University of New Mexico
UNM Digital Repository

Chemistry ETDs | Electronic Theses and Dissertations

7-2-2011

Probing morphology-dependent aggregation and photocurrent generation in polymer/fullerene photovoltaic devices

Yongqian Gao

Follow this and additional works at: https://digitalrepository.unm.edu/chem_etds

Recommended Citation
Gao, Yongqian. "Probing morphology-dependent aggregation and photocurrent generation in polymer/fullerene photovoltaic devices." (2011). https://digitalrepository.unm.edu/chem_etds/14

This Dissertation is brought to you for free and open access by the Electronic Theses and Dissertations at UNM Digital Repository. It has been accepted for inclusion in Chemistry ETDs by an authorized administrator of UNM Digital Repository. For more information, please contact disc@unm.edu.

Yongqian Gao
Candidate

Department of Chemistry and Chemical Biology
Department

This dissertation is approved, and it is acceptable in quality and form for publication:

Approved by the Dissertation Committee:

, Chairperson

Probing Morphology-Dependent Aggregation and Photocurrent Generation in Polymer/Fullerene Photovoltaic Devices

BY

Yongqian Gao

M.S., Inorganic Chemistry

University of Science &Technology of China, P .R. China, 2006

B.E., Inorganic Materials

Anhui University of Technology, P. R. China, 2003

DISSERTATION

Submitted in Partial Fulfillment of the

Requirements of the Degree of

Doctor of Philosophy

Chemistry

The University of New Mexico

Albuquerque, New Mexico

May, 2011

Copyright©2011, Yongqian Gao

DEDICATION

To my deeply beloved family and parents to stand by with me and help me to get through the hard time, especially to my sweet baby girl, Runying. I love you all, without the support and encouragement, I would have been lost and had no chance to present this work.

ACKNOWLEDGMENTS

Here I want to thank my advisor, Professor Grey, who is knowledgeable, enthusiastic and helpful. It is my great honor to work with him as his first graduate student. He has given me passion for science and guided me to understand this project from start to finish. Without his continuous encouragement for improving my dissertation, I can hardly finish it. The professional training and the style I learned from him will benefit me in my future career.

I also thank my committee members, Dr. Hua Guo, Dr. David Dunlap, and Dr. Yang Qin, for their valuable suggestions and assistance for this project during my time in graduate study. To all the instructors who taught the courses I took, I want to say thank you and the knowledge does help and expand my view of the project. All the help is greatly acknowledged.

To all my lab mates and people who helped us build the lab, I cannot thank you enough. Adam Wise worked along with me in the early days to build the lab and collect the first set of data. Thomas Martin, an undergraduate from University of Washington, worked in our lab for three summers and contributed both to instrument development and experiments. Alan Thomas, who worked in our lab for one semester to help build the external quantum efficiency test station. Karen DeZetter refurbished our thermal evaporator to perform metal depositions onsite that saved time and avoided contamination of devices. Edwards Niles helped with experiments while I was away for

the birth of my child. The personnel in the physics and chemistry machine shops, John Demoss, Fred Fuchs and Mike Davenport, who helped us make customized parts for our instrumentation. John Weeks from Wavemetrics who gave me useful suggestions on Igor Pro programming. Douglas Wozniak (CHTM) who trained me on AFM and thermal deposition techniques at CHTM. Jian Gao, Eric Martin, Stephen Myers, undergraduate students worked in our lab including Anh Phuong Ta, Jeffrey Michael Spence, thank you all and your help is greatly appreciated.

To all my friends, thank you for the many years of support and hang out together in holidays to recharge myself. The laughter we had will live in my memory for long, the nice leisure time we spent do me good. Thank you all. Last but not least, to my family, your love is the greatest gift of all, my wife, Yuling Zheng. Yuling came to US to stay with me and quit her job in China. Her arrival eased my upset and worries. For such a sacrifice, I know I cannot say thank you enough. My sweet baby girl Runying, who was born in 2009 and her smile removed all my tiredness from the whole day work in the lab. My parents who are in China, always encourage me when we talked by phone. Thanks to my siblings, my brother Leiyong and sister-in-law Lien Liu, my twin sisters Yongxin and Yongmin who eased my mind by taking care of my parents so that I can focus on my research.

Probing Morphology-Dependent Aggregation and Photocurrent Generation in Polymer/Fullerene Photovoltaic Devices

BY

Yongqian Gao

M.S., Inorganic Chemistry

University of Science &Technology of China, P .R. China, 2006

B.E., Inorganic Materials

Anhui University of Technology, P. R. China, 2003

Ph.D., Chemistry

University of New Mexico, 2011

ABSTRACT

In this dissertation, new spectroscopic and electrical imaging approaches were developed to map morphology-dependent aggregation properties of polymer chains in model solar cell devices. These techniques reveal new correlations between local structure and material performance on sub-micron size scales which are not accessible by other techniques.

Resonance Raman spectroscopic imaging was developed as a physical probe to identify and spatially map morphology-dependent variations of intra- and interchain interactions and order in poly-3-hexylthiophene (P3HT) and [6,6]-phenyl-C61-butyric acid methyl ester (PCBM) photovoltaic blend thin films. The C=C band of P3HT backbone was decomposed into aggregated and unaggregated component contribution at ~1450 cm^{-1} ($I_{C=C}^{agg.}$) and ~1470 cm^{-1} ($I_{C=C}^{un.}$), respectively. The ratio, R, ($I_{C=C}^{agg.} / I_{C=C}^{un.}$) is used to report on the relative densities of states (DOS) of aggregated and unaggregated species. From both R and frequency dispersion resonance Raman images of these individual species, four distinct types of P3HT chains are identified and mapped in annealed P3HT/PCBM blend thin films: i) highly aggregated/crystalline; ii) partially aggregated; iii) interfacial; and iv) unaggregated/PCBM-rich.

Secondly, the effect of aggregated and unaggregated species of P3HT on photocurrent is explored by a combined resonance Raman-photocurrent imaging (RRPI) approach. Maps of *R* values and photocurrents are generated for both as-cast and

annealed P3HT/PCBM devices that permit direct spatial correlations between the P3HT aggregation state and local photocurrent generation efficiency. Regions of increased P3HT aggregation are observed at both P3HT/PCBM interfaces and in P3HT-rich areas that result in decreased photocurrent generation. Voltage-dependent RRPI studies are also performed at several applied bias levels that reveal distinct changes in photocurrents due to morphology-dependent charge mobility characteristics.

Thirdly, the effect of composition of P3HT: PCBM on aggregation and of P3HT and corresponding solar cells is studied. P3HT: PCBM thin film solar cells of variable weight/weight (w/w) compositions (i.e., 1:1 to 1:4) were fabricated to systematically perturb polymer packing (aggregation) properties. On average, increasing the PCBM weight fraction, Raman spectra in the dominant P3HT C=C stretching mode region (~1450—1470 cm^{-1}) whereas symmetric stretching C-C modes show decreased intensities and red shifts. Raman bands of P3HT C=C modes can likewise be decomposed into contributions from both aggregated and unaggregated chains and, *R* values decrease with increased PCBM content. Most aggregated (ordered) P3HT chains reside primarily outside PCBM-rich regions but, reverses for >1:1 PCBM w/w loadings where all aggregated P3HT chains reside within PCBM-rich regions. This effect is attributed to a change in the type of P3HT aggregation from inter- to primarily intra-chain. The results reveal that the polymer aggregation state and its spatial location in the film that together have a large impact on charge transport properties and material performance.

Lastly, intensity modulated photocurrent spectroscopy (IMPS) and imaging is used to study the aggregation effect on charge transport and recombination processes in P3HT/PCBM devices. This frequency-domain technique provides access to both bulk and interfacial charge transport and correlations between frequency-dependent photocurrent and local structure are revealed. Maps of the photocurrent and phase shift were recorded at several modulation frequencies spanning ~100 Hz up to 10 KHz. It was found that recombination processes involving trapped charge dominates the IMPS profiles. Temperature- and color-dependent IMPS are now being performed to better understand charge transport mechanisms.

TABLE OF CONTENTS

LIST OF FIGURES xvi

LIST OF TABLES xxv

LIST OF ABBREVIATIONS xxvi

CHAPTER 1 Introduction and motivation 1

1.1 Overview of polymer solar cells 2

1.1.1 Polymer solar cell materials.....2

1.1.2 The origin of morphology-dependent properties in polymer solar cells.....5

1.1.3 Polymer solar cell fabrication and characterization.....9

1.2 Morphology-dependent performance of P3HT: PCBM solar cells 14

1.2.1 Morphology of aggregation studies on P3HT and P3HT: PCBM films.....15

1.2.2 Physical methods to probe material morphology and structure-function correlations.....17

1.3 Spectroscopic and theoretical studies on the aggregation properties of P3HT.....17

1.3.1 Weakly aggregated H-aggregated model.....18

1.3.2 Raman imaging to probe morphology-dependent aggregation of P3HT in P3HT: PCBM blend films 22

CHAPTER 2 Instrumentation 26

2.1 Raman –photocurrent imaging system.....26

2.1.1 Review of Raman spectroscopy.....26

2.1.2 Raman-photocurrent experiment 29

2.2 Intensity modulated photocurrent spectroscopy (IMPS) and imaging 32

2.2.1 IMPS and phase lagging introduction.....32

2.2.2 Instrument set-up for IMPS 33

2.3 EQE measurement 35

CHAPTER 3 Resonance Chemical Imaging of Polythiophene/Fullerence Photovoltaic Thin Films: Mapping Morphology-Dependent Aggregated and Unaggregated C=C Species 36

3.1 Introduction.....36

3.2 Experimental section.....41

3.3 Data discussion and analysis....42

3.3.1 Absorption spectra and weakly coupled H aggregate model....42

3.3.2 Resonance Raman spectra and imaging....48

3.4 Conclusions....70

CHAPTER 4 Resonance Raman Spectroscopic- and Photocurrent Imaging of Polythiophene/Fullerene Solar Cells....73

4.1 Introduction....73

4.2 Experimental section....75

4.3 Data results and discussion....77

4.3.1 Ensemble characterization using spectroscopic approaches and I-V curves 77

4.3.2 Raman and photocurrent imaging analysis....80

4.4 Conclusion....87

CHAPTER 5 Understanding Morphology-dependent Polymer Aggregation Properties and Photocurrent Generation in Polythiophene/Fullerene Solar Cells of Variable Compositions....89

5.1 Introduction....89

5.2. Experimental section....93

5.3 Data results and discussion....96

5.3.1 Absorption and Raman spectra analysis....97

5.3.2 Uncovering Spectroscopic Contributions of Aggregated P3HT chains....100

5.3.3 Mapping the Spatial Distributions of Aggregated P3HT chains....106

5.3.4 P3HT aggregation mode changes with increased PCBM content....114

5.4 Conclusions....120

CHAPTER 6 Intensity Modulated Photocurrent Imaging of Polythiophene/Fullerene Solar Cells....122

6.1 Introduction....122

6.2 Experimental section....126

6.3 Result and discussion....127

6.4 Conclusion....136

CHAPTER 7 Future work....137

7.1 Future work....137

7.1.1 Fluorescence mapping of P3HT:PCBM films to determine free exciton bandwidths 137

7.1.2 High pressure experiment on P3HT to simulate the evolution of aggregation species in P3HT: PCBM films 138

APPENDICES 141

Appendix A: Labview program for Raman photocurrent and phase shift measurement 141

Appendix B: Labview for Intensity modulation photocurrent spectroscopy (IMPS) and imaging 145

Appendix C: Labview for Galvo scanning microscope system 148

Appendix D: Igor script for Raman spectrum fitting and imaging 151

Appendix E: Igor script for weakly H aggregated absorption spectrum fit function and instructions 161

Appendix F: Labview script for EQE measurement 164

References 166

LIST OF FIGURES

Figure 1.1. Chemical structures of P3HT and PCBM and the corresponding highest occupied molecular orbitals (HOMO) and lowest unoccupied molecular orbitals (LUMO) energy levels.. 4

Figure 1.2. The photo-induced processes at the D/A interfaces of polymer solar cells: Excitons generated by photon absorption migrate and dissociate into free charges and charge transport (CT) occurs through the homo-materials to electrodes. HOMO is the highest occupied molecular orbital and LUMO is the lowest unoccupied molecular orbital, CT is charge transport, eT is electron transfer, h^+ and e^- represent holes and electrons.... 7

Figure 1.3. Absorption spectra of as cast and annealed P3HT: PCBM films and AM 1.5 solar illumination.. 8

Figure 1.4. Schematic drawing of a bulk heterojunction (BHJ) P3HT: PCBM solar cell (left) and the corresponding atomic force microscopy (AFM) image (right) reveals complicated phase separation. Active layer P3HT: PCBM blend film is sandwiched between a transparent anode, indium tin oxide (ITO) and cathode, Al layer. Note the layer thicknesses are not scaled... 11

Figure 1.5. I-V curves of P3HT: PCBM as cast (red) and annealed (blue) solar cells in dark (dotted line) and AM.1.5 illumination (solid line). V_{max} is the maximum output

voltage, and V_{oc} is the open circuit voltage, I_{sc} is the short circuit current. P_{max}, illustrated as the shaded area is the maximum output power the cell can generate. ..12

Figure 1.6. Schematic structure of P3HT π–π stacking: The distance between stacks is 1.61 nm, and the distance inside the co-facial packing is 3.8 Å.. 16

Figure 1.7. The schematic structures of H and J aggregate. The splitting of the ground state S_0 is negligible, the excited state S_1 for aggregate is split into two energy levels, E_1 and E_2, the transition is not allowed from S_0 to E_1 (E_2) in H (J) aggregates. The energy difference between E_1 and E_2 depends on the orientation of the transition dipole moment of the molecules... 19

Figure 2.1. Raman scattering and fluorescence emission.. 27

Figure 2.2. The experimental set-up of Raman/photocurrent imaging: light from a Ar-Kr laser is directed in to microscope objective with defined polarization. The signal is collected by the detector after filtering out the Rayleigh light. Photocurrent is recorded using one lock-in amplifier which is synchronized to Raman spectrum collection. 30

Figure 2.3. Intensity modulated photocurrent spectroscopy (IMPS) set up on the confocal microscope system. An intensity modulated laser source controlled though a function generator is used to excite a BHJ polymer based solar cell. The photocurrent and phase shift are recorded by a lock-in amplifier with sweeping modulation frequency,ω. With the x-y scanning stage, the photocurrent can be mapped at a selected modulation frequency... 34

Figure 3.1. Absorption spectra of as-cast (a, red) and annealed (b, blue) P3HT/PCBM blend thin films (circles). 44

Figure 3.2. P3HT/PCBM thin film (red solid/circle trace) and dilute solution absorption spectra (blue trace). Fitted and difference spectra from Figure 3.1a are also shown for comparison. 46

Figure 3.3. Time-dependent Raman total integrated intensities of the C=C symmetric stretching mode for aluminum sealed and unsealed P3HT/PCBM thin films excited under the same excitation conditions... 48

Figure 3.4. Raman spectra of pure P3HT and PCBM excited under the same conditions. The PCBM spectrum is multiplied by a factor of 5. 50

Figure 3.5. Effect of Lorentzian component linewidth. Optimal values were determined to be 15±1 cm^{-1}. 52

Figure 3.6. Normalized resonance Raman images of the total integrated intensity and ratio images of Lorentzian components (R) of the C=C symmetric stretching mode of as-cast (a,b) and annealed (d,e) P3HT/PCBM thin films, respectively. Surface contour plots of R images for as-cast and annealed films are shown in panels' c and f, respectively... 55

Figure 3.7. a) Typical Raman spectra of as-cast and annealed P3HT/PCBM thin films excited with 647 nm light in the P3HT C=C stretching mode region. b), c) Normalized Raman intensity images measured at the same region as Figures 3.6a and 3.6d for as-cast and annealed films, respectively... 58

Figure 3.8. a), b) and center frequency dispersion images for P3HT/PCBM as-cast films and c) histograms of frequency components. d), e) and center frequency images for P3HT/PCBM annealed films and f) histograms of frequency components. Symbols are superimposed which correspond to the same regions as shown in Figures 3.6c and 3.6d... 61

Figure 3.9. Normalized intensity and R images of "over-annealed" P3HT/PCBM blend thin films (a, b) and undoped annealed P3HT thin films (c,d). 63

Figure 3.10. Thin film absorption spectra of a) over-annealed P3HT/PCBM blends and b) undoped P3HT. Franck-Condon fits are depicted as dashed lines and subtracted from experimental spectra to obtain the unaggregated band. Ratios of aggregated/unaggregated species were 1.6 and 1.4, respectively.. 64

Figure 3.11. a) Raman spectra of as-cast and annealed P3HT/PCBM thin films showing both the P3HT C=C and C-C symmetric stretching modes. Ratios of intensities of C=C/C-C modes for as-cast (b) and annealed (c) films for the same regions shown in Figs. 3.6-8. 65

Figure 3.12. Raman spectra of alkyl-substituted oligothiophene (top trace) and P3HT (top trace) annealed thin films excited at 488 nm... 67

Figure 3.13. a) Cartoon diagram of proposed P3HT (purple lines) and PCBM (gray circles) organization within blend thin films for as-cast and annealed systems.. 68

Figure 4.1. a) Raman spectra of as-cast (top panel, red trace) and annealed (bottom panel, blue trace) P3HT/PCBM blend thin film devices with contributions from

aggregated ($I_{C=C}^{agg.}$, ~1450 cm-1) and unaggregated ($I_{C=C}^{un.}$, ~1470 cm-1) P3HT chains indicated by dashed gray lines. b) Normalized EQE curves from as-cast (a-c.) and annealed (ann.) P3HT/PCBM devices. The dashed cyan line depicts the excitation wavelength used for RRPI experiments (488 nm). c) Current density-voltage (J-V) curves of as-cast (a-c.) and annealed (ann.) P3HT/PCBM photovoltaic devices recorded in the dark (solid traces) and exposed to white light with an intensity of ~100 mW/cm^2 (dotted traces)... 78

Figure 4.2. ITO/PEDOT Raman contribution: a) Corrected P3HT: PCBM Raman and fit, R = 2.15; b) ITO/PEDOT/P3HT: PCBM/Al Raman and fit, R = 2.19; c) Comparison of two Raman spectra... 80

Figure 4.3. a, d) Integrated total C=C mode Raman intensities (normalized), b, e) "R" images, and c, f) photocurrent images of as-cast and annealed P3HT/PCBM devices, respectively, measured under the same conditions (Scale bars = 5 μm). g), h) and i) Linescan graphs of Raman intensity (red), R (blue) and photocurrents (green), respectively, for annealed devices indicated by arrows on d-f. Gray bars are provided as a guide for the eye.... 81

Figure 4.4. Optical image of one of typical PCBM crystal and halo ring around it... 83

Figure 4.5. Voltage dependent photocurrent images of an ITO/PEDOT/P3HT: PCBM/Al annealed device... 85

Figure 5.1. Excitation intensity dependent photocurrent response generated from a 1:1 w/w P3HT/PCBM device illuminated in a widefield mode.... 95

Figure 5.2. Survey AFM micrographs of a) 1:1, b) 1:2, c) 1:3, and d) 1:4 annealed P3HT/PCBM thin films (scale bars = 5 μm).....96

Figure 5.3. Absorption and averaged Raman spectra of 1:1, 1:2, 1:3 and 1:4 P3HT/PCBM as-cast a); b) and annealed, c); d) blend thin films. Raman spectra highlight the P3HT symmetric stretching backbone region with the C=C and C-C modes labeled. 98

Figure 5.4. Experimental absorption spectra (solid red traces with squares) and fits (dotted traces) using a weakly coupled aggregate model for 1:1 (a), 1:2 (b), 1:3 (c) and 1:4 (d) P3HT/PCBM annealed thin films. Fit spectra are subtracted and difference spectra (dash-dot traces) plotted against dilute P3HT solutions (solid blue traces with open circles).....102

Figure 5.5. Absorption spectra of regio-random P3HT solution (blue) and unaggregated components from P3HT solution (red). 103

Figure 5.6. Fitting procedure used to determine the relative amounts of unaggregated chains.... 105

Figure 5.7. Raman spectra of a) 1:1, b) 1:2, c) 1:3, and d) 1:4 w/w P3HT/PCBM thin films in the C=C symmetric stretching mode region of the P3HT component generated by averaging over 900 spectra from imaging experiments (see Fig. 5.3). C=C bands are decomposed into contributions from aggregated (ca. 1450 cm^{-1}) and unaggregated (ca. 1470 cm^{-1}) chains.....108

Figure 5.8. Current-voltage (I-V) curves for a) as-cast and b) annealed P3HT/PCBM devices of varying composition under exposure to white light (~100 mW/cm^2).... 110

Figure 5.9. Raman intensity (top row), aggregation (R) (middle row), and photocurrent (bottom row) images of annealed P3HT/PCBM solar cell devices (scale bars = 3 μm). A sketch outline of the PCBM-rich region in the 1:1 w/w film is superimposed on the "R" image.....111

Figure 5.10. P3HT C=C aggregate component and C-C Raman frequency images for variable loading P3HT/PCBM thin film devices (scale bars = 3 μm)..... 116

Figure 5.11. a) Histograms of the P3HT C=C "R" values shown in Fig. 4 for varying P3HT/PCBM content. b) Average P3HT aggregation (R) and exciton bandwidth (W) absorption spectra fit parameters as a function of P3HT/PCBM weight fraction.....118

Figure 6.1. Current-voltage (I-V) curves of annealed P3HT-PCBM devices measured in the dark and under AM1.5 illumination. 127

Figure 6.2. IMPS spectra of P3HT: PCBM solar cells. a) is photocurrent and phase shift spectra. b) is the complex plot of imaginary and real component of photocurrent..128

Figure 6.3. Raman image of the P3HT: PCBM annealed device. a) is normalized Raman intensity image of C=C band. b) is the R image . Square, circle and triangle represent incide PCBM –rich region (lower aggregation of P3HT), between crystals (higher aggregationof P3HT) and off crystal region (moderate aggregation of P3HT). The scale bar is 2 μm.. 130

Figure 6.4. IMPS images of P3HT: PCBM annealed device at different modulation frequency. Both phase shift and photocurrent images are presented. Scale bar is 2 μm.... 132

Figure 6.5. IMPS spectra generated from three distinct regions of the annealed P3HT: PCBM solar cell: P3HT-rich (triangle); PCBM- rich (square); P3HT/PCBM (circle). 134

Figure 6.6. a) IMPS of thick devices (~1 μm); b) high excitation intensity on the IMPS response of P3HT: PCBM devices..... 135

Figure 7.1. Schematic illustration of a pressure-dependent experiment and expected structure change of P3HT: PCBM blend with pressure. Pressure is proposed to induce similar aggregation as annealing..... 139

Figure A1. Part of the front panel of Raman and photocurrent/phase shift imaging program to show the input variables. 142

Figure A2. Front panel of IMPS program: Left top is the settings for Lock-in, which is shown in Appendix A, and left bottom is for function generator settings; the right is the indicator to show the spectra after it finishes.....146

Figure A3. Scheme of 2 axis galvo scanning system. The laser beam is steered by x and y axis mirror to scan one square region, the scan distance *l* is determined by the distance of d. Adapted from thorlabs.com with modification.....148

Figure A4. Front panel of Galvo microscope Labview program... 149

Figure A5. The window for input parameters of Raman imaging program 160

Figure A6. Parameters required for EQE measurement are set from the front panel of EQE measurement Labview script.....165

LIST OF TABLES

Table 5.1. Fit parameters used for calculating aggregate component spectra.....101

LIST OF ABBREVIATIONS

A	Electron acceptor
AFM	Atomic force microscopy
AM	Air mass
BHJ	Bulk heterojunction
c-AFM	Conductive atomic force microscopy
CCD	Charge coupled detector/device
CELIV	Charge extraction by linearly increasing voltage
CT	Charge transport
CS	Charge separate
D	Electron donor
DOS	Density of electronic states
ED	Electron diffraction
EQE	External quantum efficiency
ET	Energy transfer
eT	Electron transfer
FET	Field effect transistor
FF	Fill factor
GIXRD	Grazing-incidence x-ray diffraction
HOMO	Highest occupied molecular orbital
h	Planck constant

IMPS	Intensity modulated photocurrent spectroscopy
IPCE	Incident photon to current efficiency
IQE	Internal quantum efficiency
ISC	Inorganic solar cells
I_{sc}	Short circuit current
ITO	Indium tin oxide
J	Current density
k	Boltzmann constant
LUMO	Lowest unoccupied molecular orbital
ns	Nanosecond
NSOM	Near field scanning optical microscopy
PCBM	[6, 6]-phenyl-C61-butyric acid methyl ester
PEDOT: PSS	Poly (3, 4-ethylenedioxythiophene) poly (styrenesulfonate)
P_{in}	Input power of photons
P_{max}.	Maximum output power
ps	Picosecond
PSC	polymeric solar cells
rr-P3HT	Regioregular poly (3-hexylthiophene)
SCLC	Space charge limited current
SERS	Surface-enhancement Raman spectroscopy

TEM	Transmission electron microscopy
TOF	Time of flight
V_{max}	Maximum output voltage
V_{oc}	Open circuit voltage
XRD	X-ray diffraction

Chapter 1

Introduction and Motivation

Morphology-dependent packing or, aggregation, interactions of conjugated polymer chains can significantly alter the optical and electrical properties of these materials thus affecting the performance of optoelectronic devices, such as solar cells, photodiodes and field effect transistors.[1-5] For example, the rates and yields of key electronic processes (i.e., charge and energy transfer) can be modulated by several orders of magnitude by simply changing material processing conditions and, hence, aggregation.[6,7] However, current experiment cannot directly interrogate and spatially correlate aggregation properties to local device performance characteristics. These correlations are also very difficult to obtain for conjugated polymer based solar cells which must incorporate electron acceptors to separate neutral excitations generated in the polymer component. This situation gives rise to complicated morphologies that cause large fluctuations of polymer aggregation and device performance whereby conventional spectroscopy and device characterization tools simply report the average over the entire material. The overarching goal of this research is to unravel buried correlations between the polymer aggregation state and photocurrent generation efficiency in solar cells on the sub-micron size scale using new spectroscopic and electrical imaging techniques described herein.

1.1 Overview of polymer solar cells

The urgent need to find an efficient, affordable and environmentally friendly alternative energy resource can be readily appreciated by both public and private sectors. Conjugated polymer based materials are excellent candidates for this purpose because of their low cost, light weight, ease of processing and flexibility. Polymer solar cell research is currently an active and vibrant area that brings together researchers from many disciplines, such as chemistry, physics, and engineering. Herein, a brief historical overview of conjugated polymer based solar cells and existing challenges is given in addition to the fundamental role of polymer packing, aggregation and morphology on material performance. Materials processing and device structures will also be discussed as well as specific structural factors affecting performance. Lastly, recent progress in materials characterization using advanced spectroscopic and scanned probe techniques will be discussed and compared to the results presented in the body of this thesis.

1.1.1 Polymer based solar cell materials

Organic solar cells have shown tremendous promise for generating inexpensive electricity and are expected to replace traditional crystalline inorganic solar cells (i.e., silicon and III-V systems) in various settings. Unlike traditional inorganic materials, organic systems require the addition of an electron acceptor[8-10] (A, , i.e., fullerenes, quantum dots, etc.) to generate free charge carriers because of small (~3-4) dielectric constants of organic semiconductors (generally, electron donors, D, with relative high

ionization potential) that result in large binding energies of primary photoexcitations (excitons) and small charge transport distances.[11-13] However, the need to include electron acceptors gives rise to complicated morphological features due to phase-separation between donor/acceptor components.[14-18] Morphology features vary with material processing (viz. solvent and annealing) with size scales typically on the ~10 nm to >1 micron range.[14,19] Unfortunately, current understanding cannot reliably predict the optimal morphologies to maximize performance for a given polymer-based material system. The fact that many common characterization tools such as absorption spectroscopy, current-voltage curves (see section 1.1.3), do not provide access to structure-function relationships on critical sub-micron scales also complicates material design and optimization.

Since the first organic solar cell with reasonable power conversion efficiency (~1 percent, compared with 10^{-3} percent obtained previously from single component cells) was fabricated by Tang and co-workers in 1985[20] using phthalocyanine and perylene molecule bilayer structures, this field has been attracting attention not only from academia but also industry. Most notably, the discovery of light absorbing and emitting conjugated polymer semiconductors has given this field greater breadth and potential by providing increased tunability of electronic properties and processing capabilities.[21-23] This fact is highlighted by the awarding of the 2000 Nobel Prize in Chemistry to Heeger, MacDiarmid and Shirakawa for their pioneering work in conducting polymers.[24,25] These milestones have significantly expanded the playing field available for scientists to realize

the goal of inexpensive and efficient solar cells. In addition, other optoelectronic applications, such as field-effect transistors[26-30] and light emitting diodes,[31-35] have likewise benefited from this seminal work.

Figure 1.1. Chemical structures of P3HT and PCBM and the corresponding highest occupied molecular orbitals (HOMO) and lowest unoccupied molecular orbitals (LUMO) energy levels.

In the past 20 years, conjugated polymer materials have been studied extensively, such as poly-phenylene vinylene (PPV) derivatives,[36-39] polyfluorene derivatives[15,40] and polythiophene (PT) derivatives[38,41-44] for potential optoelectronic applications. The research described herein focuses on a prototype polythiophene/fullerene polymer solar cell material system that represents the current benchmark for performance. Blend thin film composites of poly-3-hexylthiophene (P3HT) and (6, 6)-phenyl-C61-butyric acid methyl ester (PCBM) comprise one of the most successful polymer-based solar cell systems to date.[45-49] The chemical structures and frontier energy levels are shown in

Figure 1.1. P3HT serves as the light absorbing and electron donor system and PCBM functions as an electron acceptor. The energy difference between highest occupied molecular orbitals (HOMO) and lowest unoccupied molecular orbitals (LUMO) of P3HT is about 1.9 eV, corresponding to ~30% solar photon absorptions. With careful tuning of morphologies, the power conversion efficiency can routinely reach above 5%.[46,48]

The following describes the basic principles of polymer solar cell operation that also highlights the impact of material morphology. It is expected that if device efficiencies reach 10% then commercial viability is possible. However, this enhancement requires fundamental understanding of the morphology effects as well as polymer packing, which governs the donor and acceptor morphology and packing interactions.[50]

1.1.2 The origin of morphology-dependent properties in polymer solar cells

Photocurrent generation in donor/acceptor polymeric solar cells is the outcome of multiple processes typically on the sub-picosecond (ps) timescale.[51,52] As will be shown below, the rates and yields of these processes are highly dependent on local morphology and polymer aggregation characteristics. Figure 1.2 illustrates the physical processes responsible for photocurrent generation in solar cells: i) Photon absorption creating Coulombically bound electron-hole pairs or, excitons, generally within the polymer component; ii) exciton diffusion, excitons migrate randomly to lowest energy sites within their lifetime (typically <1 nanosecond);[53] assuming, most excitons reach D/A interfaces; iii) charge generation, excitons split into free charges at D/A interfaces, which is an

ultrafast process (~45 fs)[54]; iv) charge transport (CT), free charges require a continuous pathway to be collected at their respective electrodes, i.e., electrons to cathode, and holes to anode. However, several undesired processes can reduce device performance to unacceptable levels. For example, two major loss mechanisms tend to dominate in polymer solar cells that are also morphology-dependent. One is trapping of charge by defects, which can originate from material defects that reduce net charge generation. Another one is recombination, either geminate or non-geminate, which occurs at polymer/fullerene or contact interfaces.

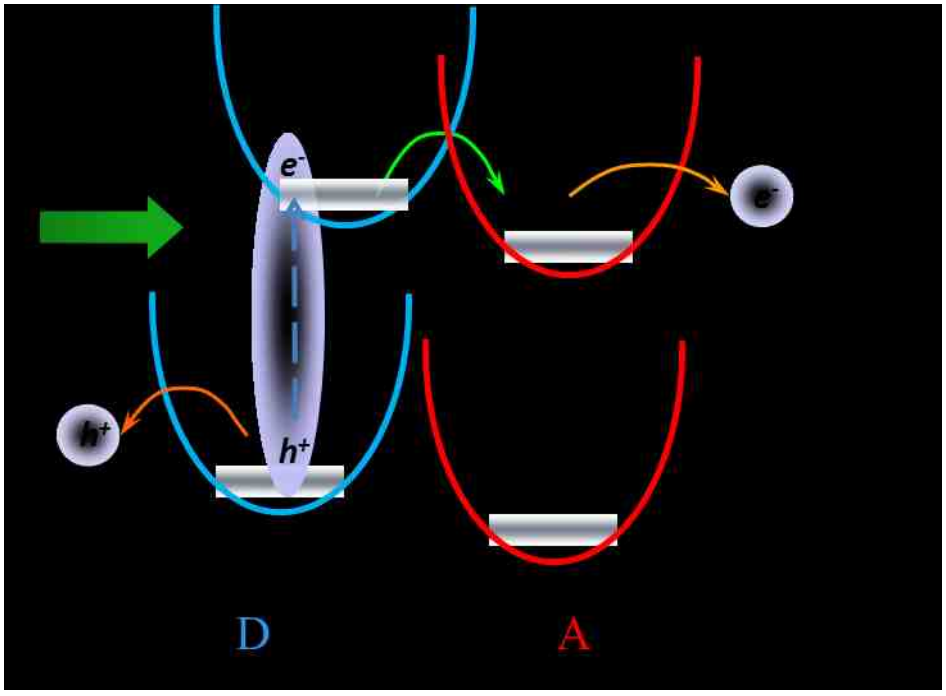

Figure 1.2. The photo-induced processes at the D/A interfaces of polymer solar cells: Excitons generated by photon absorption migrate and dissociate into free charges and charge transport (CT) occurs through the homo-materials to electrodes. HOMO is the highest occupied molecular orbital and LUMO is the lowest unoccupied molecular orbital, CT is charge transport, eT is electron transfer, h^+ and e^- represent holes and electrons.

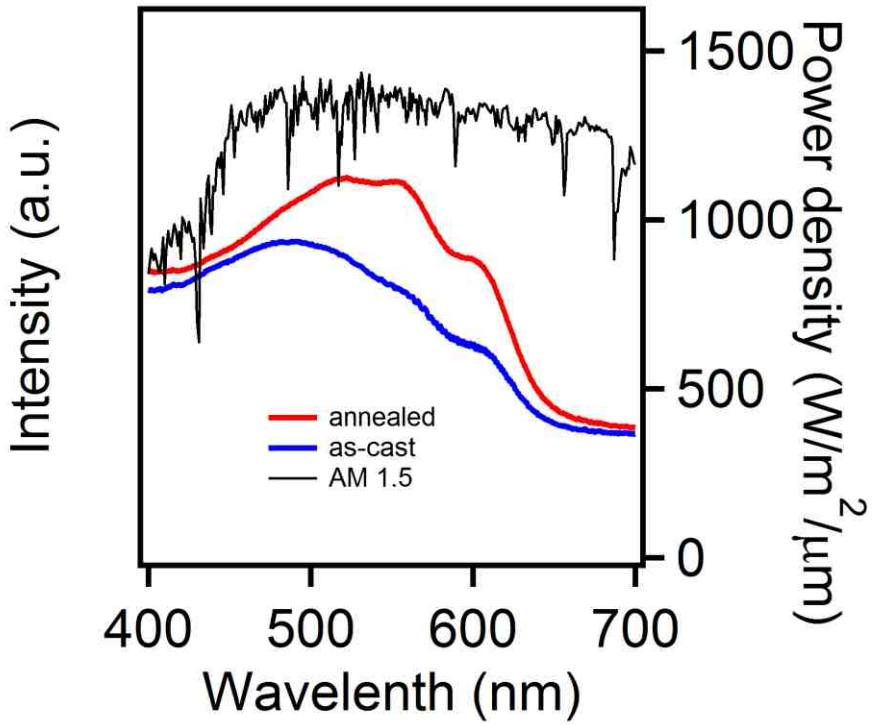

Figure 1.3. Absorption spectra of as cast and annealed P3HT: PCBM films and AM 1.5 solar illumination.

These four processes show different dependences on morphology, which changes the fabrication conditions of solar cells. These effects are discussed based on the representative P3HT: PCBM material system and the effect of processing on the P3HT packing is emphasized. Here we use annealing treatments to visualize the effect of packing and morphology on the optical and electrical properties of the polymer. As shown in Figure 1.3, absorption spectra show noticeable increase around 600 nm region of the P3HT: PCBM films is upon annealing process, which is attributed to increased

P3HT aggregation. This change of absorption lineshapes results in more exciton generation, which is beneficial to improve polymer solar cell performances. In a solar cell composite, annealing treatments not only tune the P3HT polymer chains by forming aggregated chains, but also lead to a larger phase separation of P3HT and PCBM. However, larger phase domains reduce interfacial areas, which lower exciton dissociation yields. Charge transfer requires large interfacial areas to get efficient exciton separation, assuming exciton dissociation is 100%. Charge transport, which occurs in the individual components, requires continuous pathways to minimize carrier recombination and scattering. The charge mobility is intrinsically low in polymers due to disorder. Typically this value exists in the range of 10^{-7} up to 10^{-3} $cm^2/V/s$ depending on the aggregation properties of the polymer. It is reported that two dimensional charge transport (i.e., intra and interchain) is possible in ordered P3HT regions which can improve charge mobility up to 0.1 $cm^2/V/s$.[27,55,56] Charge recombination, is likewise greatly suppressed upon annealing treatments.[57] Importantly, these findings were generated from ensemble techniques that only report the average over the entire material and any local fluctuations are lost. To probe the morphology-dependent material properties in polymer solar cells, new spatial mapping approaches are needed.

1.1.3 Polymer solar cell fabrication and characterization

Solution-based approaches are widely used to fabricate polymer solar cells with different morphologies such as roll-to-roll methods, doctor blading, etc.[52,58,59] Overall,

spin-coating is the most common deposition technique to prepare polymer solar cell devices.[60-62] In general, polymers and fullerenes are dissolved in organic solvents (i.e., toluene, chlorobenzene, etc.) and blended in specific ratios (i.e., 1:1 w/w P3HT/PCBM). In the spin-coated films, polymer chains are packed randomly to form different aggregation states. Importantly, solvents and spin-coating conditions can be varied to tune the resulting blend thin film morphology that is known to alter device performance. Annealing methods (thermal or solvent annealing) have been proven to alter the nanoscale lateral phase separation of both the P3HT aggregates and PCBM domains. Generally, the annealing temperature is below the glass transition temperature of polymer to keep film in solid state but still allows the system to reach its thermodynamic minimum by adjusting the conformation and increase the diffusion of PCBM. The final phase domain sizes are controlled by the annealing time.[60,62,63]

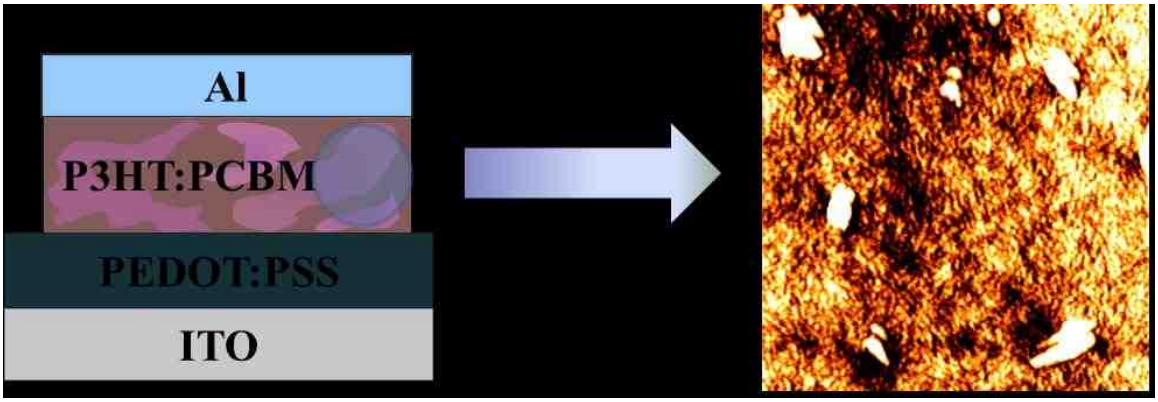

Figure 1.4. Schematic drawing of a bulk heterojunction (BHJ) P3HT: PCBM solar cell (left) and the corresponding atomic force microscopy (AFM) image (right) reveals complicated phase separation. Active layer P3HT: PCBM blend film is sandwiched between a transparent anode, indium tin oxide (ITO) and cathode, Al layer. Note the layer thicknesses are not scaled.

For polymer solar cells, the most successful architecture so far is the bulk heterojunction (BHJ) type structure, as shown in Figure 1.4. The BHJ type structure possess complicated nano- to micro-phase separated domains which enhances donor/acceptor interfaces to increase exciton harvesting, thus improving charge generation in polymer solar cells.[1,36,64] Thin films of BHJ systems are typically deposited on a transparent electrode, indium tin oxide (ITO), that functions as the anode. Generally, one conductive polymer layer poly-(3, 4-ethylenedioxythiophene) poly (styrenesulfonate) (PEDOT: PSS) is spun onto the bottom substrate as an hole transport layer before the D/A layer. The active layer (shown as a P3HT: PCBM blend film) is coated thereafter which absorbs light and generates free charges. The top electrode is thermally

evaporated onto the film to complete the device. In general, the top electrode is lower work function metals such as aluminum (Al) to work as cathode to collect electrons. P3HT: PCBM blend films, as well as other conjugated polymer solar cell materials, show complicated morphology, which need to be carefully optimized to enhance the electronic processes described above.

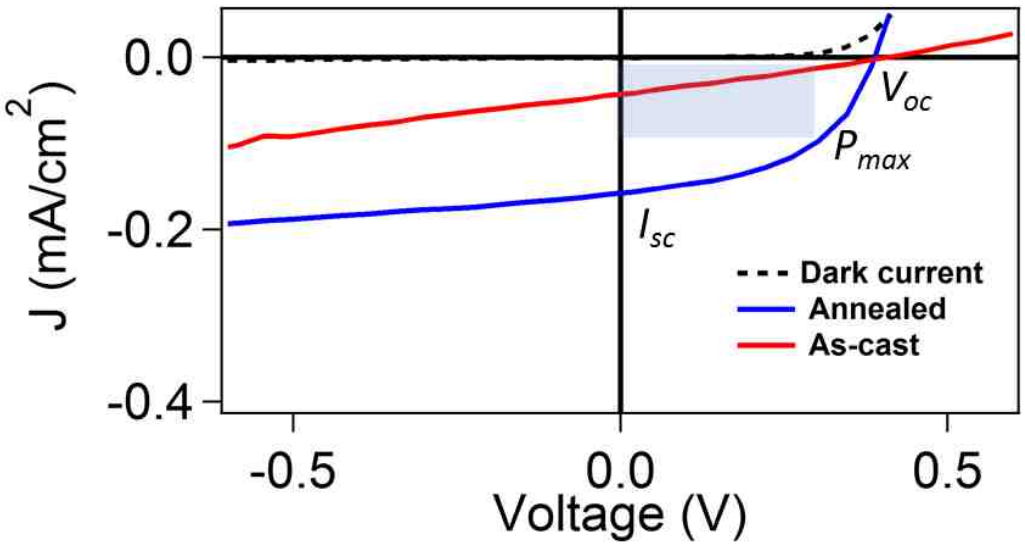

Figure 1.5. I-V curves of P3HT: PCBM as cast (red) and annealed (blue) solar cells in dark (dotted line) and AM.1.5 illumination (solid line). V_{max} is the maximum output voltage, and V_{oc} is the open circuit voltage, I_{sc} is the short circuit current. P_{max}, illustrated as the shaded area is the maximum output power the cell can generate.

As suggested in Fig. 1.5, the film morphology is critical to the device performance. To quantify the solar cell performances, the power conversion efficiency (PCE) is the most commonly reported figure of merit. In principle, the PCE is the product of all efficiencies for each process described above and is measured using current-voltage (I-V) techniques under AM1.5 illumination. Through sweeping the electric filed (applied voltages), the response current is plotted with and without illumination at AM1.5. Figure 1.5 shows two representative I-V curves for as cast and annealed BHJ P3HT: PCBM solar cells. Typical I-V curves of as cast and annealed P3HT: PCBM solar cell are shown in Figure 1.5 with (dotted line) and without illumination (solid line). To determine the efficiency, we need to measure the critical values which are: V_{oc}, the open circuit voltage, I_{sc}, the short circuit current, FF, the fill factor, and Pin, the incident light power density, which is the power of standard illumination, AM 1.5. The equations for PCE, η and FF are:

(1-1)

(1-2)

These two I-V curves of as-cast and annealed P3HT: PCBM devices give direct evidence that PCE of the annealed device is larger than as cast one (0.6% vs. 0.3%). The spectral response of a device, also known as external quantum efficiency (EQE) or, incident photon to current efficiency (IPCE), is also a useful characterization technique. Device EQE's are obtained by measuring the photocurrent, J_{sc}, change along with the

incident illumination power, P_λ, at specific wavelength, λ, and the relationship can be expressed as:

$$EQE = \frac{N_e/_s}{N_{photon}/_s} = \frac{I_{sc}/_e}{P_\lambda/\left(\frac{hc}{\lambda}\right)} \approx \frac{1240 J_{sc}}{\lambda P_\lambda} \quad (1\text{-}3)$$

The improvement on P3HT: PCBM solar cells using annealing techniques and small molecule additives to improve aggregation has been reported from a variety of research groups.[62,65] Camaioni et al. found that thermal annealing at only 55.8 ^oC increases the efficiency of P3HT: fulleropyrrolidine solar cells from 0.1% to 0.6%.[66] The remarkable PCE of 3.5% was achieved by annealing the rr-P3HT: PCBM blend[67] which results in better phase separation and charge transport. With careful tuning the morphology using thermal annealing approach, PCE values of P3HT PCBM system were reported up to 5% in 2005.[46,47]

1.2 Morphology-dependent performance of P3HT: PCBM solar cells

It is now widely accepted that the dominant contributor to high efficiency in this system is the establishment of phase separation and aggregation of polymer component that promote efficient charge transport. However, it is difficult to quantify and spatially map the intrinsic morphology-dependent variation of aggregation using conventional characterization tools. Here we give an overview of current attempts to correlate morphology and performance with scanning techniques. Scanned probe techniques are

commonly used to image morphology that is capable of achieving sub-100 nm resolution. Atomic force microscopy (AFM) is routinely used to characterize surface topography as well as phase imaging.[19,68-71] As for P3HT: PCBM blend films, the aggregation state cannot be readily identified from AFM images but, rather, only phase separation characteristics at the surface of the film.

1.2.1 Morphology of aggregation studies on P3HT and P3HT: PCBM films

Ordered P3HT chains exist in co-facial π–π stacks and are dependent on local composition. This packing distance is probed by X-ray diffraction (XRD) techniques which reveals that the d-spacing between co-facially packed chains is 3.8 Å, however, the distance between two neighboring stacks is 1.61 nm and the alkyl chain distance between two stacks is ~3.8 Å.[72] The π–π stacked P3HT structure is shown as Figure 1.6. Importantly, as PCBM is added to P3HT, the packing characteristics are affected which affects not only charge transport but also exciton diffusion and dissociation. Moreover PCBM molecules cannot intercalate into ordered P3HT chains which limits the accessible morphologies.[73]

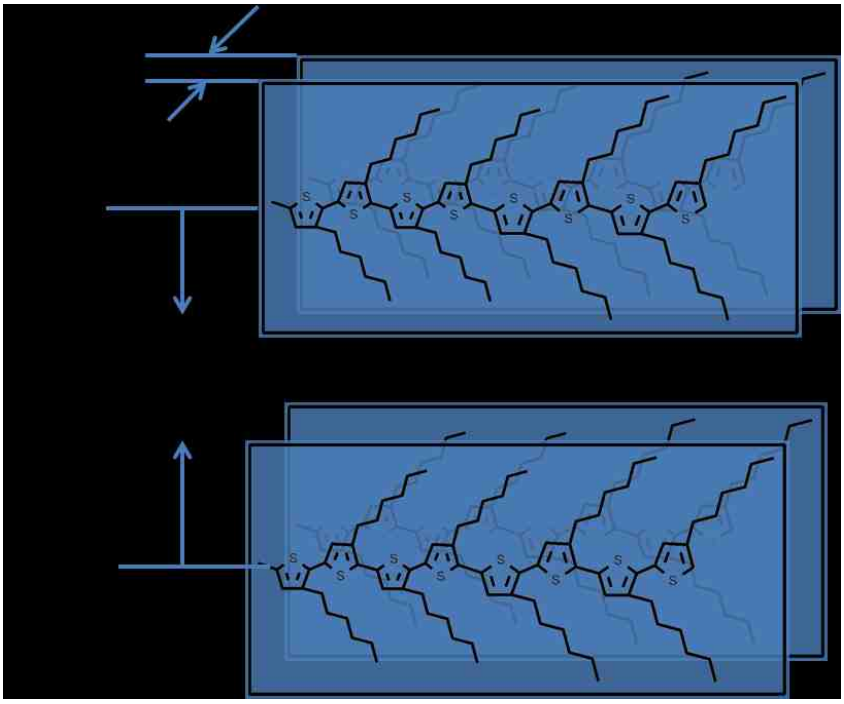

Figure 1.6. Schematic structure of P3HT π–π stacking: The distance between stacks is 1.61 nm, and the distance inside the co-facial packing is 3.8 Å

Grazing-incidence x-ray diffraction (GIXRD),[74] transmission electron microscopy (TEM) and electron diffraction (ED) studies performed by different research groups on P3HT: PCBM blend films confirmed that the aggregated regions of P3HT take on preferred orientations.[75] These findings are useful to illustrate the aggregation changes with processing conditions. However, a detailed understanding of the spatial variation of aggregation is needed in order to establish reliable correlations with device function.

1.2.2. Physical methods to probe material morphology and structure-function correlations

Various spatial mapping approaches have been explored to correlate the morphology to device performances such as electrostatic force microscopy (EFM),[76] scanning tunneling microscopy (STM).[77] One of the representative methods is conductive atomic force microscopy (c-AFM) using conductive tip to measure photocurrent and topography at the same time with controlled applied bias, which can offer up to 150 nm resolution to map the morphology-dependent photocurrent.[69,78-82] Several groups have performed this type of measurement on P3HT: PCBM devices. Local charge mobility mapping shows that the electron and hole mobilities both increase upon thermal annealing (from 10^{-5} to 10^{-3} $cm^2/V/s$), and confirms the previous bulk measurement results. Even though topography-photocurrent correlation is established in c-AFM, the ordered and disordered polymer regions and distribution cannot be identified.

To better understand polymer packing effects in polymer/fullerene composites, Raman spectroscopy has been used to probe changes in the vibrational frequencies depending on the level of doping of the polymer.[83-86] P3HT: PCBM Raman spectra show remarkable sensitivity to processing that has been exploited by multiple groups to assess the morphological properties of the material.

1.3 Spectroscopic and theoretical studies on the aggregation properties of P3HT

Morphology-dependent interchain interactions of P3HT significantly affect both optical and electrical properties of P3HT: PCBM solar cells. However, this effect is not well understood in the context of molecular electronic structure theory largely because only I-V measurements and AFM surface maps are used to characterize these materials. To quantify the effect, we focus on only the P3HT component without any packing perturbations from PCBM. Aggregates in pristine P3HT films and solutions have been revealed using optical spectroscopic approaches such as emission and absorption spectroscopy. The self-aggregation of P3HT is known to play an important role in its optoelectronic properties[87,88] and a theoretical model has been developed by Spano and co-workers to quantify electronic coupling and order in P3HT chains that can be extended to solar cell composites.

1.3.1 Weakly aggregated H-aggregated model

Recent absorption and emission spectroscopic studies on undoped P3HT thin films have demonstrated that the lowest energy optical absorption band is distorted resulting in a non-Poissonian shape.[89-91] Specifically, the intensity of the electronic origin (0-0) was found to be sensitive to material processing conditions which suggests that polymer packing is affected. To explain the lineshape deviation from a standard Frank-Condon progression, Spano and co-workers introduced the weakly coupled H aggregate model to describe the intensity and lineshape contributions as overlapping transitions from both intrachain (unaggregated) and interchain (aggregated) species.[89,92]

This model explains the aggregation effect and also can qualitatively estimate aggregation fraction depending on material processing conditions.

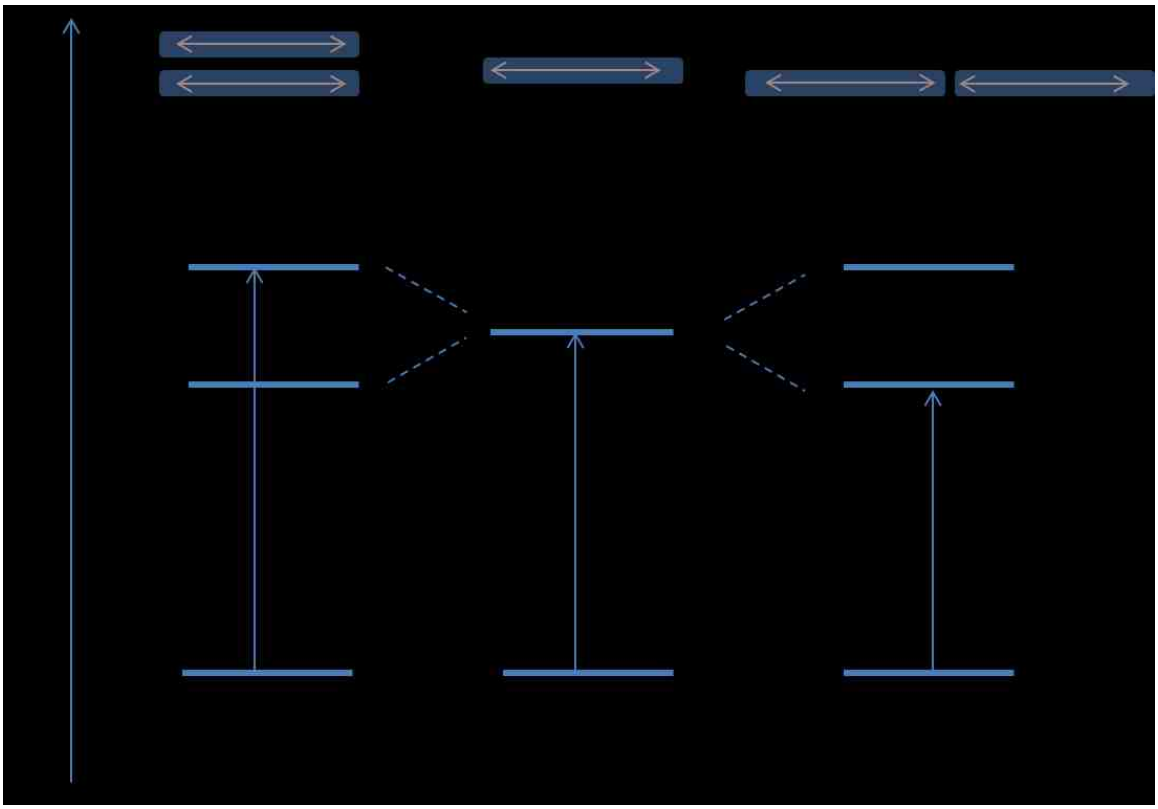

Figure 1.7. The schematic structures of H and J aggregate. The splitting of the ground state S_0 is negligible, the excited state S_1 for aggregate is split into two energy levels, E_1 and E_2, the transition is not allowed from S_0 to E_1 (E_2) in H (J) aggregates. The energy difference between E_1 and E_2 depends on the orientation of the transition dipole moment of the molecules.

In general, the molecule packing characteristics can be divided into two categories based on different electronic and spectroscopic properties: J-aggregates and H-aggregates as shown in Figure 1.7. The concept is developed based on tightly bound exciton theory.[93-95] The J-aggregate is an end-to-end arrangement in which the transition moments of individual monomers are aligned parallel to the line joining their centers. The H-aggregate is a face-to-face arrangement in which the transition moments of individual molecules are aligned parallel to each other. The optical difference of these two aggregates is: J-aggregates exhibit a narrow peak red-shifted in the absorption spectrum with respect to the unaggregated molecule absorption. However, the absorption spectrum of the H-aggregate consists of a blue-shifted band (generally is not as narrow as the J aggregates) with respect to the unaggregated molecule absorption. The transition energy difference of aggregate and monomer is dependent on the electronic coupling, *J*, which falls off exponentially with the distance between polymer chain stacks.

As in the model to describe P3HT absorption, it is proposed that the polymer chains form a weakly bounded H aggregated species. The electronic transition is modulated by the electronic coupling factor, *J*. The change on absorption can be expressed as:

[redacted]

where A is the absorption intensity of materials. S is the Huang-Rhys factor, which is a measurement of electron-phonon coupling between the electronic transition and a vibration mode, as for P3HT, the value is considered as 1.[89,92] *m* denotes the vibrational level involved in transition. W is the free exciton band width, it is related to the electronic coupling factor, W=4*J*, the variation of W is the reason for the change of the absorption/emission spectra of aggregates. G_m is a constant obtained from $G_m = \sum_{m \neq n} {S^m}/{n!}\,(n-m)$, sum of the possible transitions from n to m. E_{00} is the 0-0 transition energy, which is about ~16500 cm^{-1}, or 2 eV for C=C symmetric stretch. E_p is the vibration energy of C=C symmetric stretch (~ 1400 cm^{-1}, or 0.173 eV). Γ is the inhomogeneous line shape function, which is normally considered as a Gaussian function with constant width for all vibronic transitions. As shown by Spano and co-workers, the 0-0 and 0-1 intensity ratio of optical spectra can be used to estimate the W by the following equation:

$$\frac{A_{0-0}}{A_{0-1}} \approx \left(\frac{1 - 0.24W/E_p}{1 + 0.73W/E_p}\right)^2 \qquad (1\text{-}5)$$

where $A_{0\text{-}0}$ and $A_{0\text{-}1}$ are the relative 0-0 and 0-1 transition intensity, E_p is the intrachain vibration coupled to the electronic transition. Here E_p is the energy of C=C symmetric vibration, 0.18 eV, which is the dominant electronic transition.[85] However, the heterogeneous nature of the annealed P3HT: PCBM films requires mapping the *W* values to correlate the physical change and device performance.

The validity of this model is demonstrated with fitting different solvent cast films. By subtracting the fitted absorption spectrum of the aggregate, it is also possible to determine the relative amounts of aggregated and unaggregated chains. The difference is very similar to as the diluted solution absorption, which should exhibit no aggregation affect in it.[92,96] The calculations indicate W increases with decreases in conjugation length and interchain interactions. For example, the absorption spectra of rr-P3HT film spun from low boiling point (bp) solvent, chloroform and high bp solvent, isodurene are fitted with this model to study the processing effect on aggregation.[96] Their results suggest that longer conjugated length and more interchain interaction P3HT chain are formed from high bp solvent with small W (20 mV, cast from isodurene). The more intrachain order and shorter conjugation length formed from low bp solvent with larger W values (120 m,V cast from chloroform). The spectroscopic analysis clearly shows the aggregation contribution, however, this analysis is based on pristine P3HT films and ensemble values to represent heterogeneous distribution of aggregation. To better understand this property, this model can be extended to P3HT: PCBM blend systems where fullerenes modulate the polymer aggregation characteristics without ground state charge transfer. The morphology-dependent change in the polymer aggregation can then be mapped with sub-micron spatial resolution using scanning spectroscopic approaches.

1.3.2 Raman imaging to probe morphology-dependent aggregation of P3HT in P3HT: PCBM blend films

The model described above to indicate that the identification of aggregated and unaggregated species from absorption of pristine P3HT film is still valid in the blend film. The absorption of the blend films can be reproduced by summing up the single component absorption spectra. McGehee et al. also suggest that the PCBM molecules cannot intercalate with P3HT chains and only physically modulate the P3HT interchain packing and intrachain order.[73] This purely physical interaction between P3HT and PCBM means that the model developed from pristine P3HT film can be extended to blend films to help us identify the changes of aggregated and unaggregated species upon annealing. As seen from optical spectroscopy and I-V curves of devices, PCBM molecules complicate morphology and aggregation properties of P3HT. Herein, a microscopic approach with high chemical sensitivity to polymer aggregation is developed using resonance Raman imaging. Furthermore, this approach permits the study of polymer aggregation in situ in a functioning device and can be combined with photocurrent imaging to reveal important structure-property correlations not possible by any other scanned probe or spectroscopic technique. In the following chapters, we will introduce the Raman and photocurrent imaging technique to probe the morphology-dependent aggregation properties on P3HT: PCBM solar cells.

In chapter 3, the weakly coupled H aggregate model used to describe undoped P3HT films is extended to P3HT: PCBM blend system. It is shown that the dominant P3HT C=C band can be deconvoluted into aggregated ($I_{C=C}^{agg.}$, ~1450 cm^{-1}) and unaggregated ($I_{C=C}^{un.}$, ~1470 cm^{-1}) component. The relative amounts or, density of states

(DOS), of aggregated species change upon annealing leads to the spectral shift and lineshape change. Variations in relative concentrations ($I_{C=C}^{agg.}$ / $I_{C=C}^{un.}$ ratios, R) are used with Raman imaging approach to probe aggregation changes with annealing. With annealing treatments, phase separation of P3HT and PCBM components leads to four distinct aggregation regions which are assigned based on their *R* values. Although the aggregation is increased in P3HT–rich regions, the device performance is not necessarily increased at the same region.

In chapter 4, the relationship between heterogeneous aggregation and photocurrent generation is addressed using a combined resonant Raman photocurrent imaging (RRPI) approach. The findings suggest that with moderate aggregation (moderate R value regions) and phase separation show good photocurrent generation. The P3HT-rich region (with better aggregated states, i.e. higher R values) and PCBM-rich regions show relatively lower photocurrent, which may be due to less interfacial area to split neutral P3HT excitons.

In chapter 5, the P3HT aggregation state was explored with variable PBCM loadings. As we alter the loading of PCBM from 1:1 to 1:4 (w/w), the aggregation change from interchain interaction around the PCBM –rich region to self-aggregate inside the PCBM –rich region and corresponding photocurrent generation is reduced due to the inability to extract charge from these regions.

In chapter 6, the aggregation effect on charge transport, trap states and recombination rates are mapped using intensity modulated photocurrent spectroscopy

(IMPS) which can be combined with Raman imaging measurements. Phase lag between excitation and photocurrent is measured along with photocurrent at certain modulation frequencies that provide access to the effect of local morphology on charge transport and recombination mechanisms.

Chapter 2

Instrumentation

In this chapter, detailed descriptions of the instrumentation used in this research will be presented, which includes homebuilt microscope-based system for confocal resonance Raman and photocurrent imaging, homebuilt EQE measurement system and intensity modulated photocurrent spectroscopy instrumentation.

2.1 Raman –photocurrent imaging system

2.1.1 Review of Raman spectroscopy

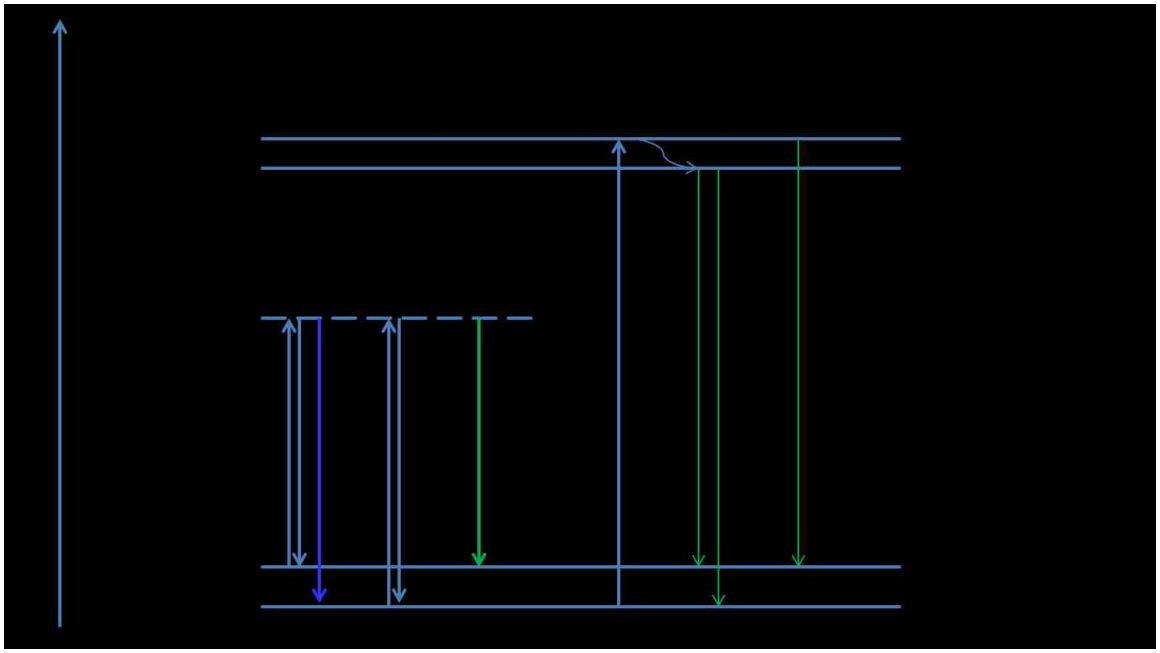

Figure 2.1. Raman scattering and fluorescence emission.

Raman spectroscopy has been used extensively quantitatively and qualitatively to study chemical bond vibrations in conjugated organic systems. The principle of Raman scattering is illustrated in Figure 2.1. When incident light excites a molecule from ground state to an intermediate virtual level or excited electronic states, it is scattered instantaneously to the ground state albeit at a different vibrational level. Most photons are scattered elastically, which is called Rayleigh scattering. A small fraction inelastic (about 1 in 10^7 photons) scattering occurs, which is called Raman scattering. It is a simultaneous two photon process: one photon is destroyed (absorbed) and another photon is created (scattered) with a certain energy shift which is equal to a vibrational quantum in the ground electronic state. When excitation energies are close to an optical transition,

fluorescence emission is a competing process that can complicate the measurement of Raman spectra.

Two types of Raman scattering are possible, namely, Stokes and anti-Stokes. In Stokes inelastic scattering, the field loses energy (exactly one vibrational quantum) with respect to the excitation frequency and anti-Stokes scattering causes the field to gain energy at the expense of the molecule. The intensities of each depend on the thermal populations of vibrational levels and usually only one type of Raman scattering (i.e., Stokes) is studied experimentally. Because the higher vibration levels are less populated at room temperature as determined by Boltzmann distribution function, Stokes shift scattering with longer wavelength (lower energy) is much more intense than anti-Stokes shift. Overall, Raman intensities depend on the intensity of the incident electromagnetic (EM) field, concentration of scatters and the cross-sections that can be expressed as:

(2-1)

where I_R is the Raman intensity, ν is the incident light frequency, $\sigma(\nu)$ is the Raman scattering cross section, $I(\nu)$ is the incident light power density, C is the concentration. Raman cross sections are typically on the order of 10^{-30} cm^2/sr, which is much smaller compared with fluorescence cross sections (~ 10^{-15} cm^2/sr). With shorter wavelength excitation, Raman scattering intensity increases with the fourth power of the incident frequency.

When a material is excited on resonance with an optical transition, large enhancements of Raman scattering cross sections are possible for modes displaced in the

excited state. This resonance effect enhances the Raman intensity by orders of magnitude (10^2-10^6) and also simplifies Raman spectra because only Raman bands of displaced modes are enhanced. Instead of the excitation promoting an electron to an intermediate virtual state, the resonance Raman technique involves promotion to an excited electronic state. However, at resonant excitation, fluorescence emission could occur too which can easily overwhelm weaker Raman bands. By exciting P3HT on resonance with its π-π^* transition (~400-600 nm), large enhancements in the total symmetric C=C breathing mode are observed. In pristine P3HT, the fluorescence is largely quenched by aggregation effects described above, however, Raman measurements can still be difficult. When PCBM is added to P3HT, efficient charge transfer quenches fluorescence to near background levels making resonance Raman spectroscopy an excellent tool for the study of these solar cell composites. This work takes advantage of PL quenching and by introducing spectral mapping to these measurements; the local variations in polymer packing and film morphology can be spatially mapped on size scales comparable to previous AFM-based measurements.

Resonance Raman spectroscopy is used in these studies to probe and identify the aggregation state of P3HT in P3HT: PCBM blend films. A home-built microscope system is developed to map this property with high spatial resolution to unravel the buried morphology-dependent aggregation changes of P3HT.

2.1.2 Raman-photocurrent imaging experiment

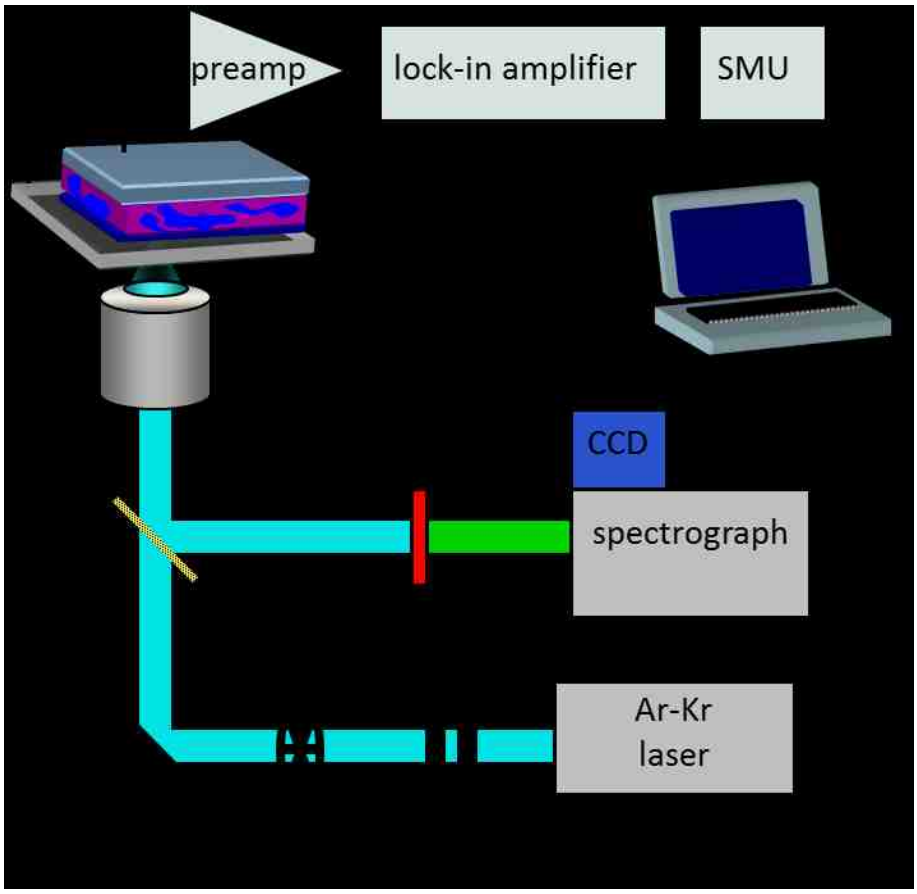

Figure 2.2. The experimental set-up of Raman/photocurrent imaging: light from a Ar-Kr laser is directed in to microscope objective with defined polarization. The signal is collected by the detector after filtering out the Rayleigh light. Photocurrent is recorded using one lock-in amplifier which is synchronized to Raman spectrum collection.

The instrumental set up for Raman-photocurrent imaging is depicted in Figure 2.2. Raman spectra and images were recorded using a home-built microscope spectrometer equipped with a nanopositioning stage (Madcity, Nano-View/M-XY) and

electron multiplying CCD camera (Andor Newton). A multi-color laser source (Ar/Kr ion, laser wavelengths range from 476 nm to 676 nm) was used to excite the sample at different wavelengths across the P3HT absorption spectrum (488 nm, 568 nm, and 647 nm). The unpolarized laser beam was directed into the microscope and reflected by a multi-color dichroic filter and focused to a diffraction limited spot by an oil immersion objective (Zeiss plan-apochromat, NA = 1.4). Raman edge filters (Semrock) were used to remove Rayleigh scattered excitation light and Raman scattered light was focused onto the entrance slits of a single stage polychromator (Andor Shamrock 303i), dispersed by a 1800 line/mm holographic grating and imaged onto the CCD. Typical spectral acquisition times were between ~200 ms to 1s and excitation intensities were ~10^5 W/cm^2 for all excitation wavelengths used. Instrument resolution was 2 cm^{-1} and experimental linewidths did not vary with the choice of slit width. Raman spectra of both as-cast and annealed films were corrected for the reabsorption of scattered light using the procedure described previously,[97] which resulted in minor changes in intensities (~4%) and no changes in lineshapes. Raman images were generated by raster scanning the nanopositioning stage over the laser spot in a synchronous fashion with CCD spectral acquisition using a LABVIEW program (See appendix A). Images were scanned for N×N points where N is the number of points per line and scan ranges varied from ~10 to 100 μm based on the sizes of P3HT/PCBM phase segregated domains determined from AFM measurements. Raman images were processed using a homemade program by plotting either the integrated intensity (area), frequency or linewidth of a particular

Raman band for each spectrum at each scan position. Spectral deconvolution of overlapping Raman bands was accomplished by performing a least squares analysis using Lorentzian functions with fixed linewidths and frequency ranges (see Appendix D and E).

Simultaneous Raman and photocurrent measurements were accomplished by modulating unpolarized laser excitation light with an optical chopper and photocurrents were measured with a combination of a pre-amplifier (current-to-voltage converter, SR570) and lock-in amplifier (Stanford, SR 830). Raman and photocurrent images were generated by raster scanning the device sample on a nano-positioning stage and recording Raman spectra and photocurrents in a point-by-point (raster) scanning fashion. A homemade script was then used to fit selected Raman bands and plot intensity, linewidth, frequency, and peak ratio images. Scan ranges varied between 10 to 40 μm that were selected on the basis of P3HT/PCBM phase segregated domain sizes determined from atomic force microscopy and optical imaging.

2.2 Intensity modulated photocurrent spectroscopy (IMPS) and imaging

2.2.1 IMPS and phase lagging introduction

Intensity modulated photocurrent spectroscopy (IMPS) has been developed to study mechanistic aspects and dynamics of charge recombination and transport processes.[98,99] This method has been widely applied in dye-sensitized solar cells[100-102] and has only recently been used to study BHJ conjugated polymer solar cells.[103,104] IMPS

measurements are performed using a small sinusoidal modulation (~10 % of DC illumination) to excite a device. The modulation frequency is swept in a wide range (typically from mHz to 100 kHz) that spans the time scales of charge recombination and transport in disordered polymeric materials. Photocurrent and phase shift are recorded using a Lock-in amplifier. In the following, the detailed experimental set-up is described based on the above microscope system.

2.2.2 Instrument set-up for IMPS

IMPS was performed using a modulated laser diode (Phoxx488, λ =488 nm) as the light source that was driven by a function generator (Fluke 271) controlled by a LABVIEW script via a GPIB interface. To ensure a linear response for the IMPS measurements, a large DC background with a small (~10%) AC component was used and average excitation powers were ~1 μW. IMPS measurements were performed on a confocal microscope spectrometer system described above. Solar cells were illuminated by a diffraction-limited laser spot (~300 nm) under short circuit conditions (0 V applied onto devices). The frequency of the AC component was swept in the 100 Hz – 10 KHz range and the photocurrent magnitude and phase shift were measured on a lock-in amplifier referenced to the modulation frequency controlled by LABVIEW software (See Appendix B). The magnitude of the frequency-dependent photocurrent, which contains both real (in-phase) and imaginary (quadrature) components, and phase shift (φ) were recorded using a lock-in amplifier (Stanford, SR 830). IMPS images were then generated

by raster scanning device samples over the diffraction-limited laser spot while holding the modulation frequency constant.

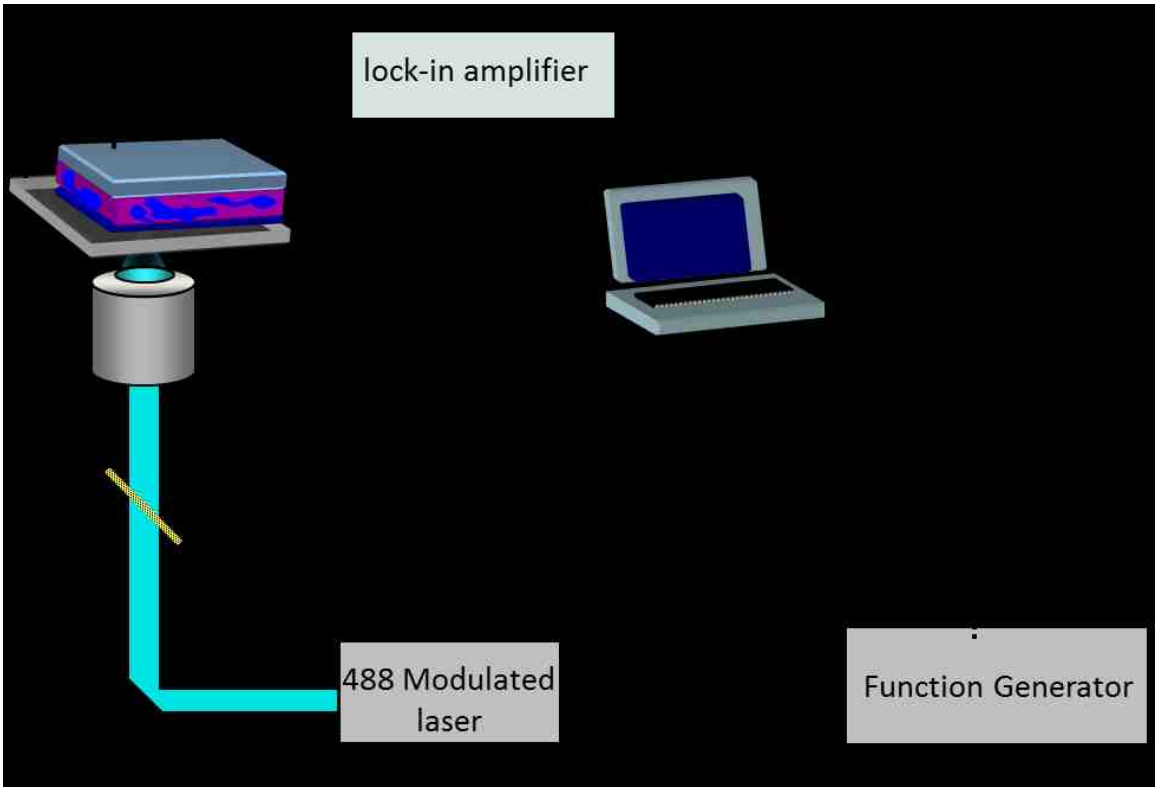

Figure 2.3 Intensity modulated photocurrent spectroscopy (IMPS) set up on the confocal microscope system. An intensity modulated laser source controlled though a function generator is used to excite a BHJ polymer based solar cell. The photocurrent and phase shift are recorded by a lock-in amplifier with sweeping modulation frequency, ω. With the x-y scanning stage, the photocurrent can be mapped at a selected modulation frequency.

Raman spectroscopic imaging was also performed over the same scan area using CW laser excitation to identify spatial variations in material composition. Raman spectra are generated by exciting the P3HT component on resonance with its π-π* transition (20490 cm^{-1}, 488 nm) and were collected using a CCD spectrograph system described above. IMPS spectra were recorded for various positions in the image field of view that were identified as P3HT-rich or P3HT-poor regions from Raman images.

2.3 EQE measurement

EQE measurement is performed using a home built apparatus. A xenon lamp (150 W) and KG 5 filter is used to simulate solar emission. The emission power is calibrated by a known response silicon photodiode at AM 1.5 condition. Photocurrent is recorded by a source meter (Keithley 2635). Light is dispersed by a monochromator. A Labview script (see appendix F) is written to control the monochromator to sweep excitation wavelengths and a Keithley 2635 collects photocurrent at each wavelength. Typically, wavelength range is set as 300-800 nm to cover the UV-Vis spectral region.

Chapter 3

Resonance Chemical Imaging of Polythiophene/Fullerence Photovoltaic Thin Films: Mapping Morphology-Dependent Aggregated and Unaggregated C=C Species

(This chapter is based on the previously published article, Journal of American Chemical Society, 2009, 131, 9654-9662. Copyright permission is obtained from *American Chemical Society*, 2009)

3.1 Introduction

Morphology-dependent variations of intra- and intermolecular interactions and order in blended photovoltaic donor/acceptor (D/A) thin films have a large impact on the type and densities of electronic states (DOS) and ultimately material performance. Among the most well-studied molecular D/A photovoltaic systems to date are solution processed blends of poly-3-hexylthiophene (P3HT) and [6, 6]-phenyl-C_{61}-butyric acid methyl ester (PCBM) that have achieved power conversion efficiencies above 5%.[45,47,48] These so-called bulk heterojunction systems take advantage of phase segregation between P3HT/PCBM (D/A) components to facilitate charge separation and transport.[105-108] The efficiencies of these processes and that of devices can be enhanced by post-processing annealing treatments that alter nano- to microscale phase domain size, shape and composition as well as the DOS of electronic species.[46,66,68,109,110] Unfortunately, reliable

control over D/A material morphologies and performance has thus far proven difficult and only incremental improvements in device efficiencies have been achieved.[49,111,112] Nevertheless, there are currently intense efforts aimed at controlling the optical and electronic properties of P3HT/PCBM blend thin films by altering film processing conditions (i.e., solvent and temperature),[46,48,113-115] inclusion of additives[65] and alternative materials deposition and patterning strategies.[116-118] Finding the optimal functional form of P3HT/PCBM systems is therefore of great practical importance which can only be realized from the aid of sensitive physical probes capable of correlating local structure to material performance.

To this end, spectroscopic or surface probe techniques are frequently combined with device current-voltage (*I-V*) or photocurrent action spectra to report on material structural changes arising from variable processing conditions on P3HT/PCBM performance in a functioning device.[49,69,78,79,110] Optical spectroscopic studies of P3HT/PCBM films have shown marked changes in both the type and DOS of electronic species depending on processing conditions and post-processing annealing treatments. For example, P3HT/PCBM blend films cast from low boiling point solvents, such as chloroform, generally yield broad and overlapping absorption transitions with little or no resolved vibronic structure.[44,113,119,120] Device *I-V* curves from these 'as-cast' films likewise show lower current densities and device efficiencies (<1%). Upon annealing, spectra recover resolved vibronic structure in the dominant C=C symmetric stretching

mode, which is commonly attributed to increased ordering (crystallinity) of the P3HT component resulting in improved device current densities and efficiencies (>5%).[110]

Interestingly, recent spectroscopic studies on undoped P3HT thin films have demonstrated that the lowest energy optical absorption band is non-Poissonian and consists of overlapping transitions from both *intrachain* (unaggregated) and *interchain* (aggregated) species.[90-92] The presence of two distinct P3HT species has also been confirmed from recent electronic structure calculations showing the existence of both crystalline (aggregated) and amorphous (unaggregated) forms with an energy difference of ~0.25 eV (2015 cm^{-1}), in good agreement with experiment.[121] In P3HT/PCBM blends, the nature of P3HT intra- and interchain interactions is more complex since the degree of phase segregation between both components affects these interactions differently than the undoped polymer. Moreover, these interactions are modulated by morphological heterogeneity thus affecting the relative DOS of both aggregated and unaggregated species that – while having a profound impact on material performance – remains poorly understood. We herein propose an extension to the physical picture developed from undoped P3HT films to describe the morphology-dependent relative DOS of aggregated and unaggregated species in P3HT/PCBM blend thin films.

Resonance Raman spectroscopy and imaging is introduced in the following that has much higher spatial resolution and chemical sensitivity than conventional optical absorption spectroscopy techniques enabling a detailed study of morphological heterogeneity on aggregated and unaggregated species. The non-invasive nature, strong

resonance enhancements of Franck-Condon displaced modes, and suppressed fluorescence backgrounds due to charge transfer quenching make Raman techniques highly amenable for studying local ground and excited state structure of photovoltaic polymeric blend systems.[120,122-127] Several groups have in fact used Raman spectroscopy to track changes in the characteristic C=C symmetric stretching backbone mode of P3HT in P3HT/PCBM blend thin films upon annealing to establish a correlation between chemical structure to device performance.[86,123,126] For example, Raman spectroscopic studies of as-cast P3HT/PCBM blend thin films reveal unusually broad C=C bands with maxima at ~1462 cm^{-1}.[127] Upon annealing, this band shifts to ~1448 cm^{-1}, narrows and becomes virtually indistinguishable from that of undoped P3HT.[127] Although the phenomenological trends in P3HT C=C Raman band frequency shifts and lineshape serve as a reliable reporter for correlating local structure to material performance, the physical origins of these effects are not entirely straightforward. Upon closer inspection, the P3HT C=C lineshape shows significant deviations from an idealized Lorentzian lineshape, i.e. overlapping transitions or shoulders, suggesting contributions from more than one species. *It is demonstrated that the C=C band of P3HT actually consists of two components centered at ~1450 cm^{-1} ($I_{C=C}^{agg.}$) and ~1470 cm^{-1} ($I_{C=C}^{un.}$) and changes in their relative concentrations upon annealing leads to apparent spectral shifts and overall lineshape changes*. These two C=C components are assigned as aggregated ($I_{C=C}^{agg.}$) and unaggregated ($I_{C=C}^{un.}$) P3HT species that show, on average, changes in relative concentrations ($I_{C=C}^{agg.}/I_{C=C}^{un.}$ ratios, R) from 0.79±0.20 to 2.45±0.77 between as-cast and

annealed P3HT/PCBM films, respectively. For longer annealing times of blend films, *R* values observed in undoped P3HT thin films are recovered (~5.5), suggesting complete phase segregation of both P3HT/PCBM components. Based on similar trends in ensemble absorption spectra of as-cast and annealed blend films, it is proposed that the *R* values measured from resonance Raman spectroscopy can be used as a reporter of the relative DOS of aggregated and unaggregated species in the P3HT component in blend films. Resonance Raman spectroscopic imaging is then used to spatially map morphology-dependent *R* values for both as-cast and annealed films to reveal the landscapes of the morphology-dependent relative DOS in P3HT/PCBM composite blend thin films. Frequency dispersion maps of $I_{C=C}^{agg.}$ and $I_{C=C}^{un.}$ species are also generated that, together with *R* images, allow us to assign sub-classifications and identify spatial distributions of these species within the blend films. The degree of aggregation measured from *R* values and images is attributed to the planarity of the P3HT chains that can be inferred from changes in the relative intensities of the C-C symmetric stretching vibration (~1380 cm^{-1}). Upon annealing, the intensities of these modes increase by about a factor of 2 and by constructing images of the ratio of C=C and C-C backbone stretching mode Raman intensities ($I_{C=C} / I_{C-C}$) we find that regions of high aggregation (high *R* values) are well correlated to regions of greater planarity (small $I_{C=C} / I_{C-C}$ values).

We conclude by briefly discussing the possible implications of P3HT aggregation on charge transfer processes in device structures and suggest future experiments to directly correlate *R* values to photocurrent generation efficiencies. Overall, the

information content afforded from this resonance Raman imaging approach provides a new insight into the impact of morphological heterogeneity on the relative DOS of aggregated and unaggregated P3HT chains in blend films that can aid materials scientists in the development of new processing strategies for improved material performance in photovoltaic devices.

3.2 Experimental section

Electronic grade, regio-regular poly-3-hexylthiophene (P3HT, Mn ~ 87,000 g/mol) and [6, 6]-phenyl-C61-butyric acid methyl ester (PCBM) were purchased from Rieke metals and Aldrich, respectively, and used without further purification. Materials were dissolved in either chlorobenzene (CB) or toluene at a concentration of 10 mg/mL for ~12 hours and filtered using a 0.2 μm filter (Whatman) to remove any undissolved solid. Glass coverslips were used as substrates that were rigorously cleaned by sonication in trichloroethylene, acetone, and methanol each for 15 min. Blend thin films were deposited by spin-casting solutions of a 1:1 w/w ratio of P3HT/PCBM at speeds of 1,000 rpm for 80 sec resulting in a ~80 nm thick film verified by atomic force microscopy (AFM). Post-processing thermal annealing treatments were used to control the morphologies of blend films by heating samples on a hot plate at 130 ^{o}C for 20 min. in a N_2 environment. Thin films were then coated with Aluminum (~70 nm) by thermal vapor deposition under high vacuum to prevent degradation from oxygen and moisture.

3.3 Data discussion and analysis

3.3.1 Absorption spectra and weakly coupled H aggregate model

Previous reports of absorption spectra from undoped P3HT thin films show non-Poissonian lineshapes that can be decomposed into contributions from interchain (aggregated) and intrachain (unaggregated) species.[90,92,128] Weakly coupled H-aggregate (interchain) species comprise the lowest energy transitions that exhibit resolved vibronic structure due to their highly ordered or, quasi-crystalline nature and increased conjugation lengths.[90,92] In contrast, unaggregated (intrachain) species show broadened and blue-shifted bands similar to dilute solution spectra suggesting substantial disorder and reduced conjugation lengths.[92] The physical basis for the assignment of the red-shifted species as H-aggregates arises from the fact that the P3HT chains adopt a more planar conformation thus leading to longer conjugation lengths and hence lower transition energies. Unaggregated P3HT molecules, on the other hand, are believed to exist in more twisted conformation and therefore conjugation lengths are reduced leading to blue-shifted band maxima.[128,129] In P3HT/PCBM blend films, intra- and interchain interactions and, therefore the relative DOS of aggregated and unaggregated P3HT species depend primarily on the degree of phase segregation between these components that, in turn, depends on the solvent characteristics and post-processing annealing treatments. In this paper, we extend the physical picture borne out of absorption spectroscopic and theoretical studies of chain packing interactions in undoped P3HT thin

films to elucidate the morphology-dependent variations of the relative DOS of aggregated and unaggregated species in P3HT/PCBM blend thin films.

We first consider electronic absorption lineshapes of P3HT/PCBM thin films in order to understand the basic nature of the relative DOS of aggregated and unaggregated species and their dependence on post-processing annealing treatments. Figures 3.1a,b present absorption spectra of P3HT/PCBM blend thin films cast from chlorobenzene (a) and thermally annealed films (b) focusing on the P3HT region (~14500—25000 cm^{-1}). Although optical absorption spectra of P3HT/PCBM blends are intrinsically more complex than those of undoped P3HT, no significant evidence for ground state charge transfer interactions exists (i.e. broad, overlapping and red-shifted bands) thus blend spectra can be described by a linear superposition of single P3HT and PCBM component spectra. Qualitative comparison of experimental spectra in Figures 3.1a, b reveals that marked changes in both lineshape and maxima occur upon annealing that are typically rationalized in terms of competing intra- and interchain interactions and ordering effects within the P3HT component.[115]

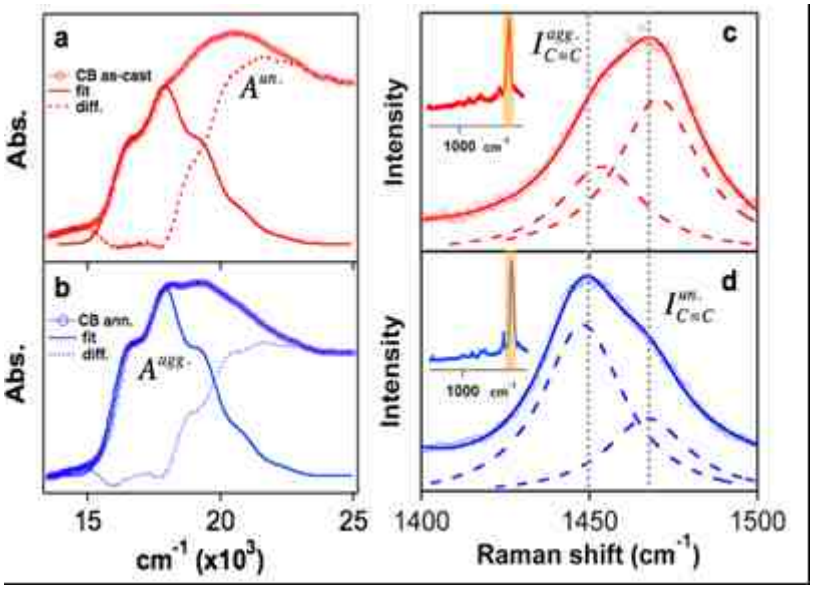

Figure 3.1. Absorption spectra of as-cast (a, red) and annealed (b, blue) P3HT/PCBM blend thin films (circles). The structured onsets of both absorption spectra are fitted using a literature model that accounts for aggregation effects on the 0-0 transition ($A^{agg.}$, solid trace).[90] Fits are then subtracted from experimental spectra revealing a broad, higher energy band corresponding to unaggregated segments of P3HT ($A^{un.}$, dashed trace). Raman spectra of as-cast (c, red) and annealed (d, blue) blend films excited with 488 nm (20492 cm^{-1}) light show the P3HT C=C symmetric stretching band represented by the shaded regions of the complete spectra shown as insets in c) and d). The C=C mode is fitted with two Lorentzian functions (dashed traces) of the form: $y1 + A_1 \{\Gamma^2/ [(x-x_1)^2 + \Gamma^2]\} + y2+A_2 \{\Gamma^2/ [(x-x_2)^2 + \Gamma^2]\}$ showing the relative contributions of both aggregated ($I^{agg.}_{C=C}$) and unaggregated ($I^{un.}_{C=C}$) components (see text for details).

A vibronic analysis of P3HT/PCBM as-cast and annealed absorption spectra is performed to unravel the contributions of both aggregated and unaggregated species to the total P3HT/PCBM absorption lineshape. In these simulations, the low energy, structured onset region (i.e. H-aggregate portion) is fitted for both as-cast and annealed spectra using a single Franck-Condon progression in the excited state P3HT C=C symmetric stretching vibrational frequency (~1400 cm^{-1}) (dashed traces, Figures 3.1a,b). Fit spectra are calculated using a model described in reference that accounts for aggregation effects, i.e. reduced intensity of the 0-0 transition which can become allowed due to disorder effects. Both as-cast and annealed absorption spectra can be fitted using the same energy of electronic origin (E_{00}) of 16500 cm^{-1} while linewidths of individual vibronic transitions are slightly broader for the former (FWHM, 810 cm^{-1} vs. 840 cm^{-1}). As seen in previous electronic absorption studies of undoped P3HT thin films, a single Franck-Condon progression is not sufficient to fit either spectrum. By subtracting the fitted spectrum, a broad and blue-shifted spectrum emerges similar to that of a dilute (<0.001 wt. %) P3HT/PCBM solution spectrum as shown in Figure 3.2. This feature has also been observed in polarized ellipsometry studies of undoped polythiophenes whereby the out-of-plane component of the optical dielectric constant shows a blue-shifted and broad lineshape.[130] Based on previous observations in undoped P3HT, the lower energy, structured spectrum is assigned as a weakly coupled H-aggregate species ($A^{agg.}$) and the higher energy; broadened spectra correspond to transitions from unaggregated P3HT chains ($A^{un.}$).

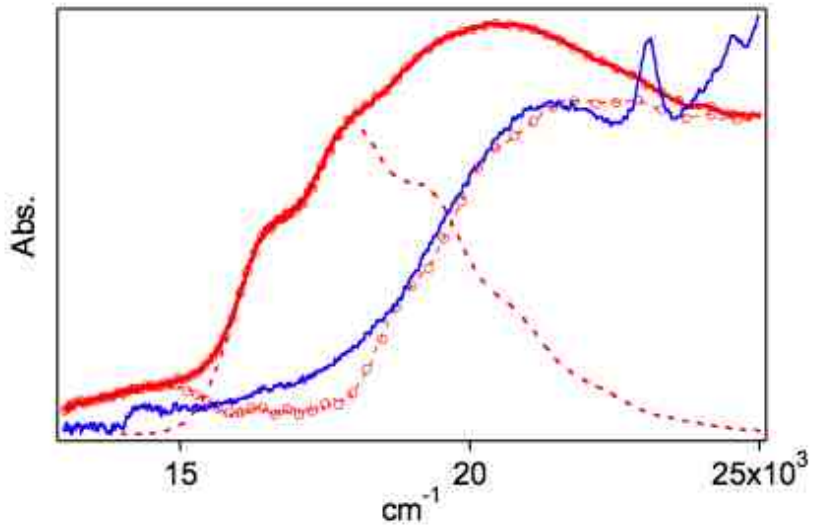

Figure 3.2. P3HT/PCBM thin film (red solid/circle trace) and dilute solution absorption spectra (blue trace). Fitted and difference spectra from Figure 3.1a are also shown for comparison.

It is interesting to note that both the energies and lineshapes of the $A^{agg.}$ spectrum change relatively little with annealing, i.e. similar C=C dimensionless normal coordinate offsets ($\Delta_{annealed}$=1.3 vs. $\Delta_{as\text{-}cast}$=1.4) which suggests that the nature of interchain interactions (π–π stacking) does not change. Estimates of excited state displacements for the $A^{un.}$ portion of the overall spectrum are obtained from the bandwidth that yield an effective Δ value of ~3. The large differences in Δ values for the aggregated and unaggregated species are likely the result of large displacements in the low frequency torsional vibrations (~200-400 cm^{-1}) in the latter in addition to contributions from the

C=C mode. These estimates provide further insight into the geometric properties of both P3HT excited species, namely, smaller Δ values and resolved lineshapes in aggregates suggest a planar conformation and longer conjugation lengths whereas the broad and unresolved lineshapes of unaggregated species indicate a twisted conformation leading to shorter conjugation lengths. Based on the small change in Δ for the A^{agg} portion of both as-cast and annealed films, lack of ground state charge transfer interactions and overall similarity to undoped P3HT absorption spectra,[92] conclude that PCBM molecules mainly modulate P3HT intra- and interchain interactions in blend films and therefore the relative DOS of aggregated and unaggregated species. Estimates of the relative DOS parameter are now determined by taking the ratios of integrated lineshapes for aggregated and unaggregated bands (i.e., $A^{agg.}/A^{un.}$) that yield values of ~0.53 and ~1.2 for as-cast and annealed films, respectively. It is important to note that these estimates are qualitative in nature due to the different Franck-Condon normal coordinate contributions and displacements for both transitions. Moreover, these values represent the average over the entire film thereby masking effects of morphological heterogeneity, which cannot be resolved by conventional absorption spectroscopic techniques. To overcome these limitations, resonance Raman spectroscopy and imaging is used to report on morphology-dependent variations in the relative DOS of aggregated/unaggregated species in as-cast and annealed P3HT/PCBM thin films.

3.3.2 Resonance Raman spectra and imaging

Since the polymer component is sensitive to light and air, before we put the imaging technique, the film's light resistance with and without protection was tested. The result is shown in Figure 3.3. The Aluminum layer protects P3HT: PCBM films from photo-induced degradation within collection time (<1 s) for each spectrum.

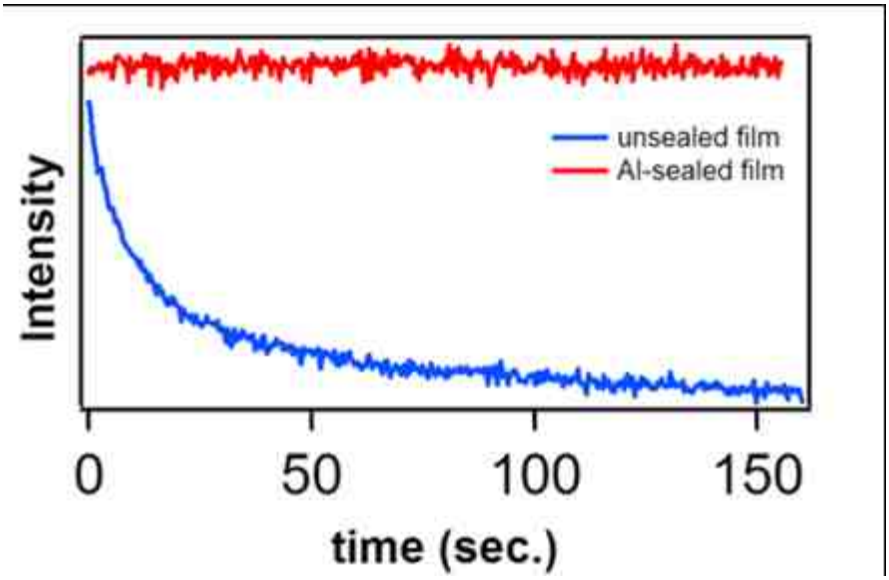

Figure 3.3. Time-dependent Raman total integrated intensities of the C=C symmetric stretching mode for aluminum sealed and unsealed P3HT/PCBM thin films excited under the same excitation conditions.

Previous reports of P3HT/PCBM Raman spectra have shown broad and overlapping C=C symmetric stretching mode lineshapes that exhibit large red-shifts (>15 cm^{-1}) and narrowing upon annealing or casting films from high boiling point solvents[123,127] These effects are generally rationalized as a single C=C band that gradually

narrows and shifts to lower frequencies due to increased intra- and interchain order and conjugation lengths.[120,123,127] We now delve further into the physical origins of these effects by first considering the characteristics of Raman lineshapes for both as-cast and annealed films. Figures 3.1c,d show Raman spectra of as-cast (c) and annealed (d) P3HT/PCBM thin films in the P3HT C=C symmetric stretching mode region excited on resonance with both the aggregated and unaggregated absorption transitions of the P3HT component at 488 nm (20492 cm^{-1}). The complete spectra are shown as insets with colored bars highlighting the C=C band that are much simpler than spectra excited off resonance[120] due to large enhancements of the P3HT C=C backbone mode scattering cross sections. Raman spectra of pure PCBM films excited under the same conditions showed negligible Raman intensities – similar to previous Raman studies of P3HT/PCBM films[86,123,127,131] and we therefore rule out any contributions from this component to the P3HT C=C lineshape (see Figure 3.4).

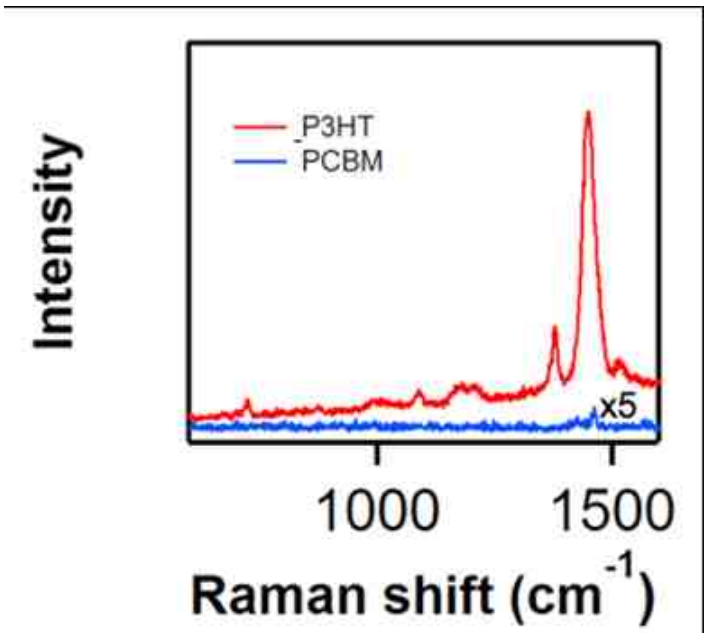

Figure 3.4 Raman spectra of pure P3HT and PCBM excited under the same conditions. The PCBM spectrum is multiplied by a factor of 5.

Upon closer inspection of the C=C Raman band for both as-cast and annealed films it is apparent that these lineshapes consist of at least two overlapping transitions. Furthermore, previous Raman spectroscopic studies of polythiophenes demonstrate that this band does not split with alkyl substitution on the 3 position of the thiophene ring,[85] thus qualitatively confirming the origin of this irregular lineshape as two different C=C species arising from different local environments. A least-squares procedure is used to fit two Lorentzian components (dashed traces, Figures 3.1c, d) to uncover the contributions of these species to the total lineshape. To ensure unique and reliable fits, linewidths were kept constant (15 cm^{-1}) and center frequencies of both species (~1450 cm^{-1} and ~1470

cm^{-1}, respectively) were constrained within 0.5% of the average center frequency (approximately ±5 cm^{-1}). The choice of linewidths for these two species was determined by varying Lorentzian fit linewidths and comparing residuals which yielded best average values of 15±1 cm^{-1}, the fitting results are shown in Figure 3.5. There was also no dependence of the fitted center frequency on the initial guess in our fit procedure when this parameter was varied within the above range the fitting parameters. On the other hand, amplitudes were allowed to vary which reflects the morphology dependent concentrations of both C=C species.

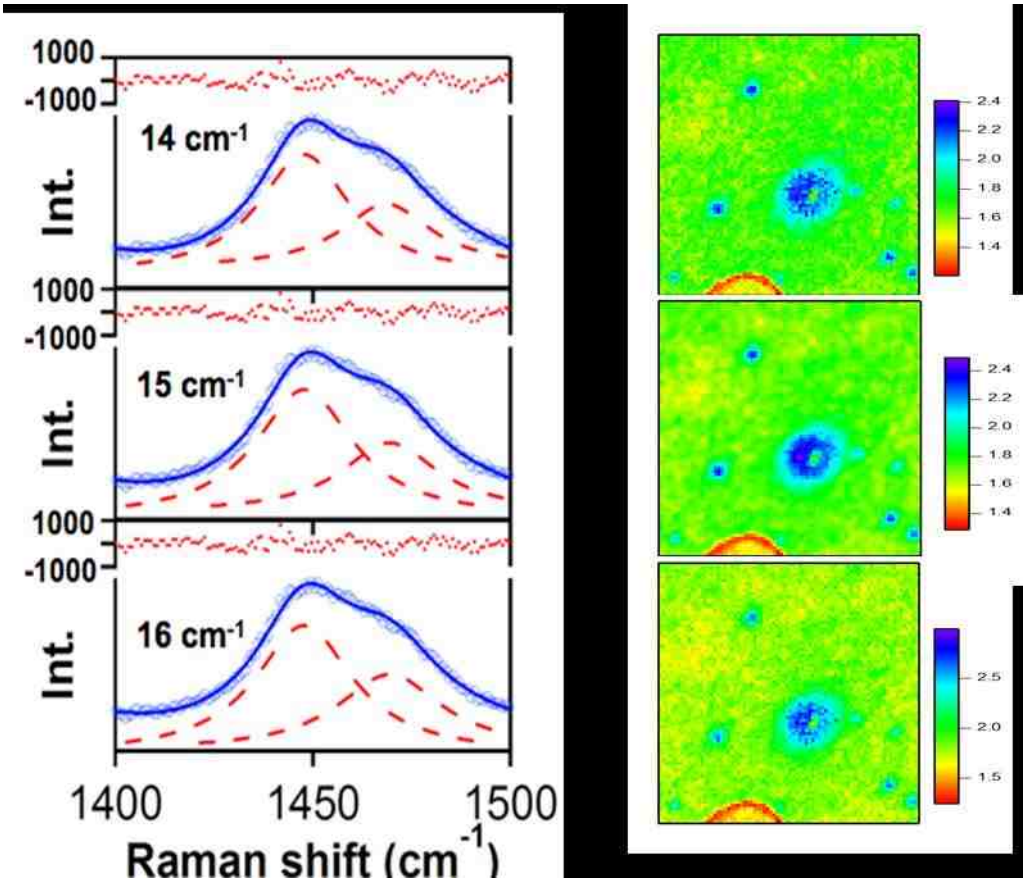

Figure 3.5 Effect of Lorentzian component linewidth. Optimal values were determined to be 15±1 cm^{-1}. R images for each linewidth are shown in the panels on the right. From this data, we find that 15 cm^{-1} yielded the highest contrast and smallest residuals therefore this value was used in the fitting procedure described in the text

Herein, spectral shifts and lineshape changes in the P3HT C=C mode upon annealing are described in terms changes in the relative concentrations of the C=C mode components due to alterations in P3HT packing interactions and order. From both experimental absorption spectroscopy and theoretical studies of undoped P3HT, the

P3HT/PCBM blend lower frequency component is assigned as aggregated P3HT C=C species ($I_{C=C}^{agg.}$) and the higher frequency component is assigned as unaggregated P3HT C=C species ($I_{C=C}^{un.}$). In this scheme, $I_{C=C}^{agg.}$ species represent P3HT chains with larger intra- and interchain order or H-aggregate-like species with longer conjugation lengths whereas $I_{C=C}^{un.}$ species correspond to chains with lower intra- and interchain order or unaggregated P3HT chains and shorter conjugation lengths. This assignment is also supported by recent theoretical and experimental studies on oligothiophenes that exhibit similar trends in Raman frequencies due to competing intra- and interchain ordering effects. [124]

Assuming that Raman scattering cross sections of both $I_{C=C}^{agg.}$ and $I_{C=C}^{un.}$ components do not change throughout the films, the ratio, R, of Raman intensities of both components is taken to obtain the relative concentrations ($N_{C=C}$) of aggregated and unaggregated species:

$$R = \frac{I_{C=C}^{agg.}}{I_{C=C}^{un.}} \approx \frac{N_{C=C}^{agg.}}{N_{C=C}^{un.}} \qquad (3\text{-}1)$$

As-cast films had average R values of ~0.8 whereas annealed films have ratios of ~2. Based on similar trends of the relative aggregated/unaggregated DOS from absorption spectra of as-cast and annealed films, it is proposed that R values measured from resonance excitation can be used as a reporter for the relative aggregated/unaggregated DOS in P3HT/PCBM photovoltaic thin films. Because no

structural relaxation effects occur in the Raman process, the R values are expected to provide a more meaningful and reliable estimate of the relative DOS compared to absorption bands. We now extend our resonance Raman spectroscopic approach to perform hyperspectral imaging and spatially map morphology-dependent R values and frequency dispersion of $I_{C=C}^{agg.}$ and $I_{C=C}^{un.}$ species for both as-cast and annealed P3HT/PCBM blend thin films.

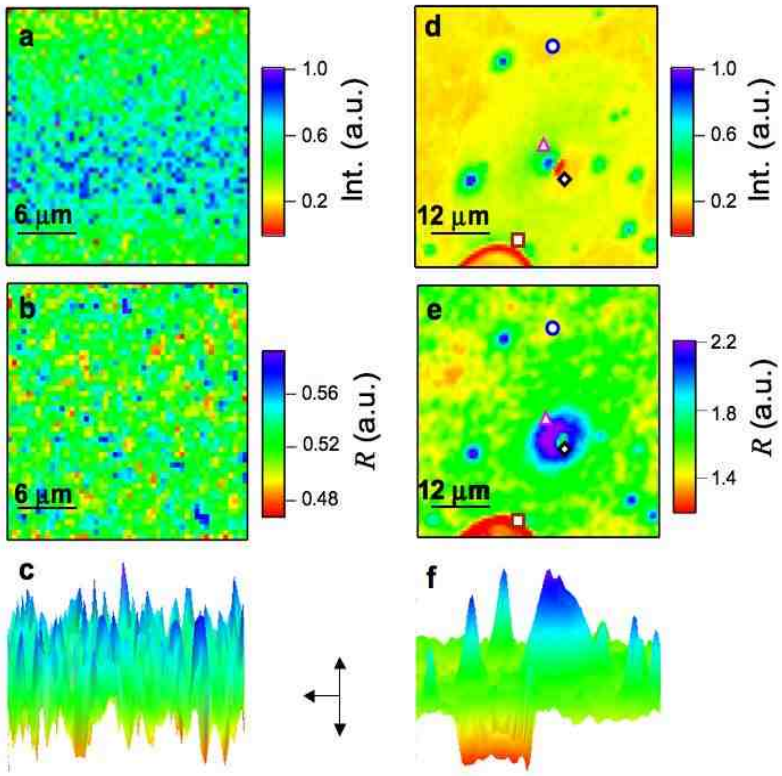

Figure 3.6. Normalized resonance Raman images of the total integrated intensity and ratio images of Lorentzian components (R) of the C=C symmetric stretching mode of as-cast (a,b) and annealed (d,e) P3HT/PCBM thin films, respectively. Surface contour plots of R images for as-cast and annealed films are shown in panels' c and f, respectively.

Resonance Raman imaging measurements performed on three different samples yielded average R values of 0.79±0.20 and 2.45±0.77 for as-cast and annealed films, respectively. Additionally, the average frequencies of $I_{C=C}^{agg.}$ species were found to be 1452±2.6 cm^{-1} and 1449±1.4 cm^{-1} for as-cast and annealed films, respectively, whereas

$I_{C=C}^{un.}$ species for both types of films had average values of 1471± 1.0 cm^{-1}. Despite sample-to-sample heterogeneity effects, as-cast and annealed films showed similar trends and these characteristics are discussed in detail in the following using representative as-cast and annealed films prepared from the same blend solution. Figures 3.6a,d presents resonance Raman images of the C=C symmetric stretching mode normalized total integrated intensities of representative as-cast and annealed P3HT/PCBM blend thin films. Because the size scale of P3HT/PCBM phase segregation determined from AFM is below the lateral resolution of our instrument, it is not possible to comment on features observed in as-cast Raman images. On the contrary, annealed films show rich structure owing to the phase-segregated nature of P3HT/PCBM components on the >1 μm size scale that is easily resolved by our apparatus. Overall, our Raman images exhibit similar features as observed in TEM,[132] electro-force microscopy [69]and off-resonance excitation Raman[86] imaging studies of P3HT/PCBM blend thin films. However, the principal advantage of our approach is the ability to spatially resolve the morphology-dependent variation of the relative DOS of $I_{C=C}^{agg.}$ and $I_{C=C}^{un.}$ species. R images of representative of as-cast and annealed blend thin films are presented in Figures 3.6b, e revealing the impact of local morphology and packing interactions on intra- and interchain order. The as-cast film had an average R value of 0.52±0.02 suggesting a greater number of $I_{C=C}^{un.}$ species and implying highly interspersed P3HT/PCBM molecules that largely suppress interchain aggregate formation. The annealed film, on the other hand, had an average R

value of 1.71±0.07 revealing a greater number of $I_{C=C}^{agg.}$ species due to increased phase segregation. Surface contour plots of both as-cast and annealed films, respectively, are shown in Figures 3.6c,f that provides greater detail into the morphology-dependent distributions of both C=C species.

In order to compare excitation wavelength effects, Raman spectra and images were also measured under off-resonance conditions using 647 nm (15455 cm^{-1}), which is expected to selectively excite $I_{C=C}^{agg.}$ species due to pre-resonance enhancement effects. Figure 3.7a shows Raman spectra of the C=C symmetric stretching mode region of as-cast and annealed P3HT/PCBM blend thin films as well as normalized intensity images measured for the same region as shown previously for 488 nm excitation, Figures 3.7b and 3.7c respectively. Since 647 nm excitation should not excite $I_{C=C}^{un.}$ species, significant deviations from the lineshapes presented in Figures 3.1c, d are expected. Indeed, both as-cast and annealed films excited off-resonance exhibit broadened Raman lineshapes and average frequencies of ~1444 cm^{-1} which represents a substantial red-shift compared to either $I_{C=C}^{agg.}$ or $I_{C=C}^{un.}$ center frequencies measured at 488 nm. It is also important to note that increased background fluorescence in off-resonance spectra leads to diminished signal-to-noise ratios especially for annealed films which have higher P3HT fluorescence yields presumably due to reduced charge transfer quenching. The lack of dependence of P3HT C=C Raman lineshapes with thin film processing conditions for off-resonance excitation conditions is most likely the result of selective enhancement

of minority $I_{C=C}^{agg.}$ species with long conjugation lengths. In this limit it is not possible to compare R values since both aggregated and unaggregated species are not excited equally, therefore off-resonance excitation is not a reliable means to interrogate morphology-dependent variations in the relative DOS of aggregated/unaggregated species.

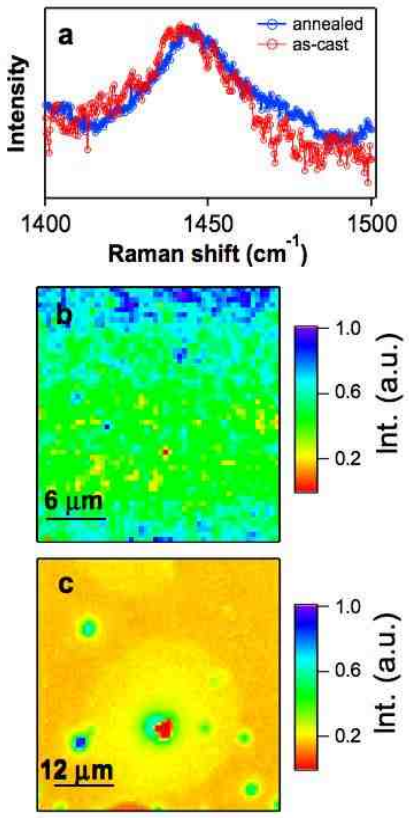

Figure 3.7. a) Typical Raman spectra of as-cast and annealed P3HT/PCBM thin films excited with 647 nm light in the P3HT C=C stretching mode region. b), c) Normalized Raman intensity images measured at the same region as Figures 3.6a and 3.6d for as-cast and annealed films, respectively.

Further comparison of normalized integrated intensity and R images for the annealed film resonance Raman image reveals four distinct regions, represented by the symbols in Figures 3.6d,e that represent distinct sub-classifications of aggregated and unaggregated P3HT species. Black diamonds highlight regions with low Raman intensities (<0.2) and R<1, blue circles represent regions of intermediate intensities (0.2< I <0.6) and 1<R<1.5, and purple triangles correspond to high intensities (>0.6) with R>1.5. Additionally, the P3HT/PCBM phase segregated domain size scales are larger than our instrument resolution (~200 nm) making it possible to interrogate the interface region between both components, which is represented by brown squares. However, due to the direct correspondence between intensity and R images, these maps are not sufficient to assign the possible structural origins of these features. We instead rely on frequency dispersion maps of $I_{C=C}^{agg.}$ and $I_{C=C}^{un.}$ species that provide greater insight into the identity and morphology-dependent distributions of these species throughout the films.

As-cast film frequency dispersion images of $I_{C=C}^{agg.}$ and $I_{C=C}^{un.}$ species are shown in Figures 3.8a, b and those of the annealed film are shown in Figures 3.8d, e. Histograms of these frequencies are also included in Figures 3.8c, f, respectively. Similar to normalized intensity and R images in Figures 3.6a,b, as-cast $I_{C=C}^{agg.}$ and $I_{C=C}^{un.}$ component frequency dispersion images show diffraction-limited features due to nanoscale phase segregation below the limit of our instrument resolution. Figure 3.8d

shows the frequency dispersion of the $I_{C=C}^{agg.}$ species for the annealed film and comparison to normalized integrated intensity and R images in Figures 3.6d, e reveals similar features (i.e. blue circles, purple triangles and brown squares). Regions represented by the blue circles likely correspond to partially aggregated P3HT chains, i.e., chains with increased interchain order (higher R values) but still possessing significant amounts of PCBM molecules. Purple triangles represent highly aggregated or quasi-crystalline P3HT chains that show lower frequencies possibly due to increased conjugation lengths and appear as red areas in Figure 3.8d. This feature resembles characteristics observed in TEM and AFM images of P3HT/PCBM blend films that show distinct crystallite or 'nanowire' formation of P3HT chains. However, because the size scale of these features are usually on the order of tens of nanometers we cannot rule out the possibility of P3HT crystallite formation in solution, a common observation in several groups. Instead it is more likely that these regions represent a statistical distribution of all possible crystallite types and orientations. We further consider the nature of aggregated species and their origins in more detail in the following.

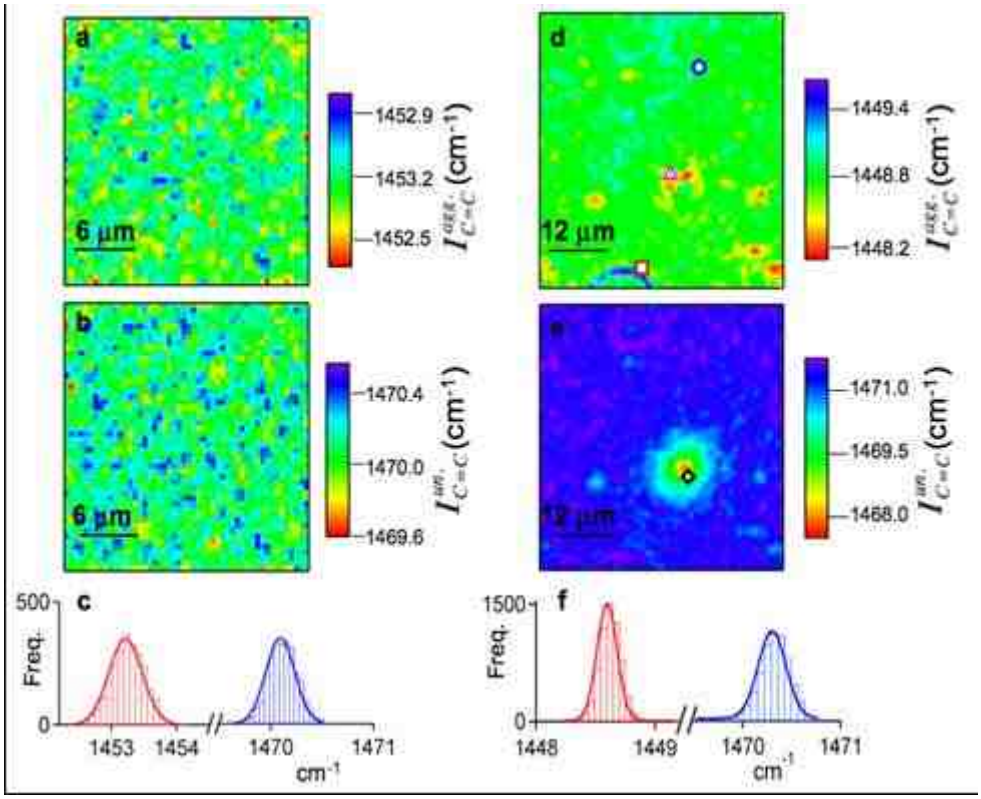

Figure 3.8. a), b) and center frequency dispersion images for P3HT/PCBM as-cast films and c) histograms of frequency components. d), e) and center frequency images for P3HT/PCBM annealed films and f) histograms of frequency components. Symbols are superimposed which correspond to the same regions as shown in Figures 3.6c and 3.6d.

Because the interfacial region between P3HT and PCBM represents an area of great importance due to photoinduced charge transfer at these boundaries, a detailed understanding of interfacial structural interactions is critical for developing improved material processing strategies for increased materials performance. The brown square in

Figure 3.8d highlights an interfacial region that possesses a broad range of R values (1-4) likely due to competing intra- and interchain ordering effects. The larger R values probably arise from the fact that the two components are almost completely phase segregated or, that the PCBM interactions at interfaces are folding P3HT chains differently in these regions. Further evidence for interfacial interactions can be observed from somewhat blue-shifted $I_{C=C}^{agg.}$ frequencies in this region, as shown in Figure 3.8d.

Figure 3.8e shows the $I_{C=C}^{un.}$ component of the annealed film that exhibits one noteworthy feature, namely a region of lower frequency (red area) represented by the black diamond. Further comparison to Figures 3.6d, e for this same region suggests this is a PCBM-rich region with interpenetrating, randomly dispersed P3HT chains. These species represent unaggregated P3HT chains since high concentrations of PCBM effectively break up interchain interactions, which is further confirmed by their low R values (<1) and intensities. Lastly, comparison of as-cast and annealed $I_{C=C}^{agg.}$ frequency dispersion histograms in Figures 4c, f shows a significant red-shift in the latter (~4 cm^{-1}). It is tempting to assign this red shift to photoinduced charge transfer effects; however, this trend contradicts previous observations that annealing decreases P3HT/PCBM interface area due to increased phase segregation that should lead to a reduction in charge transfer yields. This behavior is instead attributed to increased average conjugation lengths and intrachain order of P3HT in the annealed films. It is now interesting to

consider the effects on R and frequencies of P3HT $I_{C=C}^{agg.}$ and $I_{C=C}^{un.}$ species when both P3HT/PCBM are allowed to fully phase segregate due to over-annealing.

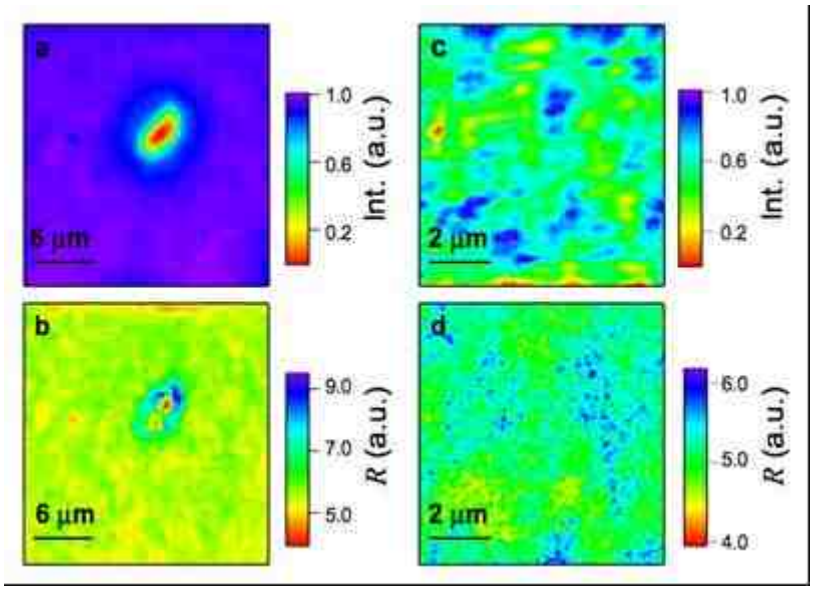

Figure 3.9. Normalized intensity and R images of "over-annealed" P3HT/PCBM blend thin films (a, b) and undoped annealed P3HT thin films (c,d).

Although large improvements of P3HT/PCBM photovoltaic device efficiencies can result from annealing leading to increased intra- and interchain order of the P3HT component,[110,112,132] over-annealing can lead to complete phase segregation of both components that diminishes material performance in a device environment. Figure 3.9 shows resonance Raman normalized intensity and R images of the C=C bands for thermally annealed P3HT/PCBM thin films cast from toluene (Figures 3.9a, b) and undoped P3HT thin films (Figures 3.9c, d). The over-annealed blend film exhibits

remarkable phase segregation with a well-resolved PCBM crystallite (I~0) providing very high contrast between P3HT and PCBM components. Comparison of R values between over-annealed blends and undoped P3HT films show approximately the same average values (~5.5) suggesting that no residual PCBM molecules exist within P3HT domains in blend films. Corresponding absorption spectra for over-annealed blend films and undoped P3HT films show noticeable increases in aggregated/unaggregated ($A_{agg.}/A_{unagg}$) ratios (1.6 and 1.4, respectively) which further confirms our conclusions from Raman spectroscopy and imaging results shown in Figure 3.10.

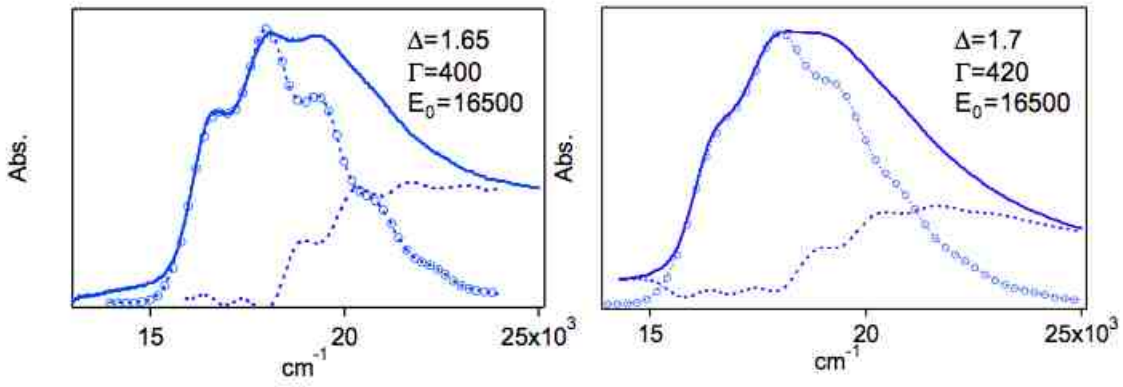

Figure 3.10. Thin film absorption spectra of a) over-annealed P3HT/PCBM blends and b) undoped P3HT. Franck-Condon fits are depicted as dashed lines and subtracted from experimental spectra to obtain the unaggregated band. Ratios of aggregated/unaggregated species were 1.6 and 1.4, respectively

On the basis of our observations from changes in Raman spectra and images upon annealing, it is apparent that significant structural rearrangements occur that lead to greater aggregation amongst P3HT molecules. We now consider the origins for the change in aggregation state of P3HT which are proposed to arise from a change in the planarity of P3HT chains.

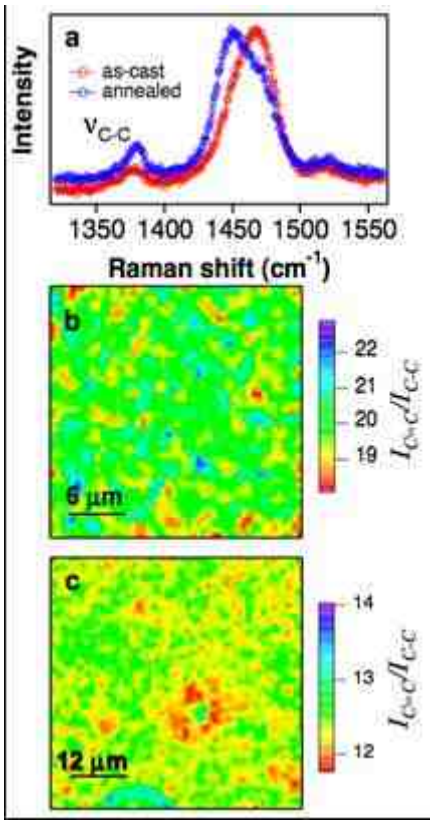

Figure 3.11. a) Raman spectra of as-cast and annealed P3HT/PCBM thin films showing both the P3HT C=C and C-C symmetric stretching modes. Ratios of intensities of C=C/C-C modes for as-cast (b) and annealed (c) films for the same regions shown in Figs. 3.6-8.

Figure 3.11a shows typical Raman spectra of as-cast and annealed P3HT/PCBM films with the C-C symmetric stretching mode appearing at ca. 1380 cm^{-1}. Upon annealing, the relative intensity of the C-C mode increases substantially (~2×) with no change in frequency. By taking the ratio of the C=C and C-C total integrated intensities ($I_{C=C} / I_{C-C}$), we find that annealed films show an average value of ~12 whereas as-cast films had an average value of ~20. It is now informative to construct spatial maps of $I_{C=C} / I_{C-C}$ values for as-cast and annealed films (Figures 3.11b, c, respectively) and compare these to R images shown in Figure 3.6. For annealed films, regions with larger R values correlate well with smaller $I_{C=C} / I_{C-C}$ ratios whereas the larger $I_{C=C} / I_{C-C}$ values of as-cast films suggest a more twisted P3HT conformation and smaller R values. The relative increase in C-C mode intensities (decrease in $I_{C=C} / I_{C-C}$ values) in annealed films is attributed to an increase of π electron density in C-C bonds resulting from an increase in planarity of P3HT chains. Previous Raman studies on oligothiophenes have suggested that the increase in C-C intensity is the result of increased charge transfer from C=C bonds,[133] however, very little experimental evidence exists to substantiate this claim. The relationship between C-C intensity and chain planarity is better observed by comparing Raman spectra from an oligothiophene derivative and P3HT annealed thin films that show larger C-C mode intensities in the latter presumably due to greater planarity (see Figure 3.12).

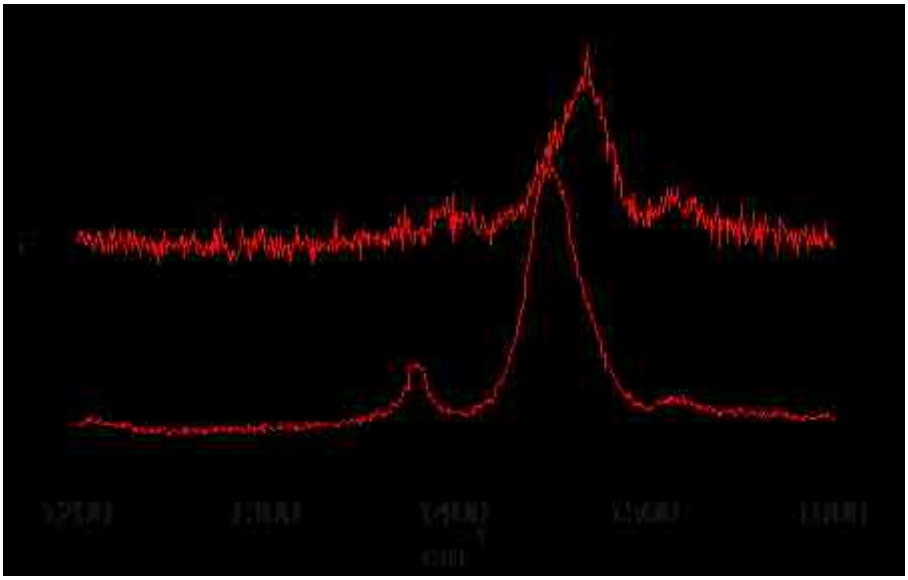

Figure 3.12. Raman spectra of alkyl-substituted oligothiophene (top trace) and P3HT (top trace) annealed thin films excited at 488 nm.

This observation is also consistent with recent experimental and theoretical studies of oligothiophenes that show planarity increases with increasing size (conjugation length).[124] Intuitively, the ability of P3HT chains to form co-facial π-π stacks should be related to the degree of planarity, therefore a direct correspondence between the degree of aggregation and planarity of P3HT chains is expected. The strong correlation between between R values and $I_{C=C} / I_{C-C}$ ratios discussed above suggests that these values do in fact provide a reliable means for tracking local changes in polymer chain planarity and, hence, aggregation. We now propose a scheme of materials organization which reconciles our data and observations with models obtained from X-ray crystallography and transmission electron microscopy.

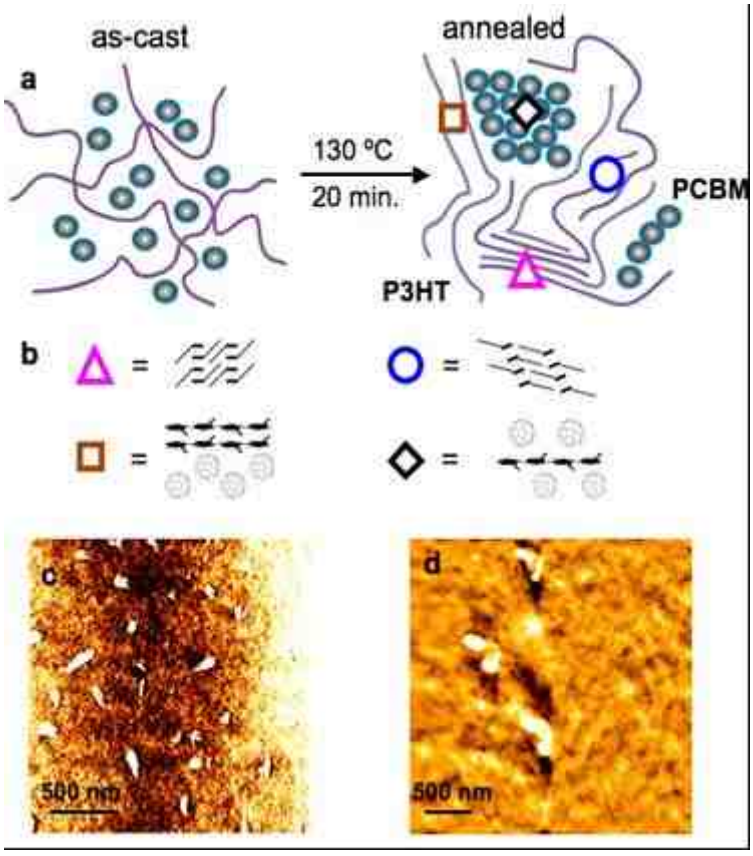

Figure 3.13. a) Cartoon diagram of proposed P3HT (purple lines) and PCBM (gray circles) organization within blend thin films for as-cast and annealed systems. Symbols represent the four previously identified regions of the blend film showing intrinsic variation of P3HT intra- and interchain interactions due to the degree of PCBM phase segregation. b) Proposed structures of regions, purple triangles: "type 1" aggregates (average spacing ~3.8 Å), blue circles: "type 2" aggregates (average spacing ~4.47 Å), brown squares: interfacial P3HT, and black diamonds: unaggregated P3HT. c), d) AFM micrographs of as-cast and annealed P3HT/PCBM thin films.

Figure 3.13a shows a schematic diagram of proposed nano- to microscale organization of P3HT (purple lines) and PCBM (gray balls) components for as-cast and annealed blend films. AFM phase images are also shown in Figure 3.13c,d for as-cast and annealed films that exhibit phase segregation size scales of <100 nm and up to >1 μm, respectively, and RMS surface roughness of <10 nm and up to ~50 nm, respectively. AFM micrographs also exhibit evidence for so-called P3HT nanowires recently reported in the literature[91,116] that correspond to highly aggregated P3HT chains in our Raman images (i.e. purple triangles, Figs 3.6 and 3.8). While AFM affords better lateral spatial resolution, it cannot report on morphology-dependent chemical structure changes arising from variations in intra- and interchain order and the relative DOS of aggregated/unaggregated species in complex blended systems. Using the notation of McCullough and co-workers, we attribute regions labeled by purple triangles (R>1.5) as "type 1" P3HT that correspond to highly aggregated chains with an average d-spacing of ~3.8 Å.[134] Regions labeled with blue circles are then assigned as "type 2" aggregates which have a slightly larger d-spacing of 4.47 Å[134] and smaller R values (1<R<1.5). Figure 3.13b shows the structural schemes for these two types of aggregates. It is important to stress that our Raman approach does not provide the ability to resolve individual crystallites but rather regions with distributions of each type. In over-annealed or undoped P3HT films, it is likely that most molecules are in the type 1 form which evident from larger R values. Interestingly, P3HT chains near a PCBM interface exhibit distinctly different behavior than PCBM-poor regions. For example, brown squares

highlight interfacial regions whereby P3HT molecules exhibit slightly higher frequencies possibly due to a disruption in interchain interactions that is shown schematically in Figure 3.13b. However, R values still suggest a significant degree of aggregation which is reasonable due to increased phase segregation in these areas. Lastly, a small fraction of P3HT chains can remain imbedded in PCBM crystallites which is represented by regions labeled by a black diamond. In this regime, interchain interactions do not exist and therefore the molecule should be in the unaggregated (solution-like) state. Because the P3HT structural properties vary significantly in the thin film, it is expected that the rates of important photovoltaic processes, such as charge transport, will also be strongly modulated by heterogeneity effects.

Future experiments will therefore involve resonance Raman imaging studies of the role of P3HT aggregation on photocurrent generation in functioning photovoltaic devices. Based on the results presented in this report, aggregated regions are expected to contribute more to observed current densities owing to the delocalized nature of these species that favors improved charge transport properties. This new approach will allow further examination into the roles of aggregation effects on photocurrent generation that far surpass conventional photocurrent action spectroscopy measurements that instead average over the entire P3HT/PCBM active layer.

3.4 Conclusions

We have shown that the P3HT C=C symmetric stretching mode in P3HT/PCBM blend thin films consists of two distinct contributions from aggregated and unaggregated segments of P3HT. Aggregated ($I_{C=C}^{agg.}$) species correspond to P3HT chains possessing high intra- and interchain order and long conjugation lengths whereas unaggregated ($I_{C=C}^{un.}$) species have less intra- and interchain order and shorter conjugation lengths. The relative concentrations, R, of these species also change with processing conditions from 0.79±0.20 to 2.45±0.77 for as-cast and annealed films, respectively, which is similar to observed changes of aggregated/unaggregated in optical absorption transitions. A direct relationship between the measured Raman R values and the relative DOS of these species is shown which is further corroborated by absorption spectra fitting procedures. The R values determined from resonance Raman spectroscopy, however, are expected to be a better estimate of the relative DOS than values obtained from absorption spectroscopy due to complications arising from Franck-Condon progressions (i.e. different Δ values for aggregated and unaggregated species) in the latter. By mapping morphology-dependent R values and $I_{C=C}^{agg.}$ and $I_{C=C}^{un.}$ frequency dispersion images for as-cast and annealed P3HT/PCBM films, we identify four regions corresponding to, 1) PCBM-rich, unaggregated P3HT (R<1); 2) interfacial P3HT (R~1-4); 3) partially aggregated P3HT (1<R<2); and 4) highly aggregated/crystalline P3HT (R>2). The origin of the change in aggregation state of P3HT is due to increased planarity of the chains that can be determined from intensity ratios of C=C/C-C stretching modes. Images of this

parameter are strongly correlated with R images whereby smaller $I_{C=C}/ I_{C-C}$ values (greater planarity) result in larger R values and therefore greater aggregation of P3HT chains. A simple model has also been proposed to explain these morphology-dependent features in terms of P3HT/PCBM packing characteristics supported by previous AFM, X-ray and optical microscopic imaging reports. This information offers a new glimpse into the factors affecting the spatial variation of aggregation in P3HT that far surpasses the limited picture afforded from conventional ensemble absorption spectroscopy.

Chapter 4

Resonance Raman Spectroscopic- and Photocurrent Imaging of Polythiophene/Fullerene Solar Cells

(This chapter is based on the previously published article, *J. Phys. Chem. Lett.* 2010, 1, 178-182. Copyright permission is obtained from *American Chemical Society* 2009. The other co-authors, Thomas P. Martin, Alan K. Thomas are greatly acknowledged)

4.1 Introduction

Molecular packing interactions (aggregation) have a large influence on the outcomes of charge and energy transfer processes in polymer blend thin film photovoltaic composites,[44,46,75,132,135,136] however, their variation with local (nano- to microscale) morphology and impact on photocurrent generation efficiency in device structures remains poorly understood. Of all organic photovoltaic systems, polymer/fullerene systems are perhaps the most studied and hold the current record for device power conversion efficiencies (~5%).[1,65,112] Phase segregation occurs between these donor/acceptor molecules upon spin-casting into thin films leading to complicated, interpenetrating networks of heterojunction interfaces that facilitate charge generation by exciton dissociation and charge transport. Material performance can be optimized further by post-processing annealing treatments that provide a facile means of tuning film

morphology. Generally, large increases of short circuit current densities (J_{SC}) can be achieved with annealing that are attributed to increased polymer aggregation and order due to increased phase segregation.[68,112] Unfortunately, bulk device characterization studies, such as current-voltage (*J*-*V*) techniques, do not reveal the contributions of different regions to the overall photocurrent generation efficiency. As a result, there is presently intense interest in understanding the microscopic implications of local structure and device performance in polymer/fullerene systems using state-of-the-art scanned probe and optical microscopies.[69,78,137-139] For example, conductive probe atomic force microscopy has emerged as an effective tool for mapping spatial correlations between thin film topography and local photocurrent generation.[69,78,140,141] However, despite the high sensitivity and spatial resolution of these techniques, they cannot interrogate the local polymer aggregation state.

In the following we introduce a new resonance Raman and photocurrent imaging (RRPI) technique to spatially correlate the local polymer aggregation state to morphology-dependent photocurrent generation efficiency and charge mobilities in the prototypical poly-(3-hexylthiophene) (P3HT)/ [6,6]-phenyl-C_{61}-butyric acid methyl ester (PCBM) photovoltaic system. RRPI studies are performed on both as-cast and annealed P3HT/PCBM devices to explore the effect of processing conditions on the polymer aggregation state and photocurrent generation efficiency. The advantages of the RRPI approach over previous spectroscopic and scanned probe studies are: i) strong resonance enhancements in Franck-Condon active vibrational modes, ii) ability to study imbedded

active materials in realistic device structures (i.e. with top metal contacts) under applied bias, iii) large charge transfer quenching reductions in polymer fluorescence backgrounds, and iv) visible excitation wavelengths permit lateral spatial resolution comparable to most near-field scanning optical microscopy (NSOM)[141] and electro-force microscopy[140] (EFM) (~250 nm vs. ~100-200 nm, respectively). Voltage-dependent RRPI studies are also performed that reveal correlations between the local polymer aggregation state to morphology-dependent charge mobilities. In this report, we demonstrate that highly aggregated polymer chains at both polymer/fullerene interfaces and polymer-rich domains generally result in decreased photocurrent generation due to poor charge generation efficiency arising from complete phase segregation of polymer and fullerene components. Overall, the RRPI approach offers new insights into the microscopic implications of the local polymer aggregation and order on photocurrent generation efficiency that are not otherwise obtainable from either ensemble spectroscopy or scanned probe techniques.

4.2 Experimental section

Electronic grade, regio-regular poly-(3-hexylthiophene) (P3HT, MW~87,000 g/mol, Rieke Metals) and [6,6]-phenyl-C61-butyric acid methyl ester (PCBM, Aldrich), were dissolved in anhydrous chlorobenzene at a concentration of 10 mg/mL and stirred overnight in a nitrogen atmosphere and solutions were filtered using a 0.2 μm filter

(Whatman) to remove undissolved solid. Device samples are prepared on glass coverslip substrates coated with indium-tin oxide-ITO (~80 Ω/sq, Metavac Inc.) that were cleaned by rigorous sonication in trichloroethylene, acetone, and methanol each for 15 min. A hole transport layer (PEDOT:PSS, Baytron) was filtered with a 0.45 μm filter (Whatman) and deposited on the ITO glass by spin casting at 2000 rpm followed by heat curing on a hot-plate at 130 ^{o}C for 30 min to remove residual water. P3HT/PCBM blend thin films were prepared in a 1:1 (w/w) ratio and deposited by spin-casting at 600 rpm for 180s producing ~200 nm thick films. Post-processing thermal annealing treatments were performed by heating substrates on a hot plate at 130 ^{o}C for 20 min under dry nitrogen. Aluminum overcoatings (~70 nm) of ~25 mm^2 were deposited on the organic film by thermal vapor deposition at 3 Å/sec in $<10^{-6}$ torr vacuum environment. Leads were connected to the devices using a silver epoxy paste (Dynaloy) and characterized by a source-measure unit (Keithley 2635). External quantum efficiencies (EQE) were measured using a homebuilt apparatus equipped with a KG5 filtered xenon lamp (150 W) and EQE curves were calibrated using a photodiode with a known spectral response under AM1.5 conditions.

The RRPI apparatus is based on a confocal scanning spectrometer described in detail previously. Simultaneous Raman and photocurrent measurements were accomplished by modulating unpolarized laser excitation light with an optical chopper and photocurrents were measured with a combination of a pre-amplifier (current-to-voltage converter, SR570) and lock-in amplifier (Stanford, SR 830). Scan ranges varied

between 10 to 40 μm that were selected on the basis of P3HT/PCBM phase segregated domain sizes determined from atomic force microscopy and optical imaging (not shown).

4.3 Data results and discussion

4.3.1 Ensemble characterization using spectroscopic approaches and I-V curves

By exciting P3HT/PCBM materials on resonance with P3HT absorption transitions (488 nm, 20492 cm^{-1}) large enhancements (~10^5) of Raman-active symmetric stretching backbone vibration cross-sections (i.e., C=C and C-C symmetric stretching modes) are obtained. Resonance excitation also initiates the photovoltaic cycle (i.e., exciton formation, migration, dissociation and charge transport) resulting in photocurrent generation that can be readily measured in a device setting. In a previous report, we showed that the dominant P3HT C=C mode consists of two overlapping transitions that can be decomposed into contributions from aggregated ($I_{C=C}^{agg.}$) and unaggregated ($I_{C=C}^{un.}$) P3HT chains,[142] similar to recent findings from linear optical absorption spectra of undoped P3HT films.[92,96] Raman intensity ratios (R, $I_{C=C}^{agg.} / I_{C=C}^{un.}$) of these two species can then be spatially mapped to uncover the morphology-dependent aggregation state of P3HT on sub-micron size scales. Here we extend our Raman imaging approach to spatially correlate the local aggregation state and photocurrent generation efficiency in P3HT/PCBM device structures.

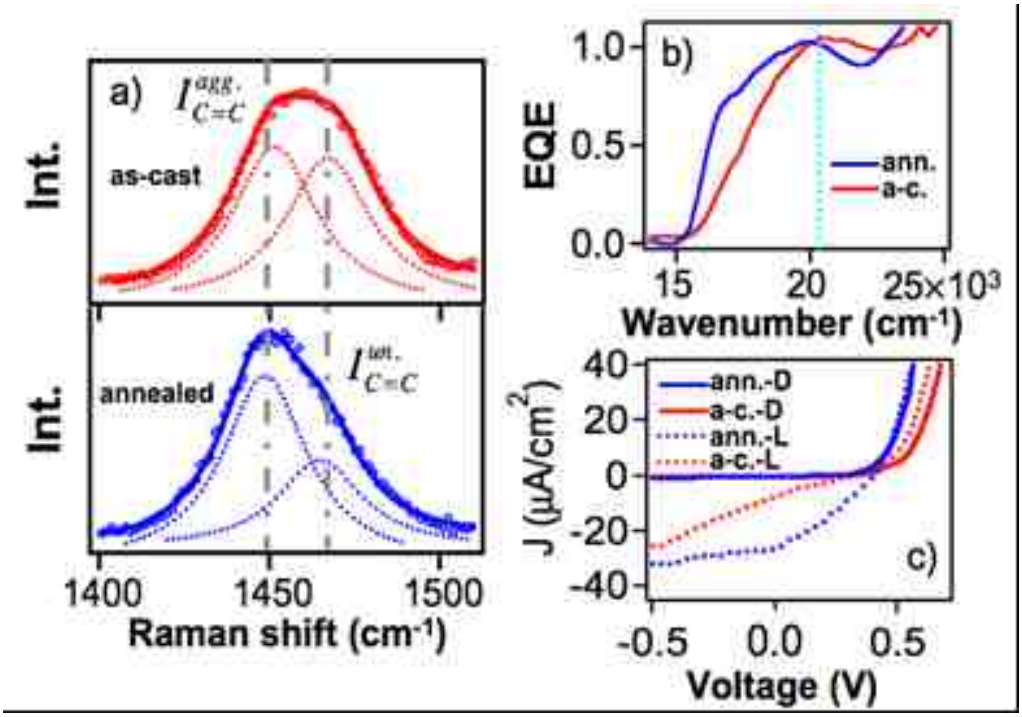

Figure 4.1. a) Raman spectra of as-cast (top panel, red trace) and annealed (bottom panel, blue trace) P3HT/PCBM blend thin film devices with contributions from aggregated ($I_{C=C}^{agg.}$, ~1450 cm^{-1}) and unaggregated ($I_{C=C}^{un.}$, ~1470 cm^{-1}) P3HT chains indicated by dashed gray lines. b) Normalized EQE curves from as-cast (a-c.) and annealed (ann.) P3HT/PCBM devices. The dashed cyan line depicts the excitation wavelength used for RRPI experiments (488 nm). c) Current density-voltage (J-V) curves of as-cast (a-c.) and annealed (ann.) P3HT/PCBM photovoltaic devices recorded in the dark (solid traces) and exposed to white light with an intensity of ~100 mW/cm^2 (dotted traces).

Fig. 4.1 presents representative Raman spectra (a), EQE spectra (b) and device J-V curves in the dark (solid traces) and upon exposure to light (dotted traces; c) for as-cast and annealed films denoted by red (as-cast) and blue (annealed) traces, respectively. Aggregated (~1450 cm^{-1}) and unaggregated (~1470 cm^{-1}) C=C components are labeled in Fig. 4.1a that are decomposed from experimental spectra by fitting two overlapping Lorentzian functions using a procedure described previously.[142] Contributions from PCBM and PEDOT: PSS C=C mode vibrations (~1470 and 1455 cm^{-1}, respectively) in the P3HT C=C mode region were negligible at 488 nm and resulted in <2% error in estimating R values as shown in Figure 4.2. Upon annealing, a significant decrease in the P3HT unaggregated component is observed due to increased phase segregation between P3HT and PCBM components that favors the formation of co-facial, H-aggregate (π-π stacked) structures.[89,92] This trend is also apparent in device EQE curves (Fig. 4.1b) that reveal significant manifestations of increased aggregation as seen from increased vibronic structure resolution in the onset regions (~660 nm, ~15000 cm^{-1}). Device peak EQE's typically varied between 10% and 20% and, interestingly, annealed devices sometimes showed slightly smaller peak EQE's than as-cast devices possibly from complete P3HT/PCBM phase segregation thus degrading charge generation yields and electron transport in PCBM domains.[10] Changes in device performance are also reflected in J-V curves of representative as-cast and annealed devices measured in the dark and upon exposure to white light (~100 mW/cm^2). For example, J_{SC} values from representative as-cast and annealed devices shown in Fig. 4.1c increase from ca. -10 $\mu A/cm^2$ to -30

$\mu A/cm^2$ upon annealing suggesting improved charge transport from increased P3HT aggregation and intra-chain order.

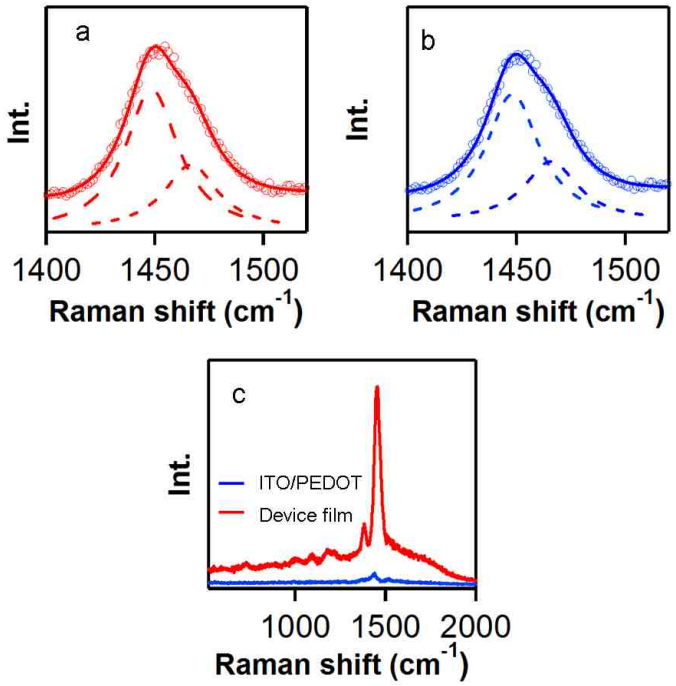

Figure 4.2. ITO/PEDOT Raman contribution: a) Corrected P3HT: PCBM Raman and fit, R = 2.15; b) ITO/PEDOT/P3HT: PCBM/Al Raman and fit, R = 2.19; c) Comparison of two Raman spectra

4.3.2 Raman and photocurrent imaging analysis

Although conventional device characterization and spectroscopic techniques are useful for understanding morphology-dependent variations of overall device performance, they lack the ability to measure contributions from distinct regions of the device. To this end, we perform RRPI studies to spatially correlate the polymer

aggregation state and local photocurrent generation efficiency for as-cast and annealed P3HT/PCBM thin film devices.

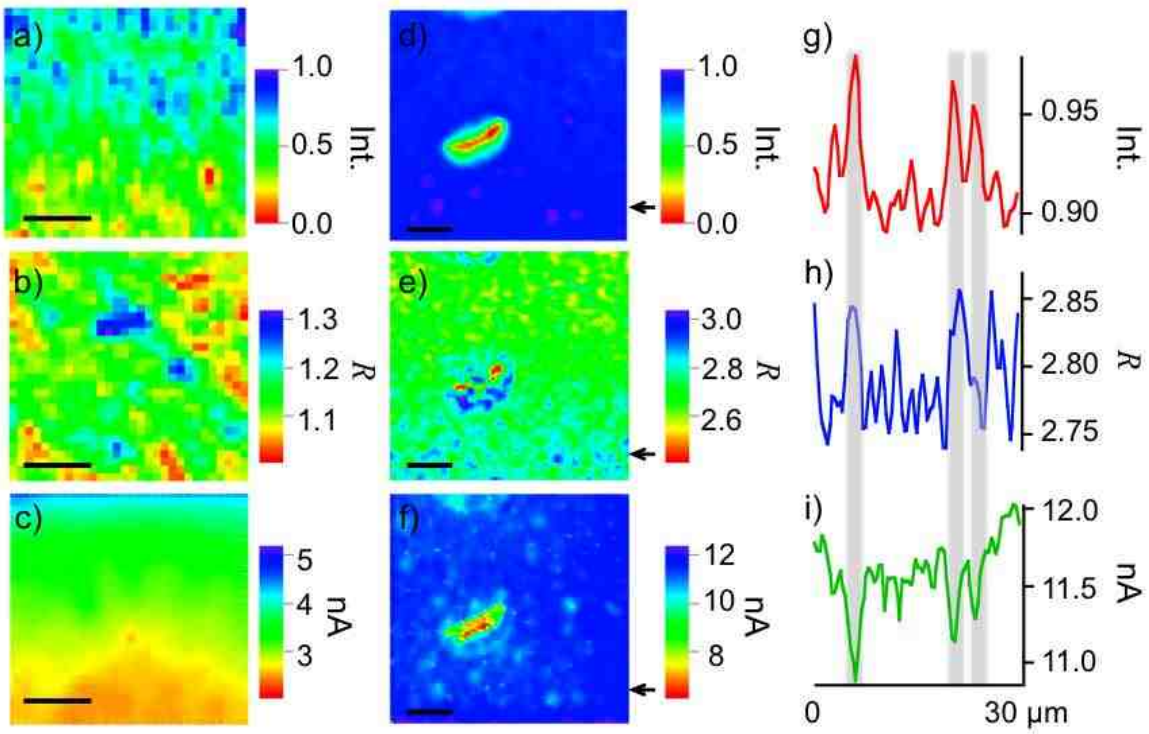

Figure 4.3. a, d) Integrated total C=C mode Raman intensities (normalized), b, e) "*R*" images, and c, f) photocurrent images of as-cast and annealed P3HT/PCBM devices, respectively, measured under the same conditions (Scale bars = 5 μm). g), h) and i) Linescan graphs of Raman intensity (red), *R* (blue) and photocurrents (green), respectively, for annealed devices indicated by arrows on d-f. Gray bars are provided as a guide for the eye.

Fig. 4.3 shows representative Raman C=C mode total integrated intensities (a,d), aggregation state; R (b,e), and photocurrent (c,f) images of as-cast and annealed P3HT/PCBM solar cell device measured under short circuit conditions (0V). Typically, as-cast films exhibit few outstanding features both in Raman and photocurrent images due to the highly interspersed nature of these films, or, P3HT and PCBM phase domains are smaller than our lateral spatial resolution (~250 nm). On the other hand, annealed devices exhibit rich structure due to the formation of PCBM crystallites that are generally needle-like in shape ranging in size from ~500 nm to 5 μm and easily recognizable from small Raman intensities and photocurrents (Figs 4.3c-f). Since the PCBM Raman scattering cross-sections at 488 nm are much smaller than those of P3HT, these signals are probably due to minority amounts of P3HT chains in a solution-like or unaggregated state within the PCBM crystallites. It is interesting to note that regions of high intensity and aggregation (i.e. larger R values, Fig. 4.3e) in the annealed device generally correspond to lower photocurrents than other areas in the P3HT-rich regions. This correlation is clearly demonstrated in linescan graphs of intensity (g), R (h) and photocurrent (i) that are generated from the region depicted by the small arrows in Figs. 4.3d-f. For example, P3HT-rich regions with normalized intensities >0.9 and R values >2.75 exhibit lower photocurrents than surrounding regions which are highlighted by gray bars for three such regions in the linescan graphs. Reductions of photocurrents for highly aggregated regions are surprising since it is widely believed that increased order and aggregation is key for attaining efficient multi-dimensional charge transport.

Figure 4.4. Optical image of one of typical PCBM crystal and halo ring around it

P3HT/PCBM interfaces also exhibit strong correlations between the aggregation state and photocurrent generation whereby the average R value surrounding PCBM crystallites is much larger on average (i.e. >3) than surrounding P3HT-rich areas. Photocurrents are also correspondingly smaller at interfaces due to complete P3HT/PCBM phase separation which is evident from the 'halo'-type rings around PCBM crystallites observed in both photocurrent and optical images of annealed P3HT/PCBM films as shown in Fig. 4.4. Because highly aggregated regions are virtually devoid of PCBM molecules, reductions in photocurrents for both P3HT-rich and P3HT/PCBM interface regions are most likely due to insufficient charge generation, a phenomenon also observed in bulk device EQE and I-V studies for films that are annealed for longer times and at higher temperatures.[60,110,143] Schwartz and co-workers have also recently demonstrated that

annealing causes reductions in charge mobilities in PCBM crystallites[68] that may also contribute to similar photocurrent reductions at P3HT/PCBM interfaces in our results. In order to understand the impact of the local aggregation state to device performance figures of merit, photocurrents are recast in terms of device EQE's which are found to vary from ~0.5×10^{-4} to 3.0×10^{-4} at 488 nm. These values are much lower than ensemble averaged EQE's measured under AM1.5 conditions in Fig. 4.1 probably due to saturation of the charge generation step and bimolecular recombination processes that occur at higher excitation intensities (~10^3—10^4 W/cm^2) required for generating high signal-to-noise Raman spectra.[144] The results shown in Fig. 4.3 demonstrate that while increased phase segregation and aggregation of P3HT chains opens up both intra- and interchain charge transport pathways[88] improved device performance can be seriously mitigated by reduced charge generation efficiency in these regions.

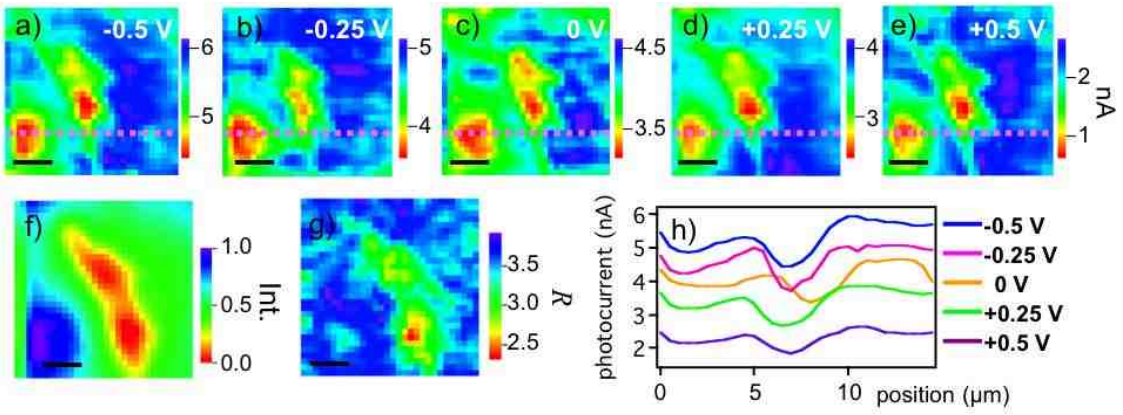

Figure 4.5. Voltage dependent photocurrent images of an ITO/PEDOT/P3HT: PCBM/Al annealed device: a-e) display photocurrent images under -0.5 V, -0.25 V, 0 V, 0.25 V, 0.5 V applied bias, respectively. f) and g) show normalized Raman C=C intensity and R images measured at 0 V (scale bar size = 3 μm). h) Linescan graphs at each applied bias indicated by the dotted purple line through panels a-e.

We have shown thus far that the local polymer aggregation state has a large impact on photocurrent generation efficiency under short-circuit conditions (0 V). It is now informative to explore the effect of applied device bias on local photocurrent generation that, upon comparison to Raman images, can shed light on the role of the local polymer aggregation state on charge transport properties. Based on previous bulk polymer device J-V and time-of-flight photocurrent studies, charge mobilities typically exhibit a strong dependence on the applied electric field indicative of hopping-type charge transport.[145-147] Unfortunately these bulk measurements do not reveal whether specific regions or domain sizes and compositions exhibit different charge mobility

characteristics. Figs. 4.5a-e show voltage-dependent photocurrent images of P3HT/PCBM device structures measured with applied biases ranging from 0.5 V to +0.5 V spanning the normal operating window of organic optoelectronic devices, i.e. short circuit and open circuit conditions. Raman intensity and R images acquired at 0 V are shown for comparison in Figs. 4.5f and 4.5g but otherwise showed little change with applied bias (<5%) which is expected under resonance excitation conditions.[85] Beyond the change in the average photocurrent for each applied bias, it is noteworthy that the photocurrent topographies and linescan profiles change presumably due to morphology-dependent charge mobility mechanisms arising from fluctuations in the polymer aggregation state (i.e., intra- vs. intermolecular transport). Fig. 4.5h shows linescan graphs plotted in the vicinity of a PCBM crystallite (dashed purple line) from each voltage-dependent photocurrent image that reveal further insight into morphology- and voltage-dependent charge mobilities. On average, photocurrent production decreases from -0.5 V to +0.5 V, the latter being close to the open circuit voltage measured from ensemble J-V curves (Fig. 4.1c). Photocurrent linescan profiles, on the other hand, show marked changes from 0 V for both positive and negative bias near P3HT/PCBM interfaces. This effect qualitatively resembles that of previous photocurrent imaging studies on polyphenylenevinylene/PCBM films using electro-force/photocurrent microscopy that show 'turn-on' effects with increasing negative bias.[78] The bias-dependent changes in photocurrent generation in Fig. 4.5 could result from distortions due to lateral carrier diffusion effects but are ruled out owing to the large mismatch in

optical spatial resolution and typical carrier migration lengths (i.e. ~250 nm vs. ~10 nm). Instead it is proposed that interface charging effects arising from trapping processes at P3HT/PCBM interfaces are the origin for the observed changes in both bias-dependent photocurrent images and linescans.

4.4 Conclusions

In summary, the RRPI results reveal that the largest photocurrent generation occurs in the P3HT-rich regions with intermediate aggregation levels, which is surprising since current understanding predicts that high P3HT aggregation and crystallinity should favor improved transport and photocurrent densities.[148] As suggested previously, the incomplete phase segregation between P3HT and PCBM components is essential for achieving maximum charge generation yields whereas complete phase segregation, while promoting efficient and multi-dimensional charge transport, can actually be detrimental to device performance owing to insufficient charge generation. Voltage-dependent Raman and photocurrent images provide more insight into this morphology-dependent tradeoff between charge generation and transport by revealing intrinsic fluctuations of charge mobilities with local morphology. These measurements also suggest that new materials design approaches are needed in order to avoid both carrier generation losses due to reduced interface area as well as recombination and trapping processes that dominate as-cast films possessing small phase segregated domain sizes. Overall, the RRPI technique is an effective tool for evaluating the role of local structure on

photocurrent generation that, owing to the strong charge transfer character of organic donor/acceptor composites, can be applied to many candidate photovoltaic materials systems.

Chapter 5

Understanding Morphology-Dependent Polymer Aggregation Properties and Photocurrent Generation in Polythiophene/fullerene Solar Cells of Variable Composition

(This chapter is based on a previously published article, *J. Phys. Chem. C*. 2010, 114 15121-15128. The copyright permission is obtained from *American Chemical Society* 2010. The other co-authors, Thomas P. Martin, Edwards T. Niles, Adam J. Wise, and Alan K. Thomas are greatly acknowledged)

5.1 Introduction

The ability of conjugated polymer molecules to form extended networks of co-facial, π-π stacked chains in thin films is vital for achieving optimal performance in optoelectronic device settings.[6,88,148,149] In particular, these structures (herein referred to as aggregates) have modified electronic structures that have important implications on charge and energy transfer processes.[2,150,151] Although the establishment of aggregated polymer networks underlies the performance of all polymeric optoelectronic devices, it is especially important in solar cells due to the need to add substantial amounts of electron acceptor materials (i.e. fullerene derivatives) to polymers that can effectively break up these extended networks. This effect can be partially alleviated by post-processing

annealing treatments that permit the fine-tuning of polymer/fullerene morphologies (i.e., phase domain size and composition) and polymer aggregation properties.[81,152] Unfortunately a detailed knowledge of the types, amounts and spatial variation of aggregated polymer chains throughout thin films has been lacking as well as the specific morphological and composition factors that regulate aggregate formation. Moreover, the impact of these structures on photocurrent generation in solar cells has also been difficult to ascertain on the sub-micron size scale and usually must be inferred from processing-dependent changes in ensemble current-voltage (I-V) and external quantum efficiency (EQE) curves.[46,63,153] Herein, we systematically perturb thin film morphologies and compositions in a prototypical polymer/fullerene solar cell material to investigate the types and spatial distributions of aggregates and directly correlate these features to local device photocurrent generation efficiency that may help guide new materials design schemes to control the amount and spatial location of aggregates to maximize device performance.

Thin film solar cells consisting of poly-(3-hexylthiophene) (P3HT) and [6,6]-phenyl-C_{61}-butyric acid methyl ester (PCBM) blends in a ~1:1 w/w ratio have consistently achieved power conversion efficiencies of ~6%, making them the current leader in this field.[49,112,154] It is widely accepted that the dominant contributor to high efficiency in this system is the establishment of highly ordered (crystalline) polymer regions that promote efficient charge transport.[121,134,155] Molecular structure factors such as side chain group size, molecular weight, polydispersity and P3HT/PCBM loadings all

play essential roles in determining the film morphology characteristics and, most importantly, the local aggregation state of P3HT chains. Interestingly, optimal P3HT/PCBM morphologies have arrived from years of extensive, top-down trial and error studies involving variation of loadings and processing conditions. Only recently, X-ray scattering studies of P3HT/PCBM blends and other promising polymeric candidate systems have demonstrated the importance of key steric factors that must be considered in the design of new material processing and synthetic schemes.[156]

Because the types and amounts of aggregated P3HT chains vary substantially throughout a thin film structures, a sensitive and high spatial resolution imaging technique is required to detect morphology-dependent variation of these structures in a functioning device and correlate their properties to local performance. Previous studies of aggregated polymer chains, particularly for the P3HT system, have been carried out by optical absorption and emission spectroscopy followed by theoretical lineshape analyses that specifically account for aggregation effects.[129,157] In P3HT, H-type (i.e. face-to-face) aggregation is most prevalent that results in non-Poissonian optical lineshapes that are also highly sensitive to film processing conditions that modify chain packing characteristics. Spano and co-workers developed a weakly coupled H-aggregate model to describe these lineshapes in terms of an exciton bandwidth parameter (interchain electronic coupling) that depends on both intra- and intermolecular order effects and conjugation lengths.[90,92,96] By fitting H-aggregate lineshapes in polythiophenes, it has been possible to extract microscopic details about the interplay between polymer

structure and electronic properties in addition to quantifying the relative amounts of aggregated (ordered) and unaggregated (solution-like) polymer chains. However, absorption spectroscopy studies of aggregates in polymer thin films, especially P3HT/PCBM blends for solar cells, average over many nano- and microscopic size domains that vary in both composition and structure thus masking the contributions of different regions of polymer aggregation types to the overall lineshapes. On the other hand, direct study of the role of polymer aggregation on photocurrent production in functioning devices can be fraught with complications from other materials necessary for proper device function (i.e. charge transport layers). To overcome these limitations, we use a highly selective resonance Raman and photocurrent imaging technique[142,158] that is capable of uncovering specific details about the local polymer aggregation state as well as the contribution to photocurrent generation.

We fabricate P3HT/PCBM solar cell devices with variable PCBM w/w loadings that, due to the lack of evidence of ground state charge transfer transitions, only affect the ability of P3HT molecules to form aggregates thus affecting energy transfer, charge generation and transport processes in the photovoltaic cycle. Absorption spectroscopy measurements are first performed to estimate the average amounts of aggregated and unaggregated (or, solution-like) P3HT chains by analyzing spectral lineshapes using the weakly coupled H-aggregate model of Spano and co-workers. Resonance Raman spectroscopy and imaging are then used to quantify and spatially map polymer aggregation properties on sub-micron scales within functioning devices. This is

accomplished by using the P3HT C=C symmetric stretching band that can be decomposed into contributions from aggregated and unaggregated chains.[142] Photocurrent imaging is also performed in a simultaneous manner to establish direct correlations between aggregation characteristics and photocurrent generation efficiency that reveal the structure-function landscapes of these systems in realistic device structures.[158] A major advantage of this approach is that, by careful selection of excitation energies, Raman signals from only the P3HT component can be resolved owing to the large resonance enhancements of P3HT Raman cross sections (~10^5) relative to all other material components in the device structure. This feature permits the study of embedded polymer chains and their aggregation properties in a highly selective manner thus avoiding unwanted complications from overlapping bands from hole transport layers and PCBM that could easily dominate in IR absorption and off-resonance Raman conditions.

5.2. Experimental section

Electronic grade, regio-regular poly-(3-hexylthiophene) (P3HT, MW~87,000 g/mol, Rieke Metals) and [6, 6]-phenyl-C61-butyric acid methyl ester (PCBM, Aldrich), were dissolved in anhydrous chlorobenzene at a concentration of 10 mg/mL and stirred for ~12 hours in a nitrogen atmosphere. Solutions were filtered using a 0.2 μm filter (Whatman) to remove any undissolved solid before use. Thin film samples for absorption spectroscopy were prepared on glass substrates and devices were fabricated on indium-tin

oxide (ITO) coated glass substrates that were cleaned by sonication in trichloroethylene, acetone, and methanol for 15 min each. A hole transport layer poly(3,4-ethylenedioxythiophene):poly(styrenesulfonate) (PEDOT:PSS, Baytron) was deposited on ITO surfaces by spin casting at 2000 rpm followed by heat curing at 130 ^{o}C for 30 min to remove residual water. P3HT/PCBM thin films were next deposited by spin-casting at 600 rpm for 180s with 1:1, 1:2, 1:3 and 1:4 w/w ratios. Post-processing thermal annealing treatments were performed by heating samples on a hot plate at 110 ^{o}C for 20 min under a nitrogen environment. Aluminum overcoatings were then deposited on the P3HT/PCBM films by thermal vapor deposition using a shadow mask with ~25 mm^2 squares to define the device active area. Leads were connected to the devices using a silver epoxy paste (Dynaloy).

P3HT/PCBM thin films were characterized by absorption spectroscopy and corrected for wavelength-dependent variations in the detector response. Device EQE and I-V characterization measurements were measured using a homebuilt apparatus equipped with a KG5 filtered 150 W xenon lamp and a current-voltage source-measure unit (Keithley 2635). EQE's were scaled using a photodiode with a known spectral response under AM1.5 illumination conditions. Resonance Raman and photocurrent imaging (RRPI) of P3HT/PCBM solar cells of variable PCBM loadings were performed using a scanning confocal spectrometer system described in detail previously. Excitation intensities were kept in the range of ~1 kW/cm^2 and no photodegradation effects were observed on the timescales of spectral acquisition (~100 ms) per scan point. Excitation

power dependent photocurrent measurements were performed to verify response linearity and that deviations from higher order effects such as exciton-exciton annihilation were minimal within the excitation intensity range used, which is shown as Figure 5.1. Survey optical and AFM images were also measured to help guide the selection of image scan range for each w/w loading (see Figure 5.2).

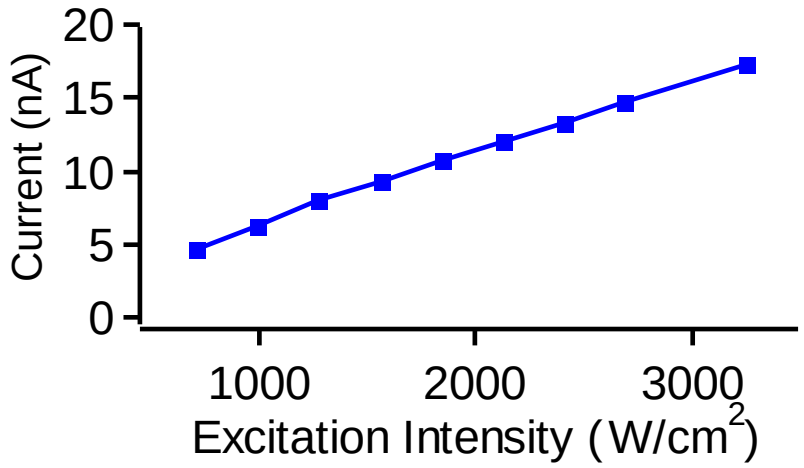

Figure 5.1. Excitation intensity dependent photocurrent response generated from a 1:1 w/w P3HT/PCBM device illuminated in a widefield mode.

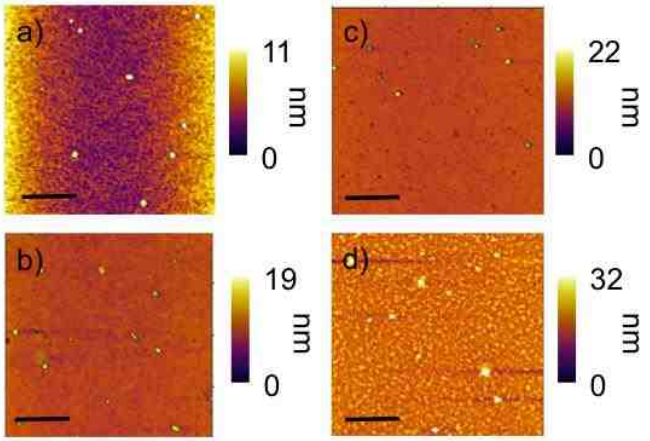

Figure 5.2. Survey AFM micrographs of a) 1:1, b) 1:2, c) 1:3, and d) 1:4 annealed P3HT/PCBM thin films (scale bars = 5 μm).

5.3 Data results and discussion

Linear optical absorption and emission spectroscopy have so far proven most useful for studying aggregation effects and the relative amounts of aggregated species in polythiophene thin films.[92,96,129,157] In particular, the weakly coupled H-aggregate model developed by Spano and co-workers has been successfully applied to polythiophenes to describe their optical absorption and emission lineshapes in terms of the interchain electronic coupling (exciton bandwidth) that is dependent upon both intra- and interchain microscopic order and conjugation lengths.[21-24] We previously extended this model to P3HT/PCBM (1:1 w/w) films where the amounts and type of aggregated chains were determined from both Raman and optical absorption spectra for different processing

conditions.[142] Herein, the PCBM weight fraction and annealing treatments are varied in a controlled manner to modulate P3HT aggregation properties.

5.3.1 Absorption and Raman spectra analysis

We first qualitatively consider the impact of variable PCBM loadings and annealing treatments on the P3HT aggregation state by studying the averaged optical and vibrational spectroscopic signatures of P3HT/PCBM thin films. Figure 5.3 presents absorption spectra in the P3HT π-π* region (~15000—25000 cm^{-1}) and Raman spectra depicting the P3HT symmetric stretching backbone region (i.e. C-C, ~1380 cm^{-1}, and C=C, ~1455 cm^{-1}, modes) for as-cast a), b) and annealed c), d) P3HT/PCBM thin films of varying PCBM weight fraction (i.e. 1:n; n=1—4), respectively. In order to observe the average Raman response from these variable loading films, the spectra in Fig. 5.3b,d were obtained by averaging >900 individual Raman spectra over a 20-30 μm area. Because Raman spectra are excited on resonance with π-π* transitions, only Franck-Condon active vibrational modes are selectively enhanced. This feature makes spectra quite simple and the relative intensities of Raman bands are highly sensitive to local fluctuations in composition and morphology that can be exploited to map the P3HT aggregation state.

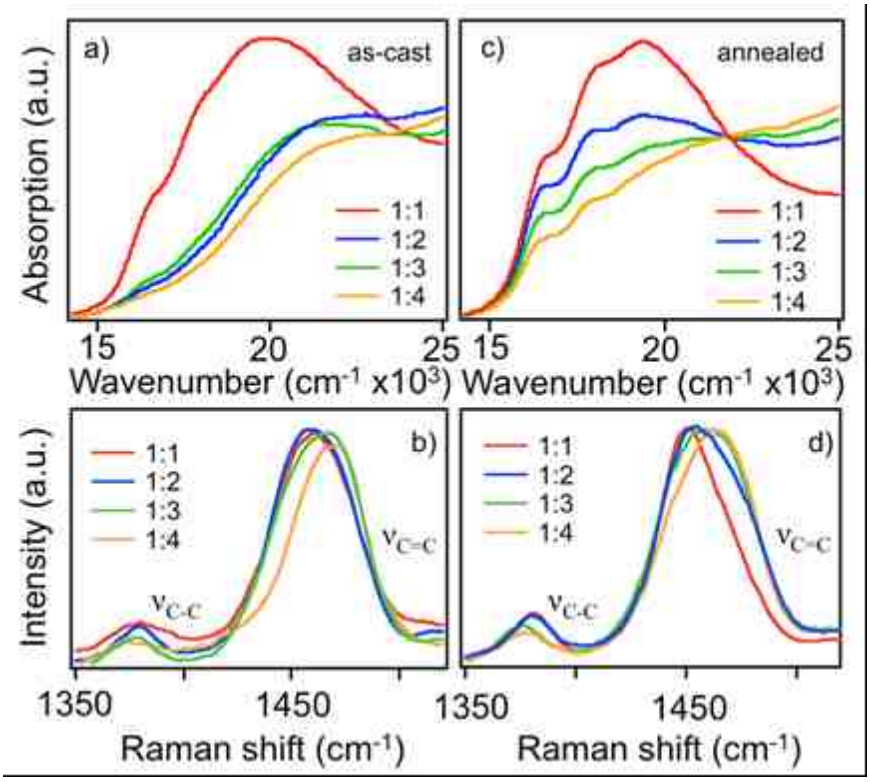

Figure 5.3. Absorption and averaged Raman spectra of 1:1, 1:2, 1:3 and 1:4 P3HT/PCBM as-cast a); b) and annealed, c); d) blend thin films. Raman spectra highlight the P3HT symmetric stretching backbone region with the C=C and C-C modes labeled.

Absorption and Raman spectra in the P3HT region of both as-cast and annealed films show progressive overall blue-shifts for increasing PCBM content. Interestingly, absorption and Raman lineshapes of as-cast films with >1:1 w/w loadings change very little and closely resemble dilute solution P3HT spectra (see below) and marked reductions in signal-to-noise ratios are also observed with increased PCBM content.

Upon annealing, absorption maxima show apparent red-shifts of the P3HT component of up to ~1000 cm^{-1} and corresponding P3HT C=C symmetric Raman bands show ~20 cm^{-1} red-shifts. Spectroscopic evidence of aggregated P3HT chains is most apparent from the onset regions of annealed P3HT/PCBM absorption lineshapes (Fig. 5.3c) where dominant progressions in the P3HT symmetric stretching C=C mode (~1400 cm^{-1}) are clearly resolved. Surprisingly, vibronic linewidths near the P3HT onset region diminish with increased PCBM concentrations but become increasingly congested from overlapping transitions from unaggregated P3HT chains at energies >20000 cm^{-1} (see below). Comparatively, P3HT C=C Raman modes exhibit high sensitivity to annealing treatments and PCBM content which is shown in the following to originate from changing amounts of aggregated and unaggregated P3HT chains. Other P3HT skeletal vibrations such as C-C intra- and inter-ring modes as well as thiophene ring C-H bending modes also show marked changes with increasing PCBM loading that can be attributed to subtle changes in chain planarity.[159]

Previous absorption and Raman spectroscopic studies of P3HT/PCBM composite films have attributed the large observed spectroscopic lineshape changes and band maxima shifts to changes of either conjugation lengths or crystallinity (order) or both.[118,160,161] In this framework, the blue-shifts of absorption and Raman spectra with increasing PCBM content result from more disordered P3HT chains due to the ability of PCBM to break up aggregated polymer chains. On the other hand, red-shifts of absorption and Raman spectra with annealing are rationalized by increased phase

segregation that promotes polymer aggregation. While qualitatively useful, these largely phenomenological generalizations often fail to capture the impact of local morphology and composition on these important material structure characteristics and their contribution to local device performance. We now delve further into these structure-property relationships and establish useful correlations between the polymer aggregation state and device photocurrent generation on the sub-micron size scale.

5.3.2 Uncovering Spectroscopic Contributions of Aggregated P3HT chains

The weakly coupled H-aggregate model is now used to fit the resolved absorption onset region (i.e. 0-0 and 0-1 vibronic transitions) and estimate the effect of variable PCBM content on the type and amounts of aggregated P3HT chains. The model has a single electronic origin with a vibronic progression in the P3HT C=C symmetric stretching mode (ca. 1400 cm^{-1} in the excited state) and a constant Huang-Rhys factor (S) of 1.0. The Gaussian vibronic linewidth (σ), energy of electronic origin ($E_{0\text{-}0)}$ and exciton bandwidth (W) parameters are then adjusted to obtain a good fit of 0-0/0-1 absorbance ratios. The justification for keeping S fixed in the fitting routine is the fact that inter-chain interactions usually dominate over intra-chain effects, such as bond distortions, from the unique affinity of P3HT to form extended aggregated structures.[96] Fit parameters are collected in Table 5.1 and a slight decrease of these parameters with increased PCBM content is observed.

Table 5.1. Fit parameters used for calculating aggregate component spectra.[a]

P3HT/PCBM w/w ratio	W (cm^{-1})	FWHM (cm^{-1})[b]	E_{0-0} (cm^{-1})[b]
1:1	980	850	16530
1:2	805	830	16500
1:3	805	835	16490
1:4	870	845	16480

[a] Huang-Rhys factor (S) was set to 1.0 and the vibrational frequency for the dominant progression forming mode (C=C) was fixed at 1400 cm^{-1} for all simulations. [b] Fit parameter tolerance was approximately +/- 4%.

Figure 5.4 shows experimental spectra (solid red traces with open squares) and fit spectra (dotted trace) for 1:1 a), 1:2 b), 1:3 c), and 1:4 d) w/w P3HT/PCBM annealed thin films. Unfortunately, it was not possible to obtain reliable fits from as-cast films of >1:1 loadings due to the very small signal- to-noise ratios near the aggregate absorption onset region and we instead concentrate solely on annealed film data. By fitting only the resolved vibronic onset region of the spectrum (i.e. 0-0/0-1 vibronic peaks) it is immediately apparent that experimental spectra cannot be reproduced by the H-aggregate model alone because of overlapping transitions from unaggregated P3HT chains that increase with PCBM loading. Fit spectra are then subtracted from experimental spectra to reveal contributions from unaggregated chains (dashed traces) that lack resolved vibronic structure presumably due to large displacements of low frequency torsional vibrations and inhomogeneous broadening.

For comparison, we show P3HT dilute solution spectra (solid blue trace with open circles) that have similar energies and linewidths as difference spectra.

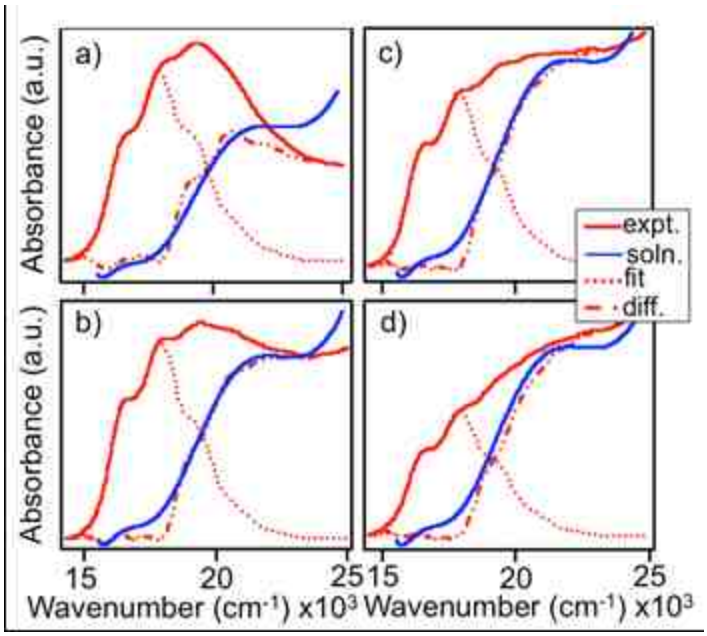

Figure 5.4. Experimental absorption spectra (solid red traces with squares) and fits (dotted traces) using a weakly coupled aggregate model for 1:1 (a), 1:2 (b), 1:3 (c) and 1:4 (d) P3HT/PCBM annealed thin films. Fit spectra are subtracted and difference spectra (dash-dot traces) plotted against dilute P3HT solutions (solid blue traces with open circles).

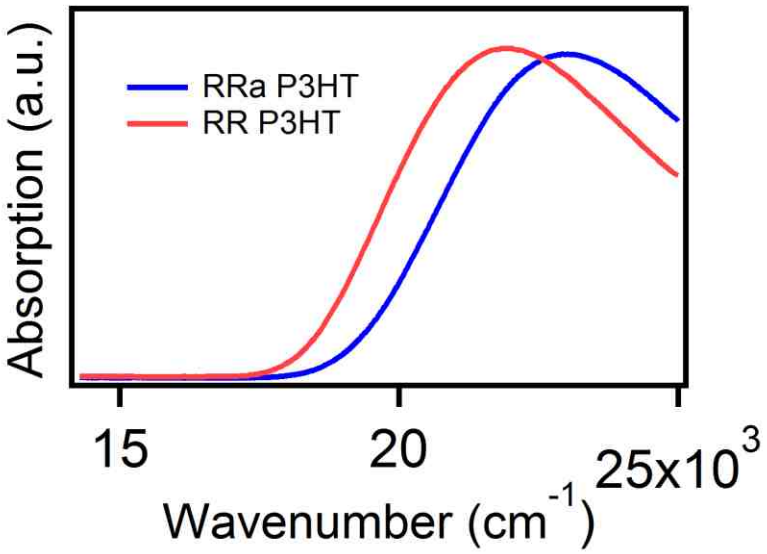

Figure 5.5. Absorption spectra of regio-random P3HT solution (blue) and unaggregated components from P3HT solution (red).

For comparison, absorption lineshapes of regio-random P3HT thin films have similar features as the dilute solution and unaggregated contributions albeit slightly higher transition energies (see Figure 5.5) but, nonetheless, confirm that unaggregated chains in P3HT/PCBM blends more closely resemble dilute solution conformations with large conformational disorder. Comparing fit spectra with increased PCBM content reveals small, but discernible, increases in vibronic linewidths and 0-0 absorption strengths in addition to slight red-shifts that correspond to reductions in σ, W, and $E_{0\text{-}0}$ fit parameters, respectively (see Table 5.1). Generally, smaller 0-0/0-1 ratios are indicative of larger exciton bandwidth and smaller conjugation lengths. On the other hand, increases in 0-0/0-1 ratios indicate reduction of exciton bandwidths due to increased intra-chain

order and conjugation lengths. From the small increases in 0-0/0-1 absorption ratios it is apparent that, while the overall amount of aggregated chains decrease, these chains are self-aggregating into ordered conformations which is expected in more PCBM-rich films since extended interchain interactions are less likely to form. A high correlation coefficient (~0.92) was also found for the exciton bandwidth and linewidth fit parameters that further supports a shift toward increased intra-chain order and a narrower distribution of conjugation lengths with increased PCBM loading.

Alternatively, the observed lineshape changes for the aggregated P3HT component absorption spectrum could arise from a "chemical pressure" effect whereby larger PCBM contents (domain size) cause a reduction in the Huang-Rhys factor by squeezing the smaller P3HT domains due to unfavorable thermodynamic mixing factors. In order to determine whether these effects are at play in P3HT/PCBM annealed thin films, we allowed the Huang-Rhys parameter to vary while holding the exciton bandwidth term fixed at 980 cm^{-1} from the 1:1 w/w film. Upon increasing the PCBM loadings from 1:1 to 1:4, it was found that the Huang-Rhys parameter decreased from 1.0 to 0.76. Assuming no mixing of vibrational modes this corresponds to a decrease of average C=C bond distances of ~0.05Å. Because distortions of this size are only likely to occur under applied hydrostatic pressures of >10 kbar, [162]we instead propose that P3HT chains self-aggregate with larger PCBM content.

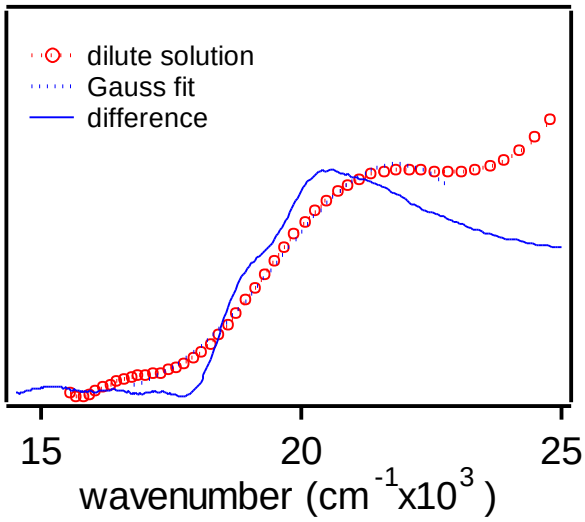

Figure 5.6. Fitting procedure used to determine the relative amounts of unaggregated chains. Dilute solution P3HT spectra are scaled to the onset and peak absorbance of difference spectra obtained from subtracting out the fit from the weakly coupled H-aggregate model from experimental blend thin film data. A Gaussian function is then fitted to the dilute solution spectrum to estimate the contribution of unaggregated chains without complications from overlapping PCBM transitions.

From the above fitting procedure, it is useful to estimate the relative amounts of aggregated and unaggregated chains in annealed P3HT/PCBM films. However, increased spectral overlap between unaggregated P3HT transitions and PCBM absorption onsets with higher PCBM content can make accurate estimates difficult. In order to avoid complications from PCBM absorption at higher frequencies (i.e. >23000 cm^{-1}) a Gaussian function is fitted to the P3HT dilute solution spectrum and scaled to match the onset of the difference spectrum generated from the fitting procedure described above

(see Figure 5.6). The ratio of integrated areas from the calculated (aggregate) spectrum and the scaled Gaussian lineshape representing the contribution from unaggregated chains P3HT components ($A_{agg.}/A_{unagg.}$) was found to decrease with higher loadings, namely, 2.6 (1:1), 1.88 (1:2), 1.44 (1:3) to 1.10 (1:4). This decrease is consistent with the fact that increased PCBM content can effectively prevent P3HT chain aggregation. In addition to complications arising from the overlap of PCBM absorption onsets, the markedly different lineshapes (Franck-Condon factors) of aggregated and unaggregated components highlight the inherent difficulty of estimating the relative contributions of these chains to the overall absorption lineshape. Fortunately, more reliable estimates can be obtained from Raman spectroscopy that also provides the basis for spatially mapping this important structural feature of the P3HT component on the sub-micron size scale.

5.3.3 Mapping the Spatial Distributions of Aggregated P3HT chains

Several research groups have previously employed Raman spectroscopy for understanding the effect of processing conditions on P3HT/PCBM blend thin film morphologies. In particular, large overall red-shifts of the P3HT C=C symmetric stretching Raman bands are observed after annealing[120,123,127] that are commonly explained in terms of increased polymer conjugation lengths and crystallinity. However, in a previous report, we demonstrated that this band can be decomposed into contributions from both aggregated and unaggregated chains with characteristic frequencies of ~1450 cm^{-1} and ~1470 cm^{-1}, respectively, which are consistent with

spectra from ordered (crystalline, regio-regular) and amorphous (solution, regio-random) of related thiophene systems.[85,133,163] In this model, the large overall spectral shifts occurring upon annealing are rationalized in terms of the relative amounts of both species changing with processing conditions that cause apparent shifts in band maxima. This model primarily demonstrates the importance of interchain effects (similar to absorption lineshape changes) since the overall P3HT C=C frequency shifts are too large to occur by increases in conjugation lengths alone. Moreover, the Raman approach for quantifying the amounts of aggregated and unaggregated species is much more reliable than absorption spectroscopy since there are no complications from multiple Franck-Condon vibrational progressions and overlapping PCBM bands. A major goal of this paper will be to extend this model to understand how the P3HT aggregation state is affected by structural perturbations from variable PCBM loadings and determine how both intra- and intermolecular factors and phase segregation regulate the types and distributions of aggregates.

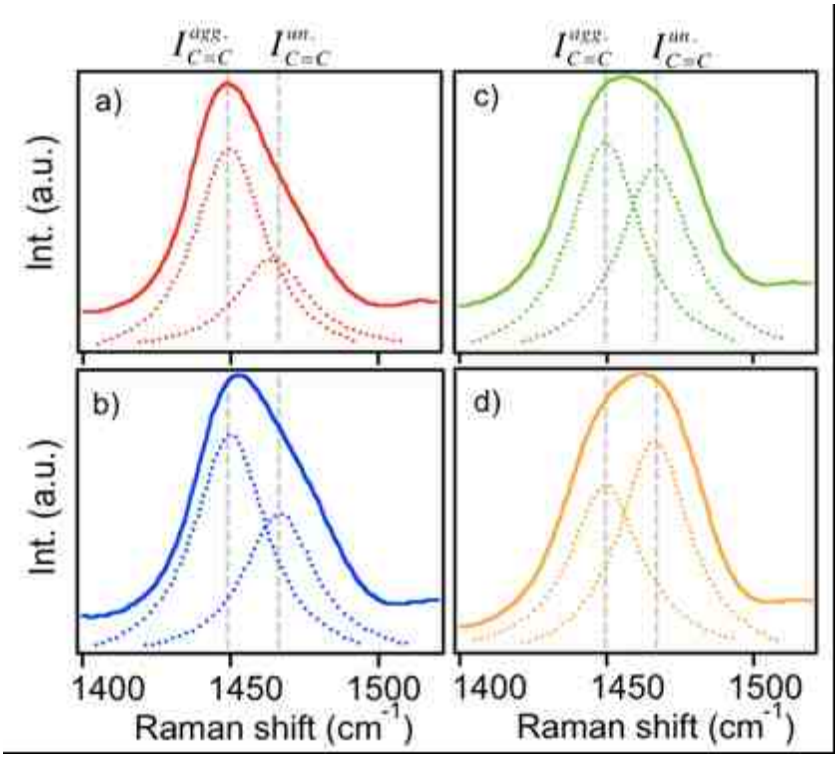

Figure 5.7. Raman spectra of a) 1:1, b) 1:2, c) 1:3, and d) 1:4 w/w P3HT/PCBM thin films in the C=C symmetric stretching mode region of the P3HT component generated by averaging over 900 spectra from imaging experiments (see Fig.5. 9). C=C bands are decomposed into contributions from aggregated (ca. 1450 cm^{-1}) and unaggregated (ca. 1470 cm^{-1}) chains.

Similar to absorption spectra characteristics, P3HT C=C Raman lineshapes (shown in Figs. 5.3b, d) also show progressive blue-shifts due to an increase in the amounts of unaggregated P3HT chains with increased PCBM content. In order to quantify the degree of P3HT aggregation from Raman spectra, we use idealized Lorentzian lineshape functions for the two components representing both aggregated

(1450 cm^{-1}) and unaggregated (1470 cm^{-1}) P3HT chains are fitted to the experimental C=C Raman band and we use the ratios of integrated areas of these components to estimate the P3HT aggregation ratio, or "R" value ($I_{C=C}^{agg.} / I_{C=C}^{un.}$). Figure 5.7 shows Lorentzian fits of averaged Raman spectra of P3HT/PCBM of variable loadings: 1:1 a), 1:2 b), 1:3 c), and 1:4 d). As the PCBM concentration increases, the unaggregated component increases confirming that P3HT chains are in increasingly twisted or solution-like conformations. From averaged spectra, the ratios of aggregated/unaggregated P3HT chains were found to be 3.2 (1:1), 1.9 (1:2), 0.9 (1:3), and 0.7 (1:4) which are comparable to estimates generated from absorption fits described above. Interference from both PCBM and PEDOT:PSS hole transport materials C=C modes (~1465 cm^{-1}) have a negligible effect on "R" values even at higher loadings due to the large disparity in Raman cross sections that are estimated to be several orders of magnitude smaller than that of P3HT for the excitation wavelength used (488 nm).

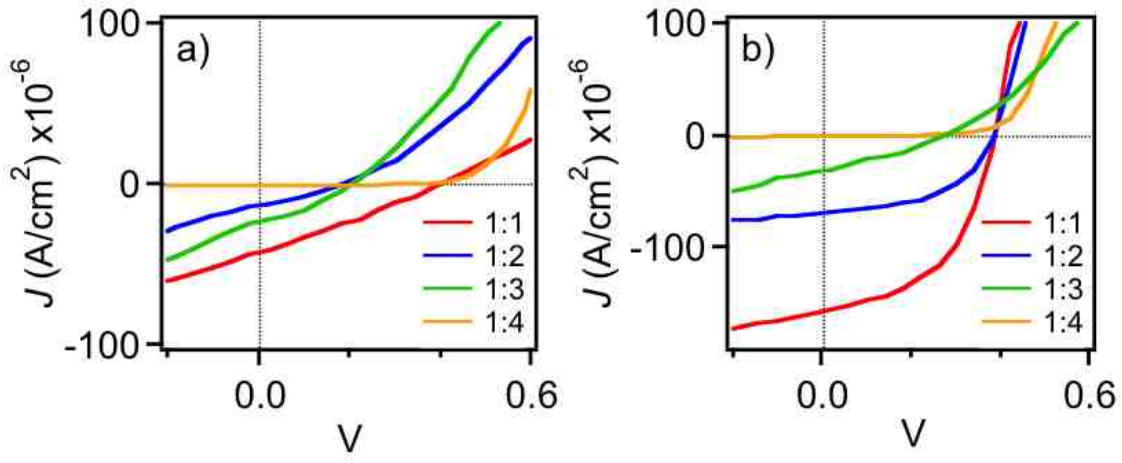

Figure 5.8. Current-voltage (I-V) curves for a) as-cast and b) annealed P3HT/PCBM devices of varying composition under exposure to white light (~100 mW/cm^2).

In order to spatially correlate the P3HT aggregation state to local photocurrent generation efficiency, functioning P3HT/PCBM solar cell devices of variable w/w loadings were first characterized I-V and EQE measurements to assess the average changes in electrical properties with changing composition and morphology. Generally, short circuit current densities (J_{SC}) and EQEs decrease considerably with increasing PCBM loadings suggesting that charge generation and charge transport efficiencies decrease due to the reduction in P3HT/PCBM interface area and crystalline P3HT regions necessary for splitting photogenerated excitons and extended charge migration pathways, respectively (see Figure 5.8). It is also important to stress that diminished photocurrent production arises from reduced amounts of P3HT chromophores in the device active layers that can be inferred from reductions in the overall P3HT absorption bands.

However, we focus specifically on the changes incurred in the P3HT component, in particular, its spatially varying aggregation properties determined from the RRPI approach.

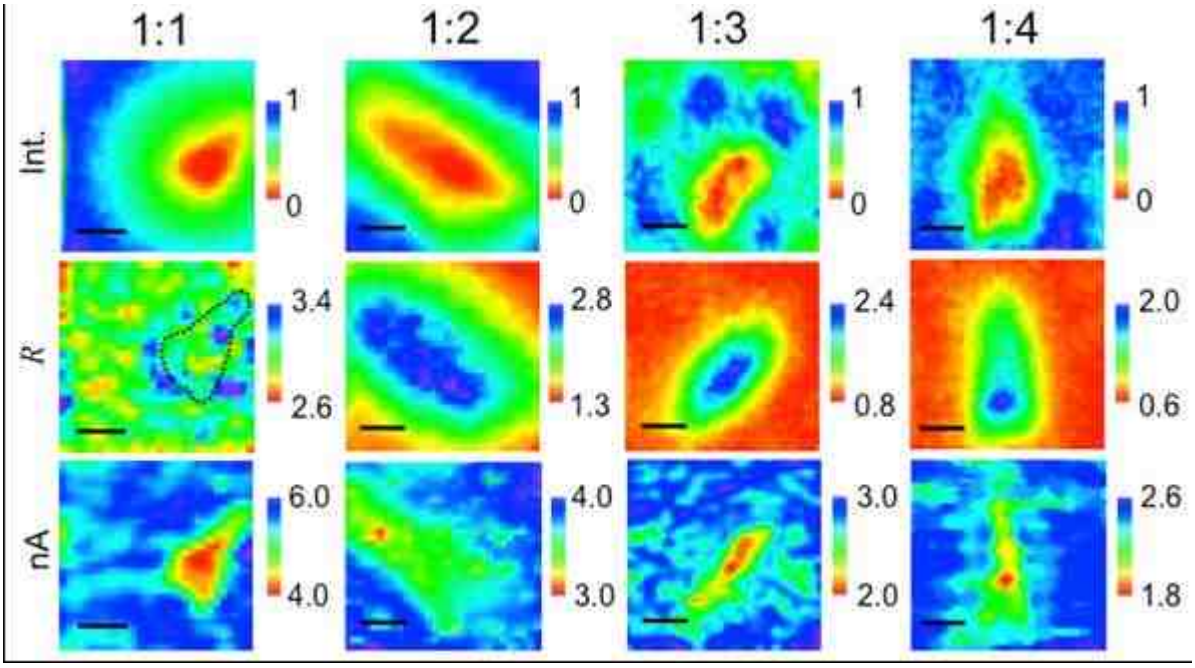

Figure 5.9. Raman intensity (top row), aggregation (R) (middle row), and photocurrent (bottom row) images of annealed P3HT/PCBM solar cell devices (scale bars = 3 μm). A sketch outline of the PCBM-rich region in the 1:1 w/w film is superimposed on the "R" image.

Figure 5.9 shows P3HT C=C mode total integrated intensity, "R" (aggregation state) images, and photocurrent images for P3HT/PCBM thin films of 1:1, 1:2, 1:3 and 1:4 w/w loadings. We emphasize regions of the films that possess both P3HT and

PCBM-rich areas (namely crystallites for the latter) and we observe similar morphological characteristics as seen in previous reports using c-AFM techniques.[69] In general, P3HT C=C total integrated Raman intensities show significant reductions in PCBM-rich regions which is confirmed by performing bright-field optical imaging in the same area (data not shown). "R" images reveal the spatial variation of the P3HT aggregation state due to local morphology fluctuations. Generally, the largest changes in R values tend to occur around PCBM crystallites for 1:1 loadings which is consistent with our previous findings.[158] Surprisingly, minority P3HT chains inside PCBM-rich regions for higher (>1:2) PCBM loadings show increased aggregation. This result is quite intriguing since P3HT aggregation should be entirely suppressed due to the small amounts of P3HT in these regions (based on corresponding Raman intensities) from nearly complete phase segregation. Smaller R values of P3HT-rich regions surrounding PCBM crystallites in films of >1:1 w/w loadings indicate that these chains are primarily unaggregated due to the increased amounts of PCBM that effectively inhibit aggregation. These aggregation maps are consistent with trends observed in absorption spectra but have the distinct advantage that the spatial locations of aggregated chains can be determined. Another possible explanation for the reversal in aggregated chain spatial distributions may be that minority P3HT molecules form a "skin" around the PCBM crystallites as seen in polyphenylenevinylene/fullerene thin films of 1:4 w/w ratios.[164] While we cannot completely rule out this possibility, we instead believe that P3HT chains become trapped in the PCBM crystallites which forces them to take on ordered but

collapsed or, self-aggregated, conformations to minimize interactions with surrounding fullerene molecules that is supported from previous AFM images of P3HT/PCBM blends that clearly show exposed PCBM crystallites surrounded by P3HT-rich regions.[69,142,165]

While it is known that crystalline, or aggregated, P3HT networks are necessary to promote good charge transport and ultimately device performance, very little is understood about how aggregated regions of different sizes and compositions contribute to photocurrent generation. We now attempt to address this issue by comparing R and photocurrent images for variable P3HT/PCBM loadings. Photocurrent images are shown in the bottom row for each loading in Fig. 5.9 and, similar to bulk device I-V curves, average photocurrent production decreases with increased PCBM loadings. Further examination of photocurrent images reveals that decreased production occurs from within regions corresponding to PCBM crystallites (i.e. low Raman intensity). However, small reductions of photocurrents are also found in regions of high P3HT aggregation in 1:1 P3HT/PCBM devices presumably due to complete phase separation of both components or possibly charge trapping by surrounding unaggregated regions.[158,166] This feature illustrates the sensitivity of local aggregation and composition that must be balanced for optimal performance but is usually difficult to resolve in conventional spectroscopy and scanned probe techniques. Since most aggregated P3HT chains for films with PCBM loadings of 1:2 and larger reside within PCBM crystallites, photocurrent decreases are most likely due to the lack of extended P3HT aggregate networks. Unfortunately, photocurrent signal-to-noise ratios of these devices decrease significantly with higher

PCBM loadings making a detailed quantitative comparison difficult and we are presently exploring new device architectures to maximize photocurrent collection efficiency. This effect is not only due to both reduced concentrations of P3HT and a greater amount of unaggregated chains, but also the spatial locations of aggregates.

The spatial mapping of the P3HT aggregation state to local photocurrent generation provides valuable insights into the intrinsic variation in polymer packing characteristics that change with PCBM content that augments current understanding borne out from previous ensemble device characterization studies of P3HT/PCBM devices with varying compositions.[43] The unexpected change in the location of aggregated P3HT chains and reduction of interchain exciton couplings in films of 1:2 loadings and higher requires further exploration. We now delve into the specific structural (i.e. chain conformational characteristics) factors that regulate the type of aggregation and the locations of aggregated regions as well as key electronic structure parameters previously determined from ensemble absorption spectra.

5.3.4 P3HT aggregation mode changes with increased PCBM content

Along with changes in the dominant P3HT C=C Raman lineshapes due to changes in the relative amounts of aggregated and unaggregated chains, other P3HT skeletal vibrational modes can provide additional insights into the changes of conformational attributes of P3HT chains observed in these films. For example, we previously noted that P3HT C-C mode Raman band frequencies and intensities also

increase with annealing treatments in films of 1:1 loadings that also coincides with regions greater aggregation amongst P3HT chains.[142] This effect was assigned as an increase in chain planarity which should, intuitively, be correlated to the P3HT aggregation state. From Figs. 5.3b,d, the average C-C mode intensities and frequencies decrease with increased PCBM loadings indicating diminished charge density in these bonds due to the more twisted character of thiophene rings corresponding to lower aggregation (i.e. smaller *R* values). However, these trends can be misleading since they only report the average over the entire film. On this note, it is more informative to construct maps of P3HT C-C frequencies (ω_{C-C}) and the C=C aggregated frequency component ($\omega_{C=C}^{agg.}$) (shown in Fig. 5.10) to uncover spatial correlations between chain planarity and aggregation.

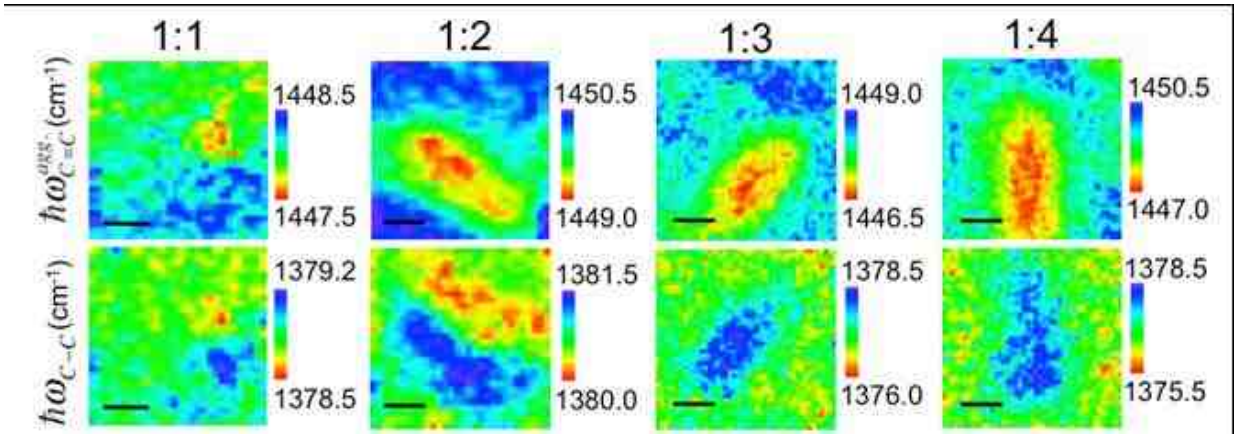

Figure 5.10. P3HT C=C aggregate component and C-C Raman frequency images for variable loading P3HT/PCBM thin film devices (scale bars = 3 μm).

Generally, values of $\hbar\omega^{agg}_{C=C}$ are lower in aggregated regions whereas $\hbar\omega_{C-C}$ show larger values in these same regions. The apparent blue-shifts of the latter also correspond to marked increases in the intensities of this mode. This effect is indicative of increased delocalization amongst chain segments due to enhanced chain planarity and is most distinct in films of >1:1 P3HT/PCBM loadings. Unfortunately, it is not possible to compare absolute frequencies due to minor fluctuations in instrument calibration between samples, however, the observed trends did not change. Another intriguing explanation for the observed increases in the C-C intensities and apparent blue-shifts is the tendency of P3HT chains to adopt a quinoid structure with increased aggregation. While this possibility requires further study, related Raman and absorption spectroscopic studies on both aromatic and quinoidal oligothiophenes reveal similar trends as presented here.[167 168] Furthermore, the quinoid form could be stabilized by aggregation interactions that

become more prevalent with thermal annealing suggesting a cooperative effect between the polymer aggregation state and accessible resonance forms. Additionally, the use of C-C frequencies and intensities as a measure of planarity is also supported from Raman spectra measured of as-cast P3HT/PCBM and regio-random P3HT films that show low C-C band intensities (signal-to-noise ratios <2) and red-shifted frequencies with respect to annealed films due to the highly twisted nature of the thiophene rings in these systems that do not permit aggregation. Based on the effects of chain planarity on aggregation, we now attempt to establish relationships between the above structural characteristics of aggregated P3HT chains to the exciton bandwidth parameter, W, describing the extent of intra- and intermolecular order.

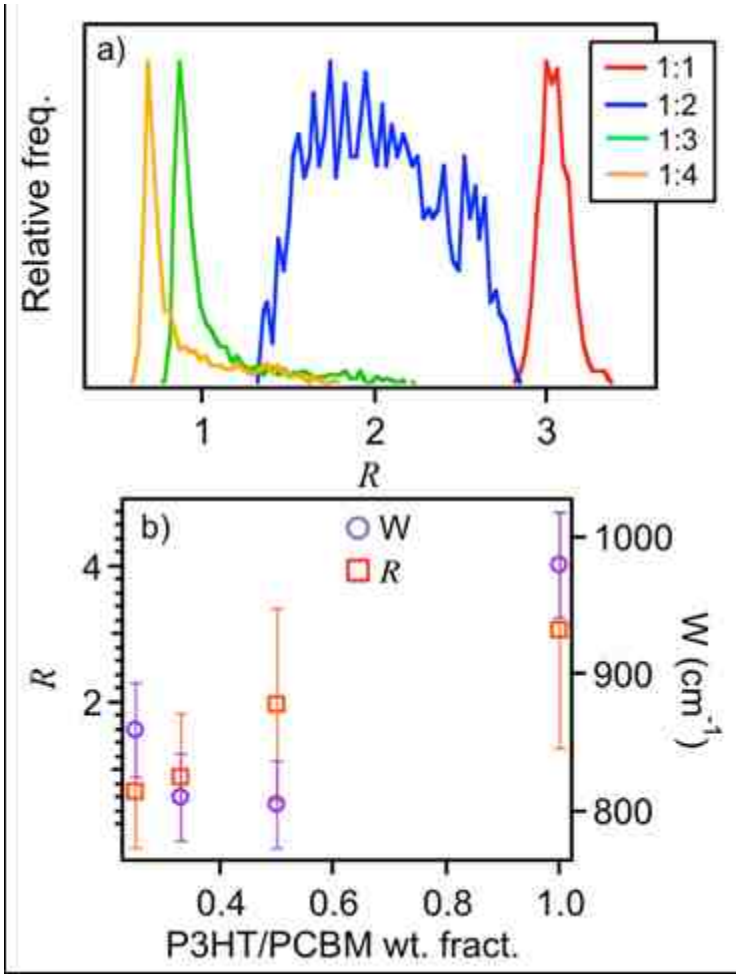

Figure 5.11. a) Histograms of the P3HT C=C "R" values shown in Fig. 5.9 for varying P3HT/PCBM content. b) Average P3HT aggregation (R) and exciton bandwidth (W) absorption spectra fit parameters as a function of P3HT/PCBM weight fraction.

For this comparison, it is helpful to re-cast R values into histograms to show how the distributions of aggregated P3HT chains change with variable loading. Figure 5.11a shows histograms of P3HT aggregation profiles generated from "R" images (Fig. 5.9, middle row) revealing changes in the distribution behaviors of aggregation as PCBM

content changes. As the PCBM weight fraction is increased, distributions first become broader (i.e. 1:2) then transition to a relatively narrow maximum at small average R values (<1) with a long tail toward higher R values (i.e. >1:2 loadings). We assign aggregated chains in 1:1 loadings as interchain aggregates that gradually decrease due to interference from PCBM molecules at higher loadings. Since aggregated chains are known to facilitate charge transport, these histograms reveal changes in the distributions of the types of aggregated species not readily apparent from R images. This aspect is especially important since aggregated P3HT chains are widely believed to be current-carrying species in P3HT/PCBM solar cells and a shift of aggregation type could disrupt charge transport leading to increased recombination. Because the exciton bandwidth parameter, W, is dependent upon chain order, it is useful to establish correlations between interchain coupling and the P3HT aggregation state. Fig. 5.11b shows plots of these parameters that decrease with increasing PCBM content that is also consistent with a shift from inter- to intra-chain aggregation interactions. As previously noted, a decrease in W suggests an increase in chain planarity and conjugation lengths for aggregated P3HT chains that result in lower interchain electronic coupling. This trend further explains the effect of self-aggregation of P3HT chains possibly into rod-like conformations that lead to significant reductions in overall photocurrent generation due to the loss of extended interchain aggregated networks that was supported by comparisons of the C-C and the C=C aggregated component frequency images in Fig. 5.10.

5.4 Conclusions

We have shown that increasing PCBM loadings result in a decrease of P3HT interchain aggregation interactions in P3HT/PCBM thin films that cause reductions in solar cell device performance. These morphology- and composition-dependent changes are manifested as increases in the 0-0/0-1 absorption vibronic peak ratios in the aggregate portion of the blend thin film ensemble absorption spectrum in addition to decreases in P3HT C=C Raman aggregated vs. unaggregated component averaged intensity ratios. By constructing spatial maps of the P3HT aggregation state and local photocurrent generation, we are able to resolve the role of polymer aggregation in photocurrent production. Surprisingly, the majority of aggregated P3HT chains for films with PCBM loadings >1:1 were found to be localized within PCBM-rich regions which was not apparent from absorption spectra or device EQE studies. Fit spectra generated from the weakly coupled H-aggregate model also showed significant decreases in the exciton bandwidth parameter indicating increased intra-chain order. P3HT C-C and aggregated C=C mode frequency images supported this result and uncovered important correlations between the polymer aggregation state and chain planarity that, together with aggregation image profiles, are consistent with a shift from predominantly inter- to intra-chain aggregation. Histograms of P3HT aggregation state (R values) distributions as well as were also used to show the transition of the type of aggregated P3HT chains from a primarily interchain type to intra-chain (self) aggregated chains within PCBM-rich areas. Moreover, the spatial location of aggregates revealed from these RRPI studies also sheds

light on previously misunderstood relationships. We thus conclude that optimal device performance is achieved when P3HT chain aggregation is largely of interchain type which is only realized in films of 1:1 w/w ratios. Although previous trial and error studies of varying film composition and processing conditions have alluded to the importance of such aggregation effects, this work now reveals the molecular structure factors that govern not only aggregate concentration but also its spatial location in the film. Overall, the combined RRPI and weakly coupled H-aggregate model fits of absorption spectra reveal new insights into the structural attributes and roles of aggregated chains on material performance that are not available from conventional device characterization techniques.

Chapter 6

Intensity Modulated Photocurrent Imaging of Polythiophene/Fullerene Solar Cells

(This chapter is based on a manuscript in preparation.)

6.1 Introduction

Conjugated polymer solar cells are among some of the most promising candidates for viable alternative energy resources. Despite historically low power conversion efficiencies (<10%), significant improvements have been made over the last five years owing largely to a better understanding of material structure-function relationships.[110,153,169-171] Of all processes involved in the generation of photocurrent in polymer solar cells, charge transport is perhaps the most susceptible to variations in material packing, morphology and defects.[172-176] More importantly, the performance characteristics of polymeric solar cells are dominated by wasteful charge recombination processes that are consequence of low dielectric constants and morphological heterogeneity found in these materials.[177-181] These processes are also sensitive to material processing conditions, such as solvent and annealing treatments, that lead to variations charge transport properties (typically measured as mobilities, $cm^2/V/s$) often by several orders of magnitude.[155,182,183] The fact that electron acceptors must be added

to polymers to separate neutral photo excitations (excitons) into free carriers also complicates the physical pictures of charge transport.

Clearly, understanding morphology-dependent charge transport in polymer/fullerene solar cells is of central importance for improving overall efficiencies. Typically, unipolar charge mobilities of either the polymer or fullerene components are measured that provide insights into the effect of morphology on bulk charge transport properties.[26,184-186] Space-charge limited current (SCLC) measurements are perhaps the most commonly used technique for measuring mobilities that are obtained from device current-voltage (I-V) measurements in the dark.[140,187,188] Here, mobilities of charge carriers of either sign (i.e., holes and electrons) can be extracted from I-V curves via the Mott-Gurney law. However, SCLC measurements are performed in the dark and under device operating conditions not encountered in typical solar cells. Alternatively, time-of-flight (ToF) techniques can also be used to measure charge mobilities.[189-191] In this approach, a short laser pulse generates a localized distribution of carriers (i.e., near the transparent electrode) that are swept to the opposite electrode by an applied bias. By measuring carrier transit times from inflections in the time-dependent photocurrent, it is possible to extract mobility information under the assumption that diffusion of carriers is small compared to drift velocities. Charge extraction by linearly increasing voltage (CELIV) allows for the study of equilibrium carriers without photoexcitation.[192] However, ToF and CELIV must be performed in non-ideal device structures, namely thick (>1 μm) films due to the need to sweep charges out of the organic layer. In

addition, charge blocking layers must often be employed to ensure that carrier mobilities of one sign are measured. Clearly, a better physical approach is required to generate an accurate picture of morphology-dependent charge transport in disordered polymeric solar cell materials. Moreover, it is desirable to study bulk and surface charge transport processes separately which is difficult using the above techniques.

To this end, intensity modulated photocurrent spectroscopy (IMPS) has recently emerged as an effective tool for studying charge transport, recombination and trapping in polymeric solar cells and has seen extensive use in inorganic semiconductors.[99,103,104,193] IMPS is a frequency domain technique that uses a small AC modulation over a large DC background to study charge carrier processes in the range of 10^{-3} up to 10 MHz. The small modulation depth (ca. 10-50%) ensures linear response and low excitation powers can be used which circumvents difficulties associated with pulsed laser excitation used in ToF studies. Frequency-dependent photocurrents can be detected using lock-in techniques which offer high sensitivity down to the picoampere level. Both the real (in-phase) and imaginary (quadrature) components of the photocurrent are obtained that reveal important insights into the mechanisms of charge transport and relaxation processes. More importantly, IMPS can be performed without application of an external bias (i.e., short circuit conditions, 0V) and on realistic devices unlike in ToF and CELIV techniques. Lastly, both bulk and surface transport and recombination processes can be investigated separately due to their different timescales.

Herein, we introduce a new frequency-dependent photocurrent imaging technique that can spatially map the morphology-dependent variation of charge transport properties in disordered polymeric solar cells. Model solar cell devices are fabricated using poly-3-hexylthiophene (P3HT) blended with [6, 6]-phenyl-C_{61}-butyric acid methyl ester (PCBM) in a 1:1 w/w ratio as the active organic layer in the device. The P3HT/PCBM system represents the benchmark in polymeric solar cells and device power conversion efficiencies of over 6% are routinely achieved.[194] Extensive spectroscopic, scanned probe, X-ray and electron microscopy studies of this system have demonstrated that increased order (crystallinity) in the P3HT component is responsible for large improvements in charge transport efficiency resulting in relatively high power conversion efficiencies.[69,75,115,158] It has also been proposed by several groups that the efficiency of these devices can be further improved by suppressing charge recombination. However, the specific mechanisms of charge recombination are not well understood.

Recent IMPS studies of P3HT/PCBM solar cells have shown that non-geminate carrier recombination dominates the performance attributes of these devices.[104] We now extend the IMPS technique to spatially map the morphology-dependent photocurrent generation in P3HT/PCBM solar cells which has several advantages over conventional IMPS, namely:

i) Photocurrent is generated from a region illuminated by a diffraction-limited laser spot allowing the study of regions with varying phase purity.

ii) Imaging of the IMPS response can be used to sort out contact and bulk transport processes.

iii) Transport mechanisms can be tested and new spatial correlations between local structure and material function can be established.

Furthermore, Raman imaging experiments can also be performed over the same scan area to understand morphology-dependent packing (aggregation) characteristics of P3HT chains which provides a basis for new structure-function correlations in this system.

6.2 Experimental section

P3HT/PCBM model solar cells were fabricated using coverslips coated with indium-tin-oxide (ITO, Metavac) with a sheet resistance of ~15 Ω/□. P3HT (Rieke Metals) and PCBM (Aldrich) were dissolved overnight in chlorobenzene solutions at a concentration of 10 mg/mL. A hole transport layer, PEDOT: PSS (Baytron) was first deposited on rigorously cleaned ITO and baked at 110 ^{o}C for 30 min, then spin-coat the P3HT/PCBM film (1:1 w/w) onto ITO/PEDOT substrate at 600 rpm for 180 sec. in a nitrogen glove box. The films were placed on a hotplate to anneal at 130 ^{o}C from 20 min. Aluminum contacts (~100 nm) were next deposited in a thermal evaporator at a base pressure of ~10^{-5} mbar and leads were attached to devices with silver paint (Dynaloy). Devices were then placed inside a nitrogen flow cell for IMPS measurements and current-voltage (I-V) measurements. I-V curves were generated on devices using a source-measure unit (Keithley 2400 or 2635) while illuminated by a solar simulator

(AM1.5, Spectra Physics). Typical power conversion efficiencies for devices studied herein were ~0.5% - 1%. Variability of device performance was checked by I-V, Raman spectroscopy and IMPS.

6.3 Results and discussion

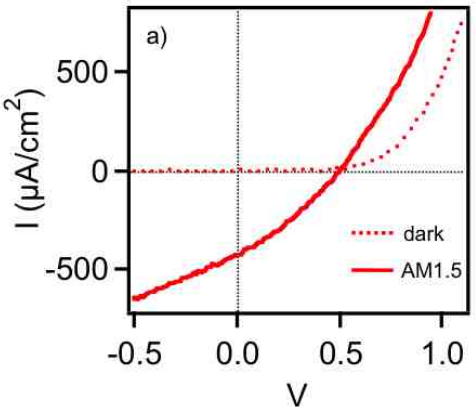

Figure 6.1. Current-voltage (I-V) curves of annealed P3HT-PCBM devices measured in the dark and under AM1.5 illumination.

Figure 6.1 shows standard I-V curves for a P3HT/PCBM device measured in the dark and under AM1.5 illumination. I-V curves for the former show diode-like behavior with a turn-on voltage of ca. 0.6V which is similar to previous reports in the literature. Upon illumination, devices show photocurrent generation with short circuit current densities of ~500 $\mu A/cm^2$ – 1 mA/cm^2. Fill factors were ~30% indicating significant losses probably due to recombination and poor carrier extraction efficiency.

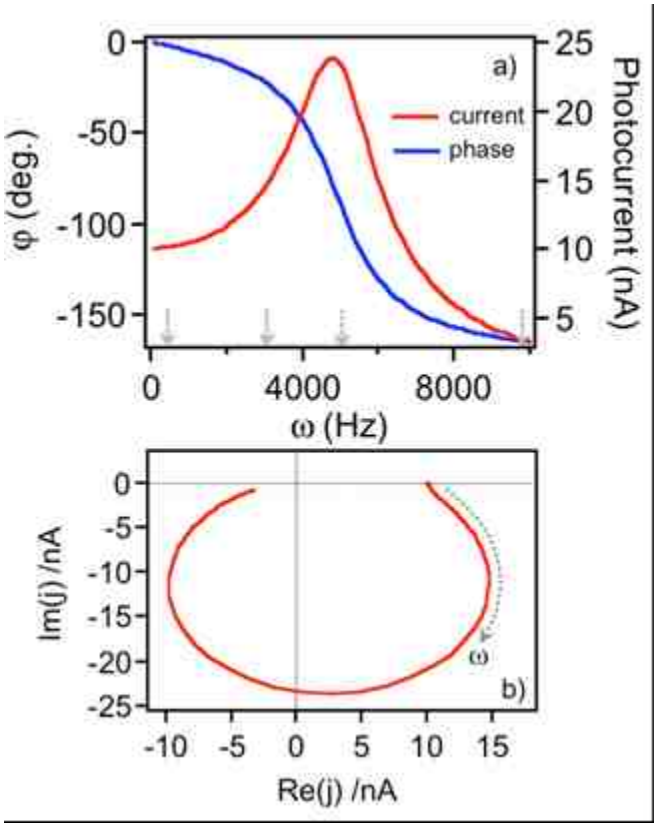

Figure 6.2. IMPS spectra of P3HT: PCBM solar cells. a) is photocurrent and phase shift spectra. b) is the complex plot of imaginary and real component of photocurrent.

IMPS spectra of a representative device are shown in Figure 6.2 with the photocurrent magnitude and phase shift labeled. These spectra were generated under wide field illumination that samples the entire device active area (~25 mm^2). As the AC modulation frequency is increased the photocurrent shows an increase to a maximum value at ~4 KHz (ω_{max}). The phase shift concomitantly decreases from ~0 degrees to -90 degrees. At higher frequencies (>4 KHz) the photocurrent decreases in addition to a further decrease of the phase shift to -170 degrees. IMPS data can offer valuable insights

into carrier loss mechanisms that are not apparent in steady state I-V measurements. For example, charge recombination processes involving deeply trapped charge are known to occur on timescales of microseconds to milliseconds which can be directly interrogated by IMPS. We speculate that the increase in photocurrent with increasing modulation frequency up to ω_{max} is the result of carrier recombination from traps which are likely chemical defects are interface states at the electrode contacts. At higher frequencies, bulk transport processes dominate and there is presently no developed theory to describe this regime. Byers et al. recently reported IMPS studies P3HT/PCBM devices and analyzed the IMPS complex plots to deduce carrier recombination mechanisms.[104] Figure 6.2b shows the complex plots generated from P3HT/PCBM devices described herein which show qualitative similarities to those reported from Byers et al. Our devices show a prominent component in the 4th quadrant that move into the 3rd quadrant at higher frequencies. Surprisingly, very little activity was observed in the 1st quadrant (unlike that of Byers et al.) which was proposed to be sensitive to recombination processes. The value of the real component at the imaginary intercept also provides a measure of the amount of photocurrent generation possible in the absence of recombination. From Fig. 6.2b we find a value of ~10 nA that, despite appearing rather small, is a consequence of the fact that these measurements are performed using nearly monochromatic light at power densities much smaller than that of the solar spectrum (AM1.5). We speculate that this discrepancy is the result of choice of processing conditions since the IMPS response is otherwise similar. Furthermore, the change of the photocurrent phase shift indicates

that photocurrent leads the light intensity which is representative of charging of the interface followed by non-geminate carrier recombination. We consider these effects further in the following by extending the IMPS approach to spatially map the morphology-dependent recombination processes of P3HT/PCBM solar cells.

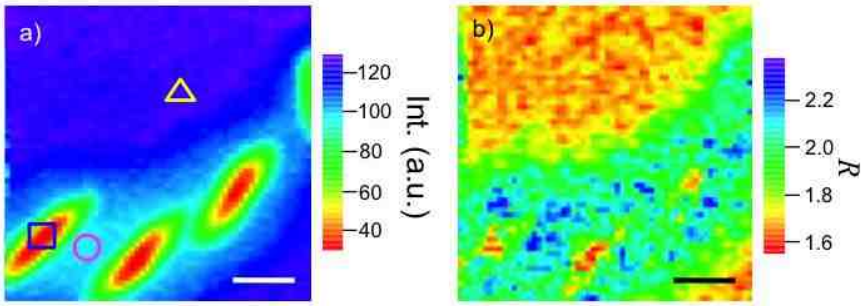

Figure 6.3. Raman image of the P3HT: PCBM annealed device. a) is normalized Raman intensity image of C=C band. b) is the *R* image . Square, circle and triangle represent incide PCBM –rich region (lower aggregation of P3HT), between crystals (higher aggregationof P3HT) and off crystal region (moderate aggregation of P3HT). The scale bar is 2 μm.

Because of the complicated phase segregated nature of polymer/fullerene thin films, it is first necessary to understand the spatial distributions and phase purity of the materials. Resonance Raman spectroscopic imaging is an excellent tool for unraveling the local composition of polymer/fullerene blends that involves the selective excitation of one component (i.e., P3HT).[142] Figure 6.3 shows Raman intensity and "R" images of

P3HT/PCBM solar cells excited with 488 nm light. We track morphology-dependent variations in the totally symmetric C=C stretching mode of P3HT (~1450 cm^{-1}) as well as decompose this band into contributions from aggregated (I_{agg}) and unaggregated (I_{un}) using a procedure described previously. By taking the ratio of I_{agg}/ I_{un} (R) it is possible to spatially map the packing state of the P3HT component. Furthermore, the high sensitivity of this figure of merit to local composition provides a means to characterize the local phase purity of the film. Because PCBM Raman scattering cross sections are relatively poor at the excitation wavelengths used, lower Raman intensities indicate the presence of PCBM-rich regions which appear as oblong crystallites in Fig. 6.3a. R images reveal that the packing characteristics of P3HT vary significantly throughout the film which can be correlated to local charge transport characteristics using IMPS imaging.

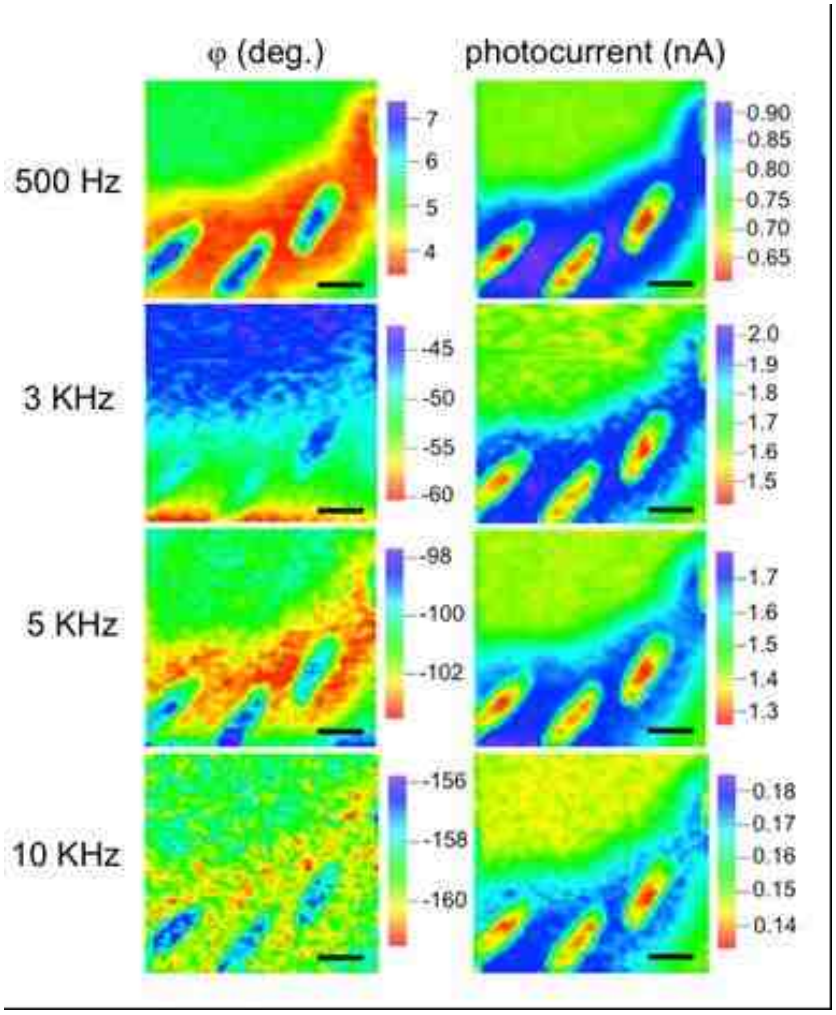

Figure 6.4. IMPS images of P3HT: PCBM annealed device at different modulation frequency. Both phase shift and photocurrent images are presented. Scale bar is 2 μm.

Figure 6.4 shows a series of IMPS images collected over the same scan area used in Raman imaging measurements with the modulation frequency held at a constant value as indicated in Fig. 6.2a. The chosen frequencies represent samplings of the overall IMPS response shown in Fig. 6.2a and represent different regimes of charge transport

processes in P3HT/PCBM solar cells. Comparison of phase shift and photocurrent images at low frequencies (500 Hz) shows that regions of poor photocurrent generation (i.e., PCBM-rich) have more positive phase shifts that suggests increased carrier recombination. This is supported by the fact that carrier separation occurs predominantly at P3HT/PCBM interfaces and subsequent trapping and recombination processes should be enhanced in these regions. However, recent studies have shown that while PCBM is not miscible in ordered (aggregated) P3HT chains, unaggregated regions do in fact contain significant amounts of PCBM which is necessary for sufficient charge generation. This feature suggests that increased phase separation and, hence phase purity can be detrimental for overall device performance. Increasing the modulation frequency close to ωmax (3 KHz) shows that the average photocurrent production increases similar to observations in ensemble IMPS measurements (Fig. 6.2a) as well as larger phase shifts. Modulation frequencies slightly beyond ωmax (5 KHz) also show similar behavior although phase contrast for both are diminished. At high frequencies (10 KHz), photocurrent production decreases substantially and phase contrast is poor. In this regime, bulk effects begin to dominate and distinctions between transport properties for specific regions is lost. We now perform IMPS at specific points in the device that are indicated by the symbols in Fig. 6.3a to further understand the dependence of the IMPS response for local blend composition.

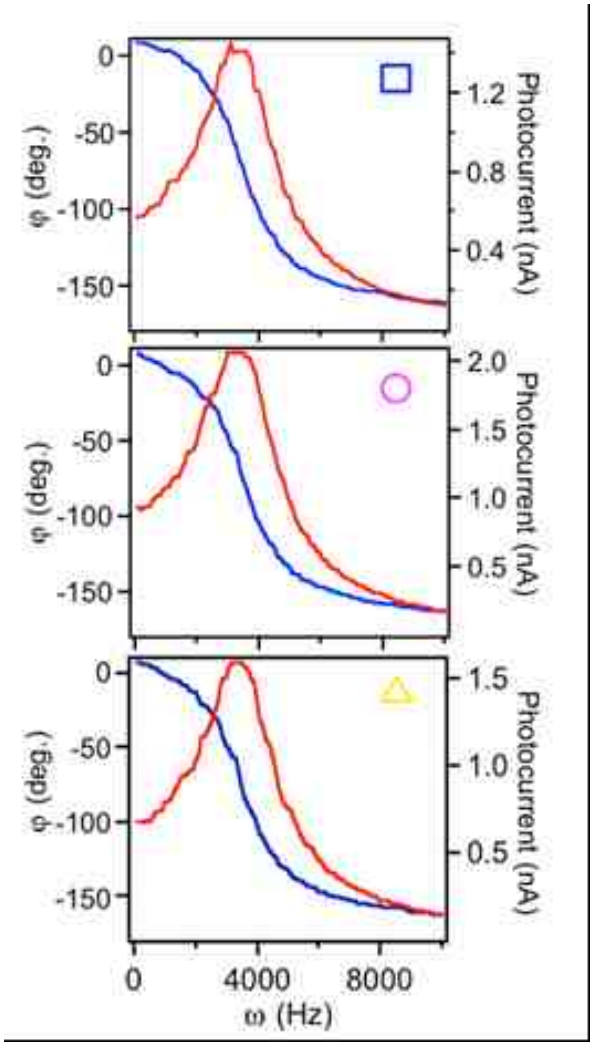

Figure 6.5. IMPS spectra generated from three distinct regions of the annealed P3HT: PCBM solar cell: P3HT-rich (triangle); PCBM- rich (square); P3HT/PCBM (circle).

Figure 5 shows IMPS spectra generated for three distinct regions: P3HT-rich (triangle); PCBM- rich (square); P3HT/PCBM (circle). Despite that IMPS images show good contrast for both phase shift and photocurrent, IMPS spectra at these distinct regions appear largely invariant. A likely reason for this effect is that a diffraction-

limited spot of the sample is illuminated but, current is collected over the entire device area. We believe that the IMPS response is dominated by the bulk contact.

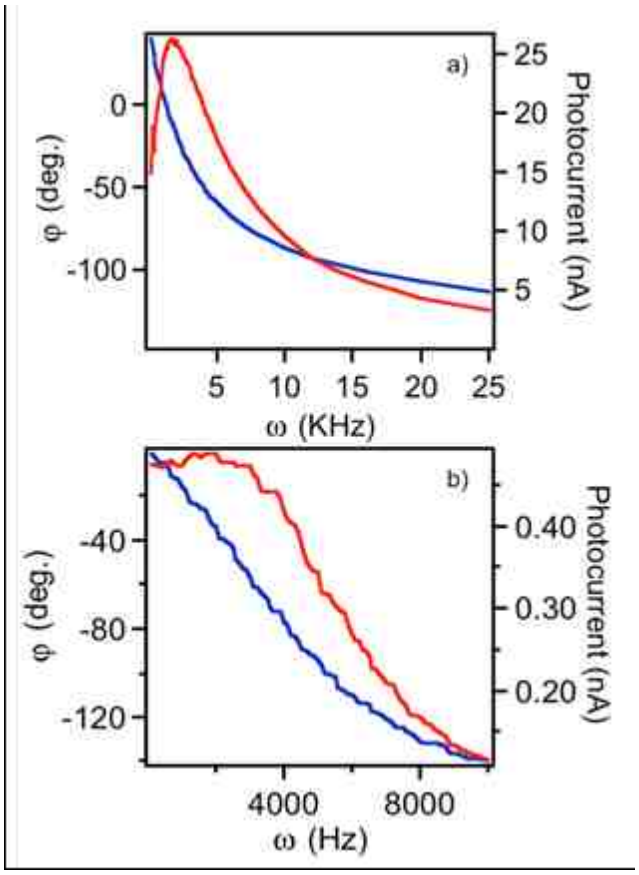

Figure 6.6. a) IMPS of thick devices (~1 μm); b) high excitation intensity on the IMPS response of P3HT: PCBM devices.

It is also informative to consider the dependence of the IMPS response on excitation power as well as material thickness as sources for contrast in Fig. 6.4. Fig. 6.6a shows IMPS spectra measured from a P3HT/PCBM device with a thickness of ~1 μm that exhibit pronounced red-shift of the photocurrent maximum and slower falloff at

higher modulation frequencies. These characteristics likely reflect the limited diffusion range of photogenerated charges in polymers. Fig. 6.6b shows the effect of high excitation intensity on the IMPS response. Namely, an increase of broadening is observed which may be the result of space charge effects.

6.4 Conclusion

Intensity modulated photocurrent spectroscopy (IMPS) and imaging is introduced to study the dynamics of traps, charge transport and recombination processes. Different aggregation regions of P3HT based on *R* values annealed P3HT: PCBM (1:1) solar cells were explored. Maps of the photocurrent and phase shift were recorded at several modulation frequencies spanning 100Hz up to 10 KHz. It was found that recombination from trapped charge dominates the IMPS profiles. Temperature- and color-dependent IMPS are now being performed to better understand charge transport mechanisms.

Chapter 7

Future work

7.1 Future work

Overall, the combined RRPI and weakly coupled H-aggregate model fits of absorption spectra reveal new insights into the structural attributes and roles of aggregated chains on material performance that are not available from conventional device characterization techniques.

7.1.1 Fluorescence mapping of P3HT:PCBM films to determine exciton bandwith

Morphology-dependent relative aggregation concentration (R values) of P3HT has been identified from resonant Raman imaging approach. However, the free exciton bandwidth (W) variation, which relates to average conjugation length and interchain orders, cannot be obtained directly from Raman spectra. The bulk estimate of *W* can be extracted from absorption spectrum of P3HT film using relative intensity of 0-0 and 0-1 ratio described by Spano.[92] To unravel the local morphology dependent *W,* photoluminescence spectra (PL) spectroscopy can be employed to do mapping.

The emission spectrum of P3HT can be collected using the microscope system described previously with a simple change in instrument conditions. For example, the spectral range can be increased by changing the grating to one of lower dispersion. Fluorescence emission spectra can then be collected in a point-by-point fashion and fitted using the weakly H aggregate model to extract morphology-dependent exciton couplings. Importantly, the setup described previously, allows the same scan used in Raman photocurrent imaging to be measured. Fitted *W* values can then be plotted to further understand the established correlations of P3HT aggregation and photocurrent generation. However, the challenge for this measurement is that PCBM molecules quench P3HT emission effectively, so to get the P3HT emission, the excitation power has be higher than in pristine P3HT films. Moreover, PCBM emission overlaps with P3HT emission spectra which may require lower PCBM loadings than that used for typical solar cells (1:1).

7.1.2 Pressure-dependent spectroscopy P3HT to simulate annealing

It was suggested that PCBM molecules perturb P3HT aggregation but electronic interactions are minimal. If the diffusion of PCBM forces to the aggregates formation, the other external physical force should have the similar effect on P3HT aggregation formation from disordered regions. It was reported in 1993 that the pressure applied on P3HT up to 80 kbar causes fluorescence intensity to decrease and strong red-shifts result from increased packing. [162] However, studies involving PCBM blends have not been

explored. Applied pressure will therefore be an excellent tool for understanding reversible changes in material packing and morphology that are not apparent from simple annealing treatments.

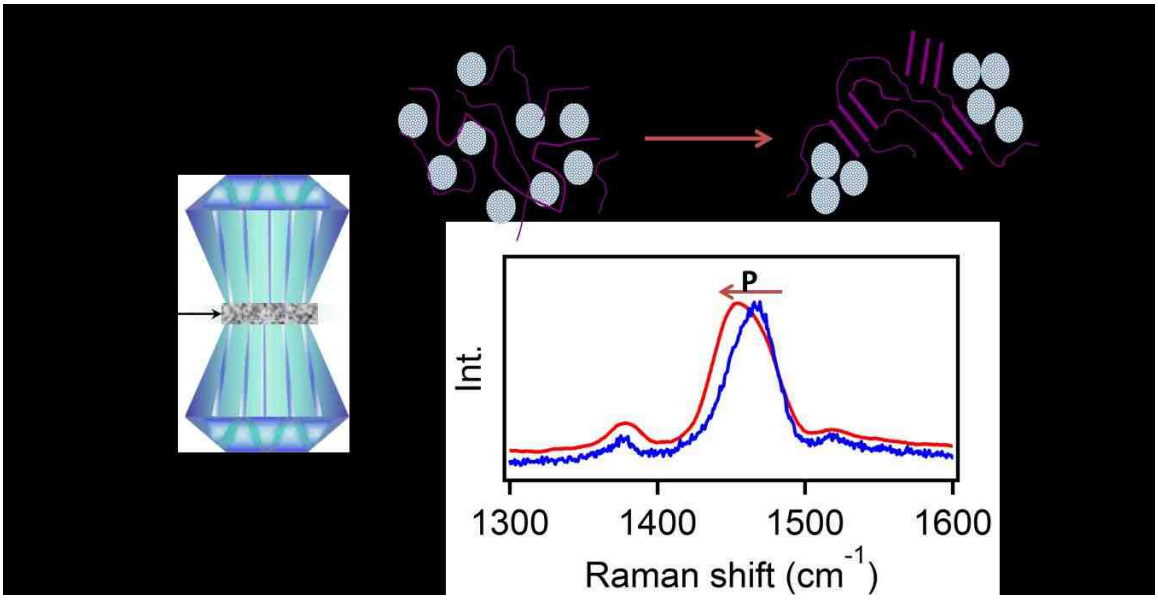

Figure 7.1. Schematic illustration of a pressure-dependent experiment and expected structure change of P3HT: PCBM blend with pressure. Pressure is proposed to induce similar aggregation as annealing.

The experimental setup and expected outcome are shown in Figure 7.1. First, a small amount of the solution of P3HT: PCBM is placed onto a diamond cell and dried to form a film. Then, pressure is applied by the diamond cell which perturbs packing interactions. Meanwhile, Raman and emission spectra can be collected with pressure

which should reveal important miscibility changes and packing. Furthermore, the diamond anvil cell allows for variable temperature studies which can be used to construct phase diagrams for solar cell composites.

Overall, the work presented herein provides new and important insights into polymer aggregation and film morphology effects that can aid in the rational design and improvement of solar cell composites. It is expected that the results will help materials scientists to tailor materials with optimal packing characteristics to improve device performance.

Appendices

Appendix A: Labview program for Raman photocurrent and phase shift measurement

This program is written in Labview to communicate with the scanning stage and synchronize the photocurrent/phase shift and Raman spectral data collection. The function of this code includes:

1) Auto scan with certain range. The maximum range is 200 μm, determined by the stage.
2) Sit onto specific scanned point.
3) Plot single molecule spectroscopy image with an APD (not used in Raman imaging).
4) Synchronize stage movement, photocurrent measurement and Raman spectrum collection.
5) Auto block and unblock laser beam via controlling an optical shutter.
6) Collect Photocurrent, phase shift, in phase and out of phase photocurrent component (used for IMPS measurement) with the lock-in amplifier.

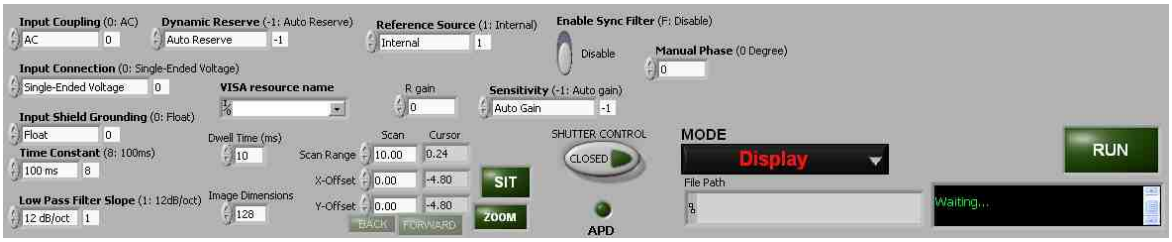

Figure A1. Part of the front panel of Raman and photocurrent/phase shift imaging program to show the input variables

The front panel is shown as Figure A1.1. In this program, we can set all related parameters for Lock-in preamplifier if photocurrent is needed:

1) VISA resonance name. Current address is GPIB0:10, which can be changed from 0-26.
2) Input coupling. Typically it is set as AC.
3) Dynamic Reserve. It is preferably set as low noise to get better signal to noise ratio.
4) Reference source. This should be set as external, which is referenced to either the function generator TTL output or chopper frequency output.
5) Enable filter is switched on if the reference frequency is lower than 200 Hz.
6) Manual phase is set to be 0 which means the reference wave phase is set 0, so that the phase shift is recorded relative to 0. If this set as auto, then phase shift values are always close to 0.
7) Sensitivity, which is dependent on the photocurrent range.

8) Input connection is set as Single Edge voltage if one current-to-voltage amplifier is used (if the phase shift is not needed) or current input (1Mohm Current Gain or 100 Mohm Current Gain).
9) Time constant is normally set as 100 ms, but it can vary if very low frequency (mHz) is used.
10) Low pass filter slope is set as 12 db/oct.

If only Raman imaging data is collected, just leave lock-in address as blank, the program will skip the Lock-in loop to do stage scan only with synchronization function with Raman spectrum collection. The scanning parameters include:

1) Dwell time (ms). It means how long the piezo stage will stay for one position. This time is same as the Raman spectrum accusation time. Typically, it is less than 1 sec (100ms).
2) Scan range and offsets (μm). It determines the scan range. The max value is 200 μm for the stage in our lab. X-and Y-offset number will shift the scan area correspondingly without physically moving the sample.
3) Gain. It is a factor to times the photocurrent measurement to have the computer record data correctly, for example, if the current is 1 nA, without the gain, which means Gain is 1, the recorded value will be 0, since lock-in output is 0.0000001 A which is considered as 0 by the computer, with one 10^9 Gain, the recorded value is 1.

4) Image Dimensions. It is the resolution for each line scan, overall positions for the whole scan range is square of this value. Generally, the scan step should be greater than the optical resolution limit. For example, we use 488 laser resolution can be estimated 250 nm even with an oil objective (N.A.=1.49) due to possible imperfection of beam quality , if we choose 10 μm, select 30, which means each step is about 300 nm, this is good enough to get the scan image, or put 40 as maximum. This value determines the spectroscopic and photocurrent image resolution.

Appendix B: Labview for Intensity modulation photocurrent spectroscopy (IMPS) and imaging

The IMPS program is written for performing an IMPS measurement without imaging capability. Combined with the imaging program, shown in Appendix A, after the scan, find interested regions such as crystalline region and off crystal regions and let laser spot sit onto the specific point. Run IMPS program, it will do the IMPS measurement for that point to record frequency, photocurrent, phase shift, real and imaginary component of photocurrent and display them as plots. In principle, it controls three instruments:

1) A lock-in amplifier to collect photocurrent, phase shift, X-component (imaginary photocurrent, as people call), Y-component (real photocurrent) at different modulation frequencies.
2) A function generator to offer the reference frequency for lock-in and modulate the Phoxx 488 laser source with one large DC illumination and small (normally 10%) modulation.
3) An optical shutter, which is open during the data collection and closed to block light after the run to protect samples.

Herein, the input parameters from the front panel, as shown in Figure A2, include:

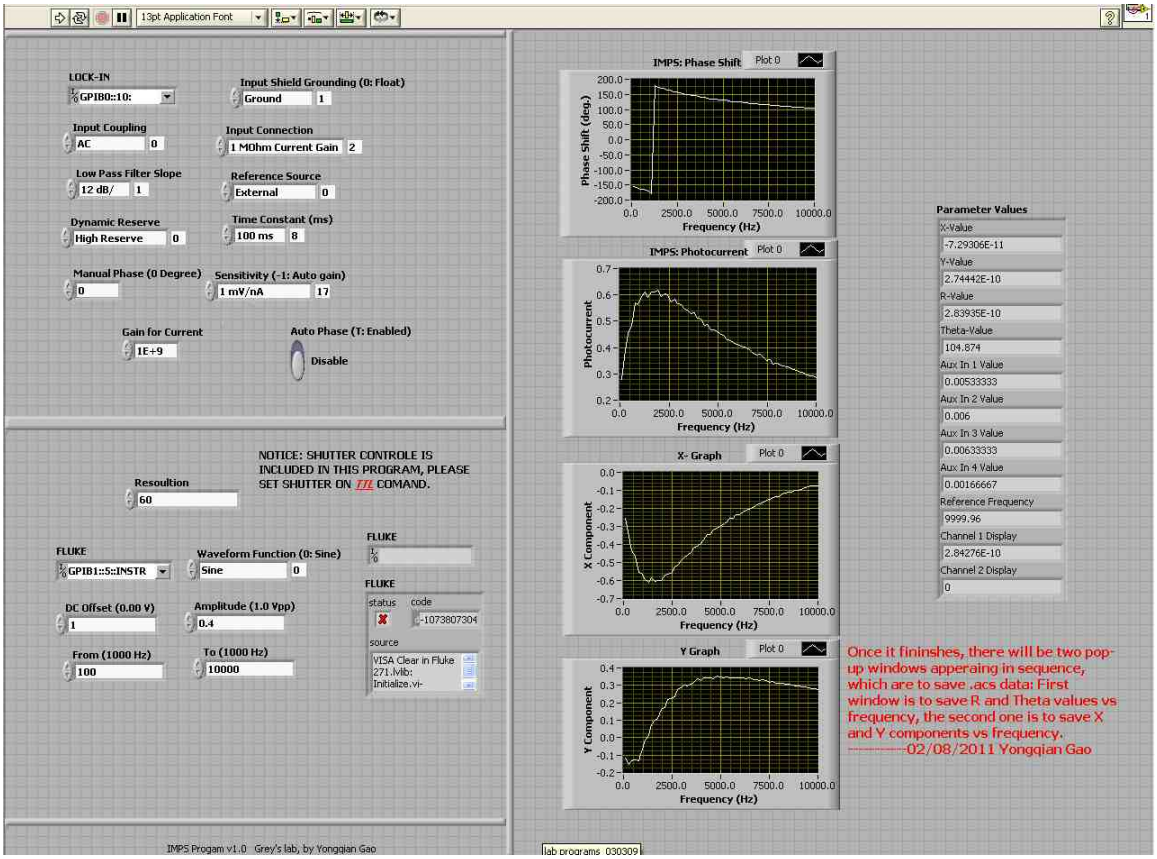

Figure A2. Front panel of IMPS program: Left top is the settings for Lock-in, which is shown in Appendix A, and left bottom is for function generator settings; the right is the indicator to show the spectra after it finishes.

The Lock-in settings are put one the left top part, the setting are pretty much the same as shown in Appendix A. The two differences are: One, since the introduction of current amplifier, there will be extra unknown phase shift contamination, only current input gain is used; two, Sync filter is set on or off automatically inside the program due to the sweeping frequency. **Driver for function generator was written for Fluke 271**

model only based on the driver template inside Labview, no guarantee it works for other models, however, if the commands are replaced by the other model supported ones, this driver should work with some modification. The fluke 271 is set as: address is GPIB1::5::INSTR, wave function is sine, DC offset is normally set as 7 V **(notice the front panel of Fluke 271 to see if the DC offset is autoscale to 701mV, because this voltage will feed to Phoxx488 laser source which can only accept 1 V as max input.)** Amplitude is to set V_{hiz} as 0.07 V, which is 10% of DC offset. From and To are to set the sweeping frequency range, since the lock-in model, SR 830 can only work in the range of 1 mHz to 102 kHz, be sure not exceeding the range. Normally we set the sweeping range from 100 Hz to 10 kHz. Resolution is the point for the sweeping, if we set it as 100 from 100 Hz to 10 kHz, each step is 100 Hz. After all parameters are set, click the arrow sign to run the program. Once it finishes, there will be two pop-up windows showing up in sequence, the first one is to save photocurrent/phase shift and frequency, second is to save X/Y component and frequency.

Appendix C: The labview for Galvo microscopic system

The scheme of 2 axis galvo scanning is illustrated in Figure A3: the laser beam is steered by two motorized x and y mirrors with limited travel range to scan certain area. To make one labview code for this purpose, the major control is to offer the two motors accurate voltage so that the travel distance, *l*, is determined with known *d*.

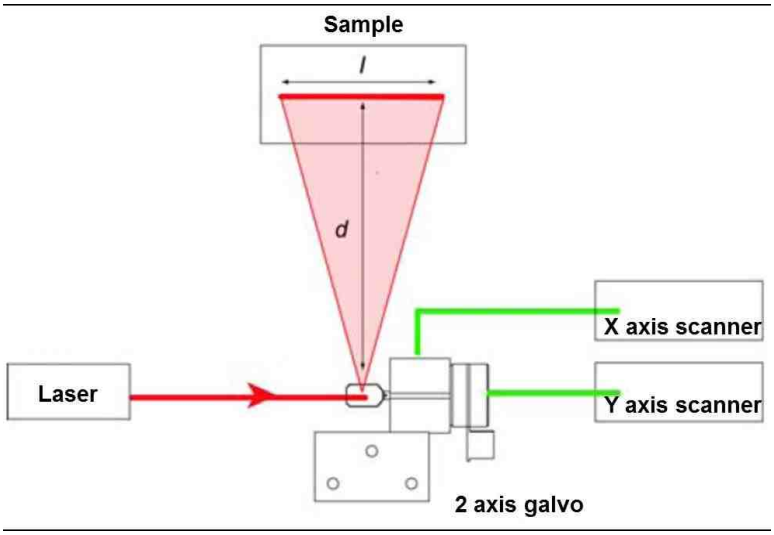

Figure A3. Scheme of 2 axis galvo scanning system**.** A laser beam is steered by x and y axis mirror to scan one square region, the scan distance *l* is determined by the distance of d. Adapted from thorlabs.com with modification.

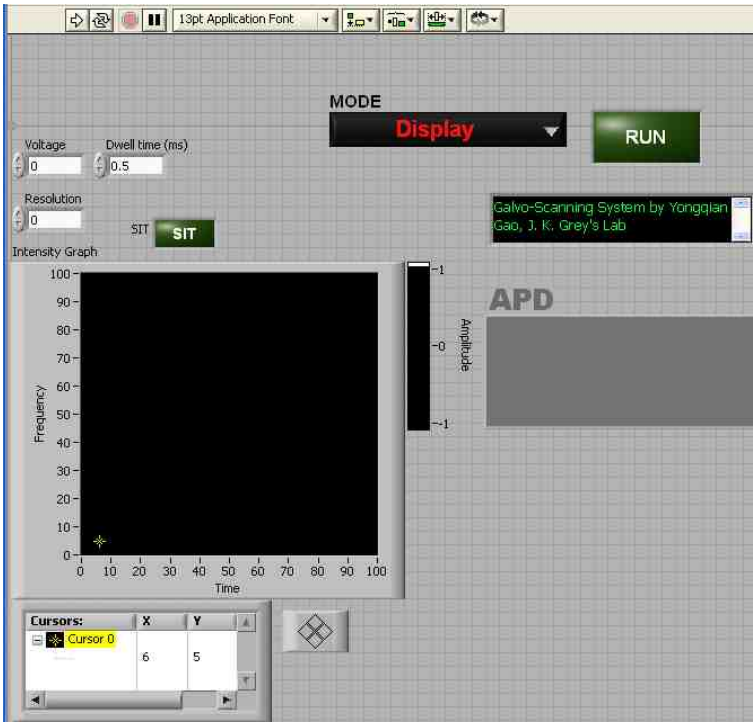

Figure A4. Front panel of Galvo microscope Labview program

This program is written to do imaging with laser beam scanning with raster moving other than the stage moves in Raman photocurrent/phase shift imaging system. The input parameters from front panel (Figure A3) include:

1) Voltage. It determines scan range, the voltage rang is 0-1V, resolution is the scan steps for each line scan.
2) Dwell time. It means time for beam stay on one position.
3) Resolution. It determines how many points for each linescan.

However, t**his program is not completed yet due to the beam scan distance is not calibrated yet.** Voltage is the driving force to move X and Y axis mirrors with a constant

angular speed thus move the beam position, to get the physical distance either one standard sample with known spacing or one accurate distance between the mirror axis and sample plane is obtained. So far, this program can perform scanning and sitting to one scanned position using SIT function if one specific position is selected by putting the cursor onto it.

Appendix D: Igor script for Raman spectrum fitting and imaging

Here is the Igor code to perform Raman spectrum analysis demonstrated in chapter 3, 4 and 5. The principle is to split the Raman C=C band into two Lorentz components with certain constraints and plot the intensity images of each component. Meanwhile, the C-C single band is fitted as single Lorentz component and plotted as intensity as well.

```
#pragma rtGlobals=1		// Use modern global access method.
#include <All IP Procedures>
#include <Image Saver>
Function twolor(w,x) : FitFunc
	Wave w
	Variable x
	// W[0] = start of X range		MUST BE HELD
	// W[1] = end of X range		MUST BE HELD
	//W[2] = linear fit of baseline
	// W[4] = amp1
	// W[6] = location1
	// W[5] = width1
	// W[7] = amp2
	// W[9] = location2
	// W[8] = width2
```

```
		Variable xr = W[1]-W[0]
		Variable xs = (2*x - (W[0] + W[1]))/xr
		return w[2] + W[3]*xs+W[4]*W[5]^2/((x-
W[6])^2+W[5]^2)+W[7]*W[8]^2/((x-W[9])^2+W[8]^2)
		End
	Macro load()
	Killwaves/A/Z
	NewPath/O path ""
	LoadWave/G/A/P=path
	Silent 1 ; PauseUpdate
	Display/N = Spectrum wave1 vs wave0
	ModifyGraph tick=2,mirror=1
	Label left "Intensity (a.u.)"
	Label bottom "Raman Shift (cm\\S-1\\M)"
	showinfo
	 end macro
	  macro smoothing( numspec)
	 variable numspec
	 prompt numspec,"enter the frames of image"
	variable i
```

```
        i=1
        do
        Smooth/E=2/S=2 45, $("wave"+ num2str(i))
        i+=1
        while(i<numspec)
        end
        macro calculation(C2_S, C2_E,C1_S, C1_E,freq1,freq2,
width,A_agg,A_un,nopix)
        variable nopix,freq1,freq2,width,A_agg,A_un
        Variable i, numspec
        variable C2_S, C2_E
        variable C1_S, C1_E
        prompt C2_S,"enter the start point of C=C mode(pixel number)"
        prompt C2_E,"enter the end point of C=C mode(pixel number)"
        prompt C1_S,"enter the start point of C-C mode(pixel number)"
        prompt C1_E,"enter the end point of C-C mode(pixel number)"
        prompt freq1, "estiamte of freq1"
        prompt freq2, "estimate of freq2"
        prompt width, "estimate of width"
        prompt A_agg, "estiamte of intensity of agg."
        prompt A_un, "estimate of unagg."
```

```
	prompt nopix,"enter the dimensions"
	numspec=nopix*nopix
	make/D/O/N =(nopix,nopix) peakareaC1
	make/o/d/n= (nopix,nopix) freqC1
	make/o/d/n= (nopix,nopix) freqFIT_1
	make/o/d/n= (nopix,nopix) freqFIT_2
	make/o/d/n= (nopix,nopix) peakareaFIT_1
	make/o/d/n= (nopix,nopix) peakareaFIT_2
	make/o/d/n= (nopix,nopix) peakareaC2
	make/o/d/n= (nopix,nopix) widthFIT_1
	make/o/d/n= (nopix,nopix) widthFIT_2
	make/o/d/n=(nopix,nopix) Ratio1_2
	make/o/d/n=(nopix,nopix) Int_agg_1
	make/o/d/n=(nopix,nopix) Int_un_1
	make/o/d/n=(nopix,nopix) Int_2_1
	Make/D/O
W_Coef1={pcsr(a),pcsr(b),vcsr(a),0.1,A_agg,freq1,width,A_un,freq2,width}
	Make/T/O TwolorConstraint = {"K6>1446","K6<1455", "K9>1465","K9 <
1475","K5>14.999","K5<15.001","K8>14.999","K8<15.001"}
	i=1
	do
```

```
CurveFit/N/Q/NTHR=0/M=2/W=0 lor, $("wave"+
num2str(i))[C1_S,C1_E]/X=wave0[C1_S,C1_E]/D
peakareaC1(i-1)=abs(W_coef[1]/sqrt(W_coef[3])*pi/2)
freqC1(i-1)=W_coef[2]
FuncFit/N/Q/NTHR=0/H="11" twolor W_coef1  $("wave"+
num2str(i))[C2_S,C2_E] /X=wave0 /D /C=TwolorConstraint
freqFIT_1(i-1)=W_coef1[6]
freqFIT_2(i-1)=W_coef1[9]
widthFIT_1(i-1)=abs(W_coef1[5]*2)
widthFIT_2(i-1)=abs(W_coef1[8]*2)
peakareaFIT_1(i-1)=abs(W_coef1[4]*W_coef1[5]*pi/2)
peakareaFIT_2(i-1)=abs(W_coef1[7]*W_coef1[8]*pi/2)
peakareaC2(i-1)=peakareaFIT_1(i-1)+peakareaFIT_2(i-1)
i += 1
while (i <= numspec)
Ratio1_2=peakareaFIT_1/peakareaFIT_2
Int_un_1=peakareaFIT_1/peakareaC1
Int_agg_1=peakareaFIT_2/peakareaC1
Int_2_1=Int_un_1+Int_agg_1
Newimage /N =Int2_1 Int_2_1
ModifyImage Int_2_1 ctab= {*,*,Rainbow,0}
```

```
ModifyGraph nticks=0
AutoSizeImage(0,3)
Newimage /N =freqC1 freqC1
ModifyImage freqC1 ctab= {*,*,Rainbow,0}
ModifyGraph nticks=0
AutoSizeImage(0,3)
Newimage /N =fre1 freqFIT_1
ModifyImage freqFIT_1 ctab= {*,*,Rainbow,0}
ModifyGraph nticks=0
AutoSizeImage(0,3)
Newimage /N =fre2 freqFIT_2
ModifyImage freqFIT_2 ctab= {*,*,Rainbow,0}
ModifyGraph nticks=0
AutoSizeImage(0,3)
Newimage /N =inten1 peakareaFIT_1
ModifyImage peakareaFIT_1 ctab= {*,*,Rainbow,0}
ModifyGraph nticks=0
Newimage /N =inten2 peakareaFIT_2
ModifyImage peakareaFIT_2 ctab= {*,*,Rainbow,0}
ModifyGraph nticks=0
Newimage /N =inten3 peakareaC2
```

```
ModifyImage peakareaC2 ctab= {*,*,Rainbow,0}

ModifyGraph nticks=0

AutoSizeImage(0,3)

Newimage /N =width1 widthFIT_1

ModifyImage widthFIT_1 ctab= {*,*,Rainbow,0}

ModifyGraph nticks=0

Newimage /N =width2 widthFIT_2

ModifyImage widthFIT_2 ctab= {*,*,Rainbow,0}

ModifyGraph nticks=0

Newimage /N =Ratio Ratio1_2

ModifyImage Ratio1_2 ctab= {*,*,Rainbow,0}

ModifyGraph nticks=0

AutoSizeImage(0,3)

Newimage /N =DensityImage1 peakareaC1

ModifyImage peakareaC1 ctab= {*,*,Rainbow,0}

ModifyImage Ratio1_2 ctab= {*,*,Rainbow,0}

ModifyGraph nticks=0

AutoSizeImage(0,3)

Newimage /N =C=C_1 C=C_1

ModifyImage C=C_1 ctab= {*,*,Rainbow,0}

ModifyGraph nticks=0
```

```
AutoSizeImage(0,3)
Newimage /N =Int_agg_1 Int_agg_1
ModifyImage Int_agg_1 ctab= {*,*,Rainbow,0}
ModifyGraph nticks=0
AutoSizeImage(0,3)
Newimage /N =Int_un_1 Int_un_1
ModifyImage Int_un_1 ctab= {*,*,Rainbow,0}
ModifyGraph nticks=0
AutoSizeImage(0,3)
colorscale
Newimage /N =DensityImage2 pkareaC2
ModifyImage pkareaC2 ctab= {*,*,Rainbow,0}
colorscale
end macro
macro piontspec()
variable nopix
variable x,y,c
killwaves wavec
make/o/d/n= (1600) wavec
x=xcsr(a)
y=vcsr(a)
```

```
c=y*nopix+x+1
wavec= $("wave"+ num2str(c))
display wavec vs wave0
end macro
```

To run this code, just load this code which has been saved as one file called Raman_052209.ipf, and compile it to be executable, Under “Macro” menu, “load” menu is to load the .asc format file. For “smoothing” function , unless the signal/noise ratio is too noisy, do not run this function, because probably it may distort the lineshape of spectra, if it is has to be used, the number 45 in the line *Smooth/E=2/S=2 45, $("wave"+ num2str(i)),* can be changed to samller number to be less distorted. **This smoothing function is not used in our published results**. Preferably, change data collecting conditions to get better spectra not to smooth it, just leave the function here just in case we need it. Select “Calculation”, and then there will be one pop up window to ask for the parameters like shown here:

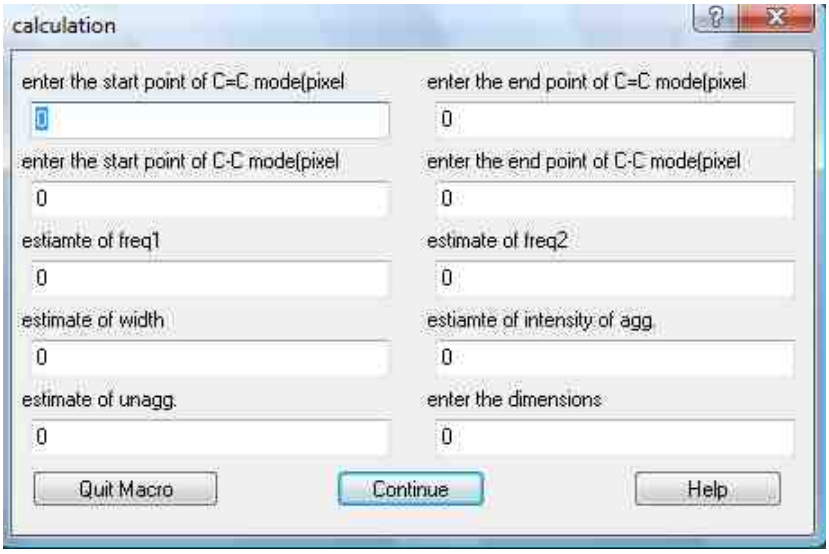

Figure A5. The window for input parameters of Raman imaging program

As for the peak region, only pixel values as position inputs are needed, i.e., if the CCD pixel number 600 corresponds 1400 cm^{-1}, input 600 not 1400; freq1 and freq2 are the two components frequency, normally they are around 1450 and 1470 cm^{-1}; width is fixed as 15; intensity of agg. and unagg. are relative to the original intensity; "dimensions" is the same number as the value of dimension in Labview imaging program. **Before run the calculation, find the proper range of C-C and C=C band using cursors.**

Appendix E: Igor script for weakly H aggregated absorption spectrum fit function and instructions

The script is used to perform an absorption spectrum fitting based on the weakly coupled H aggregated model (Here it is called SpanoFit). Here is the Igor code:

```
Function spanoFit(w,x) :Fitfunc
 wave w
 Variable x
//NOTE:THIS FIT IS USED TO FIT AGGREGATED P3HT ABSORPTION ONLY.
// modified inteisty is desacribed as: A=sumF.C. (1-G*W*exp(-s)/2E0)^2*Gaussian (E00, E0, x)
//S=1.0;
//E00=16500;
//E0=1400;
Variable G0= W[1]+W[1]^2/factorial (2)/2+W[1]^3/ factorial (3)/3+W[1]^4/factorial (4)/4+W[1]^5/factorial (5)/5
Variable G1=-1+W[1]^2/factorial (2)+W[1]^3/ factorial (3)/2+W[1]^4/factorial (4)/3+W[1]^5/factorial (5)/4
Variable G2=-1/2-W[1]+W[1]^3/ factorial (3)+W[1]^4/factorial (4)/2+W[1]^5/factorial (5)/3+W[1]^6/factorial (6)/4
```

```
Variable G3=-1/3-W[1]/2-W[1]^2/factorial (2)+W[1]^4/factorial
(4)/1+W[1]^5/factorial (5)/2+W[1]^6/factorial (6)/3
Variable G4=-1/4-W[1]/3-W[1]^2/factorial (2)/2-W[1]^3/factorial
(3)/1+W[1]^5/factorial (5)/1+W[1]^6/factorial (6)/2+W[1]^7/factorial (7)/3
Variable F1=exp(-W[1])*exp(-(x-16500)^2/W[2]^2)
variable F2=exp(-(x-16500-W[3])^2/W[2]^2)
Variable F3=exp(-(x-16500-2*W[3])^2/W[2]^2)
Variable F4=exp(-(x-16500-3*W[3])^2/W[2]^2)
Variable F5=exp(-(x-16500-4*W[3])^2/W[2]^2)
return W[0]*(F1*(1-G0*0.12*exp (-W[1])/2/0.173)^2+W[1]*exp(-W[1])*F2*(1-
G1*0.12*exp (-W[1])/2/0.173)^2+W[1]^2*exp(-W[1])/2*F3*(1-G2*0.12*exp (-
W[1])/2/0.173)^2+W[1]^3*exp(-W[1])/6*F4*(1-G3*0.12*exp (-
W[1])/2/0.173)^2+W[1]^4*exp(-W[1])/24*F5*(1-G4*0.12*exp (-W[1])/2/0.173)^2)
End
Macro load()
string filename
Killwaves/A/Z
NewPath/O path ""
LoadWave/G/A/P=path //filename
Silent 1 ; PauseUpdate
Display/N = Spectrum wave1 vs wave0
```

```
wave0=1e7/wave0
ModifyGraph tick=2,mirror=1
Label left "Intensity (a.u.)"
Label bottom "Wavelnumber (cm-1)"
showinfo
 End
```

To run the script, open Igor Pro program and load the script. Then click the Marco menu to compile the file, the submenu should be seen under Macro menu, click the “load” menu from Macro, it will pop up one window to ask for loading the spectrum from one directory, **it can only load .asc format files**. The “load” menu will load the absorption file and plot it in the window. The x-axis has been converted into wavenumber, which is needed for executing the Spanofit function. Then select the fitting range by putting two cursors onto the plot. From “Curve Fitting” menu, select Spanofit, and put in initial guess values for all the variables, then click “do it”, the fitting process should start running and append the fitting curve onto the original absorption spectrum. Adjust the fitting parameters to get good fit.

Appendix F Labview script for EQE measurement.

This script is used to do EQE measurements. Two function generators are used as power supply for the monochromator, Keithley 2635 is used to record photocurrent as demonstrated previously. The communication between computer and Keithley is through GPIB and PCI 6024E (through BNC 2110 board). The parameters we need to set are from front paneld as shown in Figure A6. The variables for this program include:

1) Starting wavelength. Typically this is set as 300 or 350 nm.
2) End wavelength. Since for P3HT: PCBM solar cells, there is no noticeable absorption beyond 700 nm, set as 650 or 700 nm is good enough.
3) Gain. The purpose of this value is a factor to multiply measured photocurrent so that computer can display correctly. For safe 1E 9 is used generally, which means the current displayed as unit of nA.
4) Level. The applied bias, for EQE measurement, set as 0.
5) Source function and Measure function. These two settings are for Keithley, select voltage as source function for current measurement, and current as measure function.
6) Visa resource name. This is the GPIB address of Keithley, 26 is the default address.

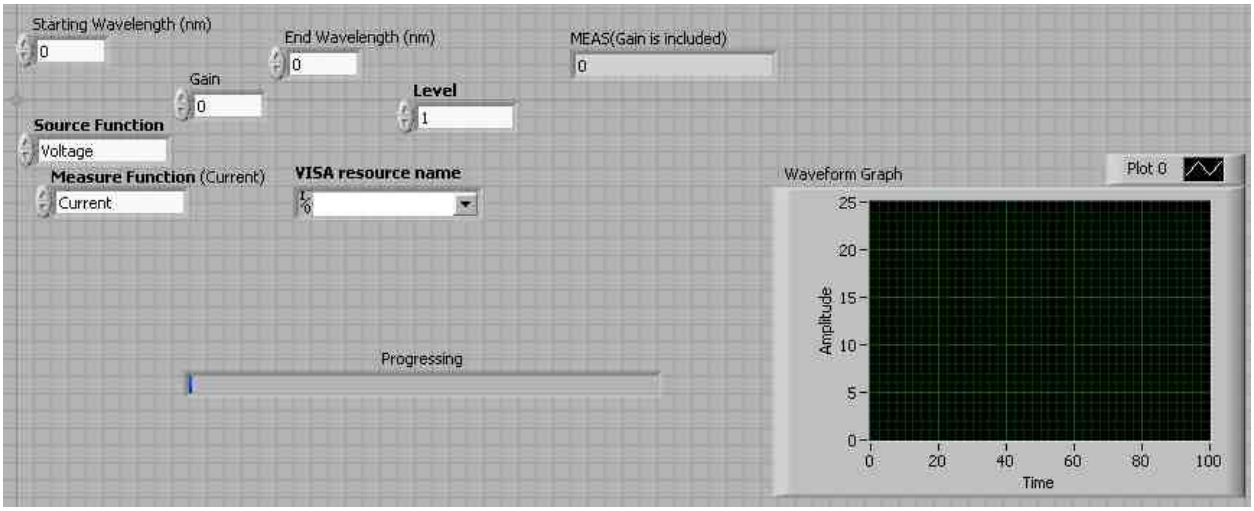

Figure A6. Parameters required for EQE measurement are set from the front panel of EQE measurement Labview script.

References

(1) Hoppe, H.; Sariciftci, N. S. *J. Mater. Chem.* **2006**, *16*, 45.

(2) Yah, W. O.; Wang, Z.; Otsuka, H.; Kato, K.; Kim, J.; Takata, M.; Takahara, A. *ACS Appl. Mater. Interfaces* **2009**, *1*, 1544.

(3) Huynh, W. U.; Dittmer, J. J.; Libby, W. C.; Whiting, G. L.; Alivisatos, A. P. *Adv. Funct. Mater.* **2003**, *13*, 73.

(4) Halls, J. J. M.; Arias, A. C.; MacKenzie, J. D.; Wu, W.; Inbasekaran, M.; Woo, E. P.; Friend, R. H. *Advanced Materials (Weinheim, Germany)* **2000**, *12*, 498.

(5) Liu, J.; Zhang, R.; Sauve, G.; Kowalewski, T.; McCullough, R. D. *J. Am. Chem. Soc.* **2008**, *130*, 13167.

(6) Schwartz, B. J. *Annual Review of Physical Chemistry* **2003**, *54*, 141.

(7) Kline, R. J.; DeLongchamp, D. M.; Fischer, D. A.; Lin, E. K.; Heeney, M.; McCulloch, I.; Toney, M. F. *Appl. Phys. Lett.* **2007**, *90*, 062117/1.

(8) Gregg, B. A. *Journal of Physical Chemistry B* **2003**, *107*, 4688.

(9) Granstrom, M.; Petritsch, K.; Arias, A. C.; Lux, A.; Andersson, M. R.; Friend, R. H. *Nature* **1998**, *395*, 257.

(10) Yu, G.; Heeger, A. J. *J. Appl. Phys.* **1995**, *78*, 4510.

(11) Scully, S. R.; McGehee, M. D. *J. Appl. Phys.* **2006**, *100*, 034907/1.

(12) Knupfer, M. *Appl. Phys. A: Mater. Sci. Process.* **2003**, *77*, 623.

(13) Moses, D.; Wang, J.; Heeger, A. J.; Kirova, N.; Brazovski, S. *Proc. Natl. Acad. Sci. U. S. A.* **2001**, *98*, 13496.

(14) Yang, C. Y.; Heeger, A. J. *Synthetic Metals* **1996**, *83*, 85.

(15) Arias, A. C.; MacKenzie, J. D.; Stevenson, R.; Halls, J. J. M.; Inbasekaran, M.; Woo, E. P.; Richards, D.; Friend, R. H. *Macromolecules* **2001**, *34*, 6005.

(16) Videlot, C.; Ackermann, J.; El Kassmi, A.; Raynal, P. *Thin Solid Films* **2002**, *403-404*, 380.

(17) Peumans, P.; Uchida, S.; Forrest, S. R. *Nature* **2003**, *425*, 158.

(18) Peet, J.; Kim, J. Y.; Coates, N. E.; Ma, W. L.; Moses, D.; Heeger, A. J.; Bazan, G. C. *Nat Mater* **2007**, *6*, 497.

(19) Conboy, J. C.; Olson, E. J. C.; Adams, D. M.; Kerimo, J.; Zaban, A.; Gregg, B. A.; Barbara, P. F. *J. Phys. Chem. B* **1998**, *102*, 4516.

(20) Tang, C. W. *Appl. Phys. Lett.* **1986**, *48*, 183.

(21) Burroughes, J. H.; Bradley, D. D. C.; Brown, A. R.; Marks, R. N.; Mackay, K.; Friend, R. H.; Burns, P. L.; Holmes, A. B. *Nature* **1990**, *347*, 539.

(22) Woo, H. S.; Graham, S. C.; Halliday, D. A.; Bradley, D. D. C.; Friend, R. H.; Burn, P. L.; Holmes, A. B. *Phys. Rev. B* **1992**, *46*, 7379.

(23) Sariciftci, N. S.; Braun, D.; Zhang, C.; Srdanov, V. I.; Heeger, A. J.; Stucky, G.; Wudl, F. *Appl. Phys. Lett.* **1993**, *62*, 585.

(24) Patil, A. O.; Heeger, A. J.; Wudl, F. *Chem. Rev.* **1988**, *88*, 183.

(25) Umeda, T.; Hashimoto, Y.; Mizukami, H.; Shirakawa, T.; Fujii, A.; Yoshino, K. *Synthetic Metals* **2005**, *152*, 93.

(26) Sandberg, H. G. O.; Frey, G. L.; Shkunov, M. N.; Sirringhaus, H.; Friend, R. H.; Nielsen, M. M.; Kumpf, C. *Langmuir* **2002**, *18*, 10176.

(27) Bao, Z.; Dodabalapur, A.; Lovinger, A. J. *Appl. Phys. Lett.* **1996**, *69*, 4108.

(28) Horowitz, G. *Adv. Mater.* **1998**, *10*, 365.

(29) Chua, L.-L.; Zaumseil, J.; Chang, J.-F.; Ou, E. C. W.; Ho, P. K. H.; Sirringhaus, H.; Friend, R. H. *Nature* **2005**, *434*, 194.

(30) Zaumseil, J.; Donley, C. L.; Kim, J.-S.; Friend, R. H.; Sirringhaus, H. *Adv. Mater.* **2006**, *18*, 2708.

(31) Gross, M.; Muller, D. C.; Nothofer, H. G.; Scherf, U.; Neher, D.; Brauchle, C.; Meerholz, K. *Nature* **2000**, *405*, 661.

(32) Anderson, J. D.; McDonald, E. M.; Lee, P. A.; Anderson, M. L.; Ritchie, E. L.; Hall, H. K.; Hopkins, T.; Mash, E. A.; Wang, J.; Padias, A.; Thayumanavan, S.; Barlow, S.; Marder, S. R.; Jabbour, G. E.; Shaheen, S.; Kippelen, B.; Peyghambarian, N.; Wightman, R. M.; Armstrong, N. R. Electrochemistry and Electrogenerated Chemiluminescence Processes of the Components of Aluminum Quinolate/Triarylamine, and Related Organic Light-Emitting Diodes. In *J. Am. Chem. Soc.*; ACS, 1998; Vol. 120; pp 9646.

(33) Paasch, G.; Scheinert, S. *Synthetic Metals* **2001**, *122*, 145.

(34) Martin, S. J.; Lupton, J. M.; Samuel, I. D. W.; Walker, A. B. *Journal of Physics-Condensed Matter* **2002**, *14*, 9925.

(35) Greenham, N. C.; Moratti, S. C.; Bradley, D. D. C.; Friend, R. H.; Holmes, A. B. *Nature* **1993**, *365*, 628.

(36) Shaheen, S. E.; Radspinner, R.; Peyghambarian, N.; Jabbour, G. E. *Appl. Phys. Lett.* **2001**, *79*, 2996.

(37) Martens, T.; D'Haen, J.; Munters, T.; Beelen, Z.; Goris, L.; Manca, J.; D'Olieslaeger, M.; Vanderzande, D.; De, S. L.; Andriessen, R. *Synth. Met.* **2003**, *138*, 243.

(38) Smith, A. P.; Smith, R. R.; Taylor, B. E.; Durstock, M. F. *Chem. Mater.* **2004**, *16*, 4687.

(39) Hoppe, H.; Drees, M.; Schwinger, W.; Schaffler, F.; Sariciftcia, N. S. *Synth. Met.* **2005**, *152*, 117.

(40) Pacios, R.; Bradley, D. D. C.; Nelson, J.; Brabec, C. J. *Synth. Met.* **2003**, *137*, 1469.

(41) Alam, M. M.; Jenekhe, S. A. *J. Phys. Chem. B* **2001**, *105*, 2479.

(42) Grant, C. D.; Schwartzberg, A. M.; Smestad, G. P.; Kowalik, J.; Tolbert, L. M.; Zhang, J. Z. *Synth. Met.* **2003**, *132*, 197.

(43) Kim, Y.; Choulis, S. A.; Nelson, J.; Bradley, D. D. C.; Cook, S.; Durrant, J. R. *J. Mater. Sci.* **2005**, *40*, 1371.

(44) Nguyen, L. H.; Hoppe, H.; Erb, T.; Guenes, S.; Gobsch, G.; Sariciftci, N. S. *Adv. Funct. Mater.* **2007**, *17*, 1071.

(45) Reyes-Reyes, M.; Kim, K.; Carroll, D. L. *Appl. Phys. Lett.* **2005**, *87*, 083506/1.

(46) Li, G.; Shrotriya, V.; Huang, J.; Yao, Y.; Moriarty, T.; Emery, K.; Yang, Y. *Nat. Mater.* **2005**, *4*, 864.

(47) Kim, Y.; Cook, S.; Tuladhar, S. M.; Choulis, S. A.; Nelson, J.; Durrant, J. R.; Bradley, D. D. C.; Giles, M.; McCulloch, I.; Ha, C.-S.; Ree, M. *Nat. Mater.* **2006**, *5*, 197.

(48) Ma, W.; Yang, C.; Gong, X.; Lee, K.; Heeger, A. J. *Adv. Funct. Mater.* **2005**, *15*, 1617.

(49) Guenes, S.; Neugebauer, H.; Sariciftci, N. S. *Chem. Rev.* **2007**, *107*, 1324.

(50) Brabec, C. J.; Durrant, J. R. *MRS Bull.* **2008**, *33*, 670.

(51) Brabec, C. J.; Sariciftci, N. S.; Hummelen, J. C. *Advanced Functional Materials* **2001**, *11*, 15.

(52) Hoppe, H.; Sariciftci, N. S. *J. Mater. Res.* **2004**, *19*, 1924.

(53) Scheblykin, I. G.; Yartsev, A.; Pullerits, T.; Gulbinas, V.; Sundstroem, V. *J. Phys. Chem. B* **2007**, *111*, 6303.

(54) Allemand, P. M.; Koch, A.; Wudl, F.; Rubin, Y.; Diederich, F.; Alvarez, M. M.; Anz, S. J.; Whetten, R. L. *J. Am. Chem. Soc.* **1991**, *113*, 1050.

(55) Sirringhaus, H.; Brown, P. J.; Friend, R. H.; Nielsen, M. M.; Bechgaard, K.; Langeveld-Voss, B. M. W.; Spiering, A. J. H.; Janssen, R. A. J.; Meijer, E. W.; Herwig, P.; De, L. D. M. *Nature* **1999**, *401*, 685.

(56) Sirringhaus, H.; Tessler, N.; Friend, R. H. *Science* **1998**, *280*, 1741.

(57) Marsh, R. A.; Hodgkiss, J. M.; Albert-Seifried, S.; Friend, R. H. *Nano Lett.* **2011**, *10*, 923.

(58) Dennler, G.; Lungenschmied, C.; Neugebauer, H.; Sariciftci, N. S.; Labouret, A. *J. Mater. Res.* **2005**, *20*, 3224.

(59) Yang, X.; Loos, J. *Macromolecules* **2007**, *40*, 1353.

(60) Guo, T.-F.; Wen, T.-C.; Pakhomov, G. L. v.; Chin, X.-G.; Liou, S.-H.; Yeh, P.-H.; Yang, C.-H. *Thin Solid Films* **2008**, *516*, 3138.

(61) Vanlaeke, P.; Vanhoyland, G.; Aernouts, T.; Cheyns, D.; Deibel, C.; Manca, J.; Heremans, P.; Poortmans, J. *Thin Solid Films* **2006**, *511-512*, 358.

(62) Yao, Y.; Hou, J.; Xu, Z.; Li, G.; Yang, Y. *Adv. Funct. Mater.* **2008**, *18*, 1783.

(63) Li, G.; Yao, Y.; Yang, H.; Shrotriya, V.; Yang, G.; Yang, Y. *Adv. Funct. Mater.* **2007**, *17*, 1636.

(64) Roncali, J. *Acc. Chem. Res.* **2009**, *42*, 1719.

(65) Lee, J. K.; Ma, W. L.; Brabec, C. J.; Yuen, J.; Moon, J. S.; Kim, J. Y.; Lee, K.; Bazan, G. C.; Heeger, A. J. *J. Am. Chem. Soc.* **2008**, *130*, 3619.

(66) Camaioni, N.; Ridolfi, G.; Casalbore-Miceli, G.; Possamai, G.; Maggini, M. *Adv. Mater.* **2002**, *14*, 1735.

(67) Padinger, F.; Rittberger, R. S.; Sariciftci, N. S. *Adv. Funct. Mater.* **2003**, *13*, 85.

(68) Ayzner, A. L.; Wanger, D. D.; Tassone, C. J.; Tolbert, S. H.; Schwartz, B. J. *J. Phys. Chem. C* **2008**, *112*, 18711.

(69) Dante, M.; Peet, J.; Nguyen, T.-Q. *J. Phys. Chem. C* **2008**, *112*, 7241.

(70) Zhong, H.; Yang, X.; de With, B.; Loos, J. *Macromolecules* **2006**, *39*, 218.

(71) Huynh, W. U.; Dittmer, J. J.; Libby, W. C.; Whiting, G. L.; Alivisatos, A. P. *Adv. Funct. Mater.* **2003**, *13*, 73.

(72) Erb, T.; Zhokhavets, U.; Gobsch, G.; Raleva, S.; Stuehn, B.; Schilinsky, P.; Waldauf, C.; Brabec, C. J. *Adv. Funct. Mater.* **2005**, *15*, 1193.

(73) Mayer, A. C.; Toney, M. F.; Scully, S. R.; Rivnay, J.; Brabec, C. J.; Scharber, M.; Koppe, M.; Heeney, M.; McCulloch, I.; McGehee, M. D. *Adv. Funct. Mater.* **2009**, *19*, 1173.

(74) Chu, C.-W.; Yang, H.; Hou, W.-J.; Huang, J.; Li, G.; Yang, Y. *Appl. Phys. Lett.* **2008**, *92*, 103306/1.

(75) Yang, X.; Loos, J.; Veenstra, S. C.; Verhees, W. J. H.; Wienk, M. M.; Kroon, J. M.; Michels, M. A. J.; Janssen, R. A. J. *Nano Lett.* **2005**, *5*, 579.

(76) Silveira, W. R.; Marohn, J. A. *Phys. Rev. Lett.* **2004**, *93*, 116104.

(77) Nardes, A. M.; Kemerink, M.; Janssen, R. A. J.; Bastiaansen, J. A. M.; Kiggen, N. M. M.; Langeveld, B. M. W.; van Breemen, A. J. J. M.; de Kok, M. M. *Adv. Mater.* **2007**, *19*, 1196.

(78) Coffey, D. C.; Reid, O. G.; Rodovsky, D. B.; Bartholomew, G. P.; Ginger, D. S. *Nano Lett.* **2007**, *7*, 738.

(79) Coffey, D. C.; Ginger, D. S. *Nat. Mater.* **2006**, *5*, 735.

(80) Pingree, L. S. C.; Reid, O. G.; Ginger, D. S. *Nano Lett.* **2009**, *9*, 2946.

(81) Alexeev, A.; Loos, J.; Koetse, M. M. *Ultramicroscopy* **2006**, *106*, 191.

(82) Lin, H.-N.; Lin, H.-L.; Wang, S.-S.; Yu, L.-S.; Perng, G.-Y.; Chen, S.-A.; Chen, S.-H. *Appl. Phys. Lett.* **2002**, *81*, 2572.

(83) Kim, H.-J.; Kim, D.-C.; Kim, R.; Kim, J.; Park, D.-H.; Kim, H.-S.; Joo, J.; Suh, Y. D. *J. Appl. Phys.* **2007**, *101*, 053514/1.

(84) Bazzaoui, E. A.; Marsault, J. P.; Aeiyach, S.; Lacaze, P. C. *Synth. Met.* **1994**, *66*, 217.

(85) Louarn, G.; Trznadel, M.; Buisson, J. P.; Laska, J.; Pron, A.; Lapkowski, M.; Lefrant, S. *J. Phys. Chem.* **1996**, *100*, 12532.

(86) Klimov, E.; Li, W.; Yang, X.; Hoffmann, G. G.; Loos, J. *Macromolecules* **2006**, *39*, 4493.

(87) Osterbacka, R.; An, C. P.; Jiang, X. M.; Vardeny, Z. V. *Science* **2000**, *287*, 839.

(88) Sirringhaus, H.; Brown, P. J.; Friend, R. H.; Nielsen, M. M.; Bechgaard, K.; Langeveld-Voss, B. M. W.; Spiering, A. J. H.; Janssen, R. A. J.; Meijer, E. W.; Herwig, P.; De Leeuw, D. M. *Nature* **1999**, *401*, 685.

(89) Spano, F. C. *J. Chem. Phys.* **2005**, *122*, 234701/1.

(90) Spano, F. C. *Chem. Phys*. **2006**, *325*, 22.

(91) Manas, E. S.; Spano, F. C. *J. Chem. Phys.* **1998**, *109*, 8087.

(92) Clark, J.; Silva, C.; Friend, R. H.; Spano, F. C. *Phys. Rev. Lett.* **2007**, *98*, 206406/1.

(93) Scheibe, G. *Angew. Chem.* **1937**, *50*.

(94) Scheibe, G. *Angew. Chem.* **1936**, *49*.

(95) Jelley, E. E. *Nature* **1936**, *138*.

(96) Clark, J.; Chang, J.-F.; Spano, F. C.; Friend, R. H.; Silva, C. *Appl. Phys. Lett.* **2009**, *94*, 163306/1.

(97) Shriver, D. F.; Dunn, J. B. R. *Appl. Spectrosc.* **1974**, *28*, 319.

(98) Peter, L. M. *Chemical Reviews* **1990**, *90*, 753.

(99) Hickey, S. G.; Riley, D. J. *Electrochimica Acta* **2000**, *45*, 3277.

(100) Dloczik, L.; Ileperuma, O.; Lauermann, I.; Peter, L. M.; Ponomarev, E. A.; Redmond, G.; Shaw, N. J.; Uhlendorf, I. *J. Phys. Chem. B* **1997**, *101*, 10281.

(101) Krijger, J.; Plass, R.; Gratzel, M.; Cameron, P. J.; Peter, L. M. *J. Phys. Chem. B* **2003**, *107*, 7536.

(102) Franco, G.; Peter, L. M.; Ponomarev, E. A. *Electrochemistry Communications* **1999**, *1*, 61.

(103) Bag, M.; Narayan, K. S. *Phys. Rev. B: Condens. Matter* **2010**, *82*, 075308.

(104) Byers, J. C.; Ballantyne, S.; Rodionov, K.; Mann, A.; Semenikhin, O. A. *ACS Appl. Mater. Interfaces* **2011**, ASAP.

(105) Yu, G.; Gao, J.; Hummelen, J. C.; Wudl, F.; Heeger, A. J. *Science* **1995**, *270*, 1789.

(106) Coakley, K. M.; McGehee, M. D. *Chem. Mater.* **2004**, *16*, 4533.

(107) Sariciftci, N. S.; Smilowitz, L.; Heeger, A. J.; Wudl, F. *Science* **1992**, *258*, 1474.

(108) Halls, J. J. M.; Walsh, C. A.; Greenham, N. C.; Marseglia, E. A.; Friend, R. H.; Moratti, S. C.; Holmes, A. B. *Nature* **1995**, *376*, 498.

(109) Shaheen, S. E.; Brabec, C. J.; Sariciftci, N. S.; Padinger, F.; Fromherz, T.; Hummelen, J. C. *Appl. Phys. Lett.* **2001**, *78*, 841.

(110) Campoy-Quiles, M.; Ferenczi, T.; Agostinelli, T.; Etchegoin, P. G.; Kim, Y.; Anthopoulos, T. D.; Stavrinou, P. N.; Bradley, D. D. C.; Nelson, J. *Nat. Mater.* **2008**, *7*, 158.

(111) Scharber, M. C.; Muehlbacher, D.; Koppe, M.; Denk, P.; Waldauf, C.; Heeger, A. J.; Brabec, C. J. *Adv. Mater.* **2006**, *18*, 789.

(112) Thompson, B. C.; Frechet, J. M. J. *Angew. Chem., Int. Ed.* **2008**, *47*, 58.

(113) Li, G.; Yao, Y.; Yang, H.; Shrotriya, V.; Yang, G.; Yang, Y. *Adv. Funct. Mater.* **2007**, *17*, 1636.

(114) Li, G.; Shrotriya, V.; Yao, Y.; Yang, Y. *J. Appl. Phys.* **2005**, *98*, 043704/1.

(115) Li, G.; Shrotriya, V.; Yao, Y.; Huang, J.; Yang, Y. *J. Mater. Chem.* **2007**, *17*, 3126.

(116) Xin, H.; Kim, F. S.; Jenekhe, S. A. *J. Am. Chem. Soc.* **2008**, *130*, 5424.

(117) Lee, S. H.; Park, D. H.; Kim, K.; Joo, J.; Kim, D.-C.; Kim, H.-J.; Kim, J. *Appl. Phys. Lett.* **2008**, *91*, 263102/1.

(118) Li, L.; Lu, G.; Yang, X. *J. Mater. Chem.* **2008**, *18*, 1984.

(119) Sohn, Y.; Stuckless, J. T. *Applied Physics Letters* **2007**, *90*, 171901/1.

(120) Miller, S.; Fanchini, G.; Lin, Y.-Y.; Li, C.; Chen, C.-W.; Su, W.-F.; Chhowalla, M. *J. Mater. Chem.* **2008**, *18*, 306.

(121) Vukmirovic, N.; Wang, L.-W. *J. Phys. Chem. B* **2008**, *113*, 409.

(122) Casado, J.; Hicks, R. G.; Hernandez, V.; Myles, D. J. T.; Ruiz Delgado, M. C.; Lopez Navarrete, J. T. *J. Chem. Phys.* **2003**, *118*, 1912.

(123) Yun, J.-J.; Peet, J.; Cho, N.-S.; Bazan, G. C.; Lee, S. J.; Moskovits, M. *Appl. Phys. Lett.* **2008**, *92*, 251912/1.

(124) Milani, A.; Brambilla, L.; Zoppo, M. D.; Zerbi, G. *J. Phys. Chem. B* **2007**, *111*, 1271.

(125) Bruevich, V. V.; Makhmutov, T. S.; Elizarov, S. G.; Nechvolodova, E. M.; Paraschuk, D. Y. *J. Chem. Phys.* **2007**, *127*, 104905/1.

(126) Bao, Q.; Gan, Y.; Li, J.; Li, C. M. *J. Phys. Chem. C* **2008**, *112*, 19718.

(127) Janssen, G.; Aguirre, A.; Goovaerts, E.; Vanlaeke, P.; Poortmans, J.; Manca, J. *Eur. Phys. J.: Appl. Phys.* **2007**, *37*, 287.

(128) Koren, A. B.; Curtis, M. D.; Francis, A. H.; Kampf, J. W. *J. Am. Chem. Soc.* **2003**, *125*, 5040.

(129) Brown, P. J.; Thomas, D. S.; Kohler, A.; Wilson, J. S.; Kim, J.-S.; Ramsdale, C. M.; Sirringhaus, H.; Friend, R. H. *Phys. Rev. B* **2003**, *67*, 064203/1.

(130) Gurau, M. C.; Delongchamp, D. M.; Vogel, B. M.; Lin, E. K.; Fischer, D. A.; Sambasivan, S.; Richter, L. J. *Langmuir* **2007**, *23*, 834.

(131) Malgas, G. F.; Arendse, C. J.; Mavundla, S.; Cummings, F. R. *J. Mater. Sci.* **2008**, *43*, 5599.

(132) Vanlaeke, P.; Swinnen, A.; Haeldermans, I.; Vanhoyland, G.; Aernouts, T.; Cheyns, D.; Deibel, C.; D'Haen, J.; Heremans, P.; Poortmans, J.; Manca, J. V. *Sol. Energy Mater. Sol. Cells* **2006**, *90*, 2150.

(133) Louarn, G.; Buisson, J. P.; Lefrant, S.; Fichou, D. *J. Phys. Chem.* **1995**, *99*, 11399.

(134) Prosa, T. J.; Winokur, M. J.; McCullough, R. D. *Macromolecules* **1996**, *29*, 3654.

(135) Savenije, T. J.; Kroeze, J. E.; Yang, X.; Loos, J. *Thin Solid Films* **2006**, *511-512*, 2.

(136) Savenije, T. J.; Kroeze, J. E.; Yang, X.; Loos, J. *Adv. Funct. Mater.* **2005**, *15*, 1260.

(137) McNeill, C. R.; Watts, B.; Thomsen, L.; Ade, H.; Greenham, N. C.; Dastoor, P. C. *Macromolecules* **2007**, *40*, 3263.

(138) McNeill, C. R.; Westenhoff, S.; Groves, C.; Friend, R. H.; Greenham, N. C. *J. Phys. Chem. C* **2007**, *111*, 19153.

(139) McNeill, C. R.; Watts, B.; Thomsen, L.; Belcher, W. J.; Greenham, N. C.; Dastoor, P. C. *Nano Lett.* **2006**, *6*, 1202.

(140) Reid, O. G.; Munechika, K.; Ginger, D. S. *Nano Lett.* **2008**, *8*, 1602.

(141) McNeill, C. R.; Frohne, H.; Holdsworth, J. L.; Furst, J. E.; King, B. V.; Dastoor, P. C. *Nano Lett.* **2004**, *4*, 219.

(142) Gao, Y.; Grey, J. K. *J. Am. Chem. Soc.* **2009**, *131*, 9654.

(143) Hoppe, H.; Glatzel, T.; Niggemann, M.; Schwinger, W.; Schaeffler, F.; Hinsch, A.; Lux-Steiner, M. C.; Sariciftci, N. S. *Thin Solid Films* **2006**, *511-512*, 587.

(144) Koster, L. J. A.; Mihailetchi, V. D.; Blom, P. W. M. *Applied Physics Letters* **2006**, *88*, 052104/1.

(145) Arkhipov, V. I.; Fishchuk, I. I.; Kadashchuk, A.; Baessler, H. *Photophys. Mol. Mater.* **2006**, 261.

(146) Coropceanu, V.; Cornil, J.; Da, S. F. D. A.; Olivier, Y.; Silbey, R.; Bredas, J.-L. *Chem. Rev. (Washington, DC, U. S.)* **2007**, *107*, 926.

(147) Sims, M.; Tuladhar, S. M.; Nelson, J.; Maher, R. C.; Campoy-Quiles, M.; Choulis, S. A.; Mairy, M.; Bradley, D. D. C.; Etchegoin, P. G.; Tregidgo, C.; Suhling, K.; Richards, D. R.; Massiot, P.; Nielsen, C. B.; Steinke, J. H. G. *Phys. Rev. B: Condens. Matter Mater. Phys.* **2007**, *76*, 195206/1.

(148) Tessler, N.; Preezant, Y.; Rappaport, N.; Roichman, Y. *Adv. Mater.* **2009**, *21*, 2741.

(149) Cornil, J.; Beljonne, D.; Calbert, J.-P.; Bredas, J.-L. *Adv. Mater.* **2001**, *13*, 1053.

(150) Bao, Q.; Bao, S.; Li, C. M.; Qi, X.; Pan, C.; Zang, J.; Wang, W.; Tang, D. Y. *Chemistry of Materials* **2007**, *19*, 5965.

(151) Craley, C. R.; Zhang, R.; Kowalewski, T.; McCullough, R. D.; Stefan, M. C. *Macromol. Rapid Commun.* **2009**, *30*, 11.

(152) Bao, Q.; Li, J.; Li, C. M.; Dong, Z. L.; Lu, Z.; Qin, F.; Gong, C.; Guo, J. *Journal of Physical Chemistry B* **2008**, *112*, 12270.

(153) Chen, L.-M.; Hong, Z.; Li, G.; Yang, Y. *Adv. Mater.* **2009**, *21*, 1434.

(154) Peet, J.; Heeger, A. J.; Bazan, G. C. *Acc. Chem. Res.* **2009**, *42*, 1700.

(155) Lan, Y.-K.; Huang, C.-I. *J. Phys. Chem. B* **2009**, *113*, 14555.

(156) Becerril, H. A.; Miyaki, N.; Tang, M. L.; Mondal, R.; Sun, Y.-S.; Mayer, A. C.; Parmer, J. E.; McGehee, M. D.; Bao, Z. *Journal of Materials Chemistry* **2009**, *19*, 591.

(157) Kobayashi, T.; Hamazaki, J.-i.; Kunugita, H.; Ema, K.; Endo, T.; Rikukawa, M.; Sanui, K. *Phys. Rev. B* **2003**, *67*, 205214.

(158) Gao, Y.; Martin, T. P.; Thomas, A. K.; Grey, J. K. *J. Phys. Chem. Lett.* **2010**, *1*, 178.

(159) Lapkowski, M.; Pron, A. *Synth. Met.* **2000**, *110*, 79.

(160) Zhokhavets, U.; Erb, T.; Gobsch, G.; Al-Ibrahim, M.; Ambacher, O. *Chemical Physics Letters* **2006**, *418*, 347.

(161) MouleÌ□, A. J.; Allard, S.; Kronenberg, N. M.; Tsami, A.; Scherf, U.; Meerholz, K. *The Journal of Physical Chemistry C* **2008**, *112*, 12583.

(162) Hess, B. C.; Kanner, G. S.; Vardeny, Z. *Phys. Rev. B* **1993**, *47*, 1407.

(163) Louarn, G.; Trznadel, M.; Zagorska, M.; Lapkowski, M.; Pron, A.; Buisson, J. P.; Lefrant, S. *Synth. Met.* **1997**, *84*, 579.

(164) Hoppe, H.; Niggemann, M.; Winder, C.; Kraut, J.; Hiesgen, R.; Hinsch, A.; Meissner, D.; Sariciftci, N. S. *Advanced Functional Materials* **2004**, *14*, 1005.

(165) Huang, Y.-C.; Chuang, S.-Y.; Wu, M.-C.; Chen, H.-L.; Chen, C.-W.; Su, W.-F. *Journal of Applied Physics* **2009**, *106*, 034506/1.

(166) Kaake, L. G.; Barbara, P. F.; Zhu, X. Y. *J. Phys. Chem. Lett.*, *1*, 628.

(167) Casado, J.; Zgierski, M. Z.; Ewbank, P. C.; Burand, M. W.; Janzen, D. E.; Mann, K. R.; Pappenfus, T. M.; Berlin, A.; PÃ©rez-Inestrosa, E.; Ortiz, R. P.; LÃ³pez Navarrete, J. T. *J. Am. Chem. Soc.* **2006**, *128*, 10134.

(168) Zerbi, G.; Magnoni, M. C.; Hoogmartens, I.; Kiebooms, R.; Carleer, R.; Vanderzande, D.; Gelan, J. *Adv. Mater.* **1995**, *7*, 1027.

(169) Tremolet de Villers, B.; Tassone, C. J.; Tolbert, S. H.; Schwartz, B. J. *J. Phys. Chem. C* **2009**, *113*, 18978.

(170) Lee, J. K.; Wang, Y.-M.; Cho, S.; Wudl, F.; Heeger, A. J. *Org. Electron.* **2009**, *10*, 1223.

(171) Jo, J.; Na, S.-I.; Kim, S.-S.; Lee, T.-W.; Chung, Y.; Kang, S.-J.; Vak, D.; Kim, D.-Y. *Adv. Funct. Mater.* **2009**, *19*, 2398.

(172) Zhang, Y.; de Boer, B.; Blom, P. W. M. *Adv. Funct. Mater.* **2009**, *19*, 1901.

(173) Yakuphanoglu, F.; Mehrotra, R.; Gupta, A.; Munoz, M. *J. Appl. Polym. Sci.* **2009**, *114*, 794.

(174) van Bavel, S.; Sourty, E.; de With, G.; Frolic, K.; Loos, J. *Macromolecules* **2009**, *42*, 7396.

(175) Tuladhar, S. M.; Sims, M.; Kirkpatrick, J.; Maher, R. C.; Chatten, A. J.; Bradley, D. D. C.; Nelson, J.; Etchegoin, P. G.; Nielsen, C. B.; Massiot, P.; George, W. N.; Steinke, J. H. G. *Phys. Rev. B: Condens. Matter Mater. Phys.* **2009**, *79*, 035201/1.

(176) Coropceanu, V.; Cornil, J.; Da Silva Filho, D. A.; Olivier, Y.; Silbey, R.; Bredas, J.-L. *Chem. Rev.* **2007**, *107*, 926.

(177) Lenes, M.; Morana, M.; Brabec, C. J.; Blom, P. W. M. *Adv. Funct. Mater.* **2009**, *19*, 1106.

(178) Blom, P. W. M.; Mihailetchi, V. D.; Koster, L. J. A.; Markov, D. E. *Adv. Mater.* **2007**, *19*, 1551.

(179) McGehee, M. D. *Nat. Photonics* **2009**, *3*, 250.

(180) Westenhoff, S.; Howard, I. A.; Hodgkiss, J. M.; Kirov, K. R.; Bronstein, H. A.; Williams, C. K.; Greenham, N. C.; Friend, R. H. *J. Am. Chem. Soc.* **2008**, *130*, 13653.

(181) Liang, Z.; Nardes, A.; Wang, D.; Berry, J. J.; Gregg, B. A. *Chem. Mater.* **2009**, *21*, 4914.

(182) Nelson, J.; Kwiatkowski, J. J.; Kirkpatrick, J.; Frost, J. M. *Acc. Chem. Res.* **2009**, *42*, 1768.

(183) Huang, Y.-F.; Chang, C.-W.; Smilgies, D.-M.; Jeng, U. S.; Inigo, A. R.; White, J. D.; Li, K.-C.; Lim, T.-S.; Li, T.-D.; Chen, H.-Y.; Chen, S.-A.; Chen, W.-C.; Fann, W.-S. *Adv. Mater.* **2009**, *21*, 2988.

(184) Kokil, A.; Shiyanovskaya, I.; Singer, K. D.; Weder, C. *J. Am. Chem. Soc.* **2002**, *124*, 9978.

(185) Zaumseil, J.; Sirringhaus, H. *Chem. Rev.* **2007**, *107*, 1296.

(186) Sauve, G.; Liu, J.; Zhang, R.; Kowalewski, T.; McCullough, R. D. *Proc. SPIE* **2007**, *6658*, 665810/1.

(187) Blom, P. W. M.; Tanase, C.; van Woudenbergh, T. *Semicond. Polym. (2nd Ed.)* **2007**, *1*, 385.

(188) Arkhipov, V. I.; Heremans, P.; Emelianova, E. V.; Adriaenssens, G. J. *Appl. Phys. Lett.* **2001**, *79*, 4154.

(189) Tseng, H.-E.; Jen, T.-H.; Peng, K.-Y.; Chen, S.-A. *Appl. Phys. Lett.* **2004**, *84*, 1456.

(190) Wallace, J. U.; Young, R. H.; Tang, C. W.; Chen, S. H. *Appl. Phys. Lett.* **2007**, *91*, 152104/1.

(191) Tyutnev, A. P.; Saenko, V. S.; Pozhidaev, E. D.; Ikhsanov, R. S. *J. Phys.: Condens. Matter* **2008**, *20*, 215219/1.

(192) Mozer, A. J.; Sariciftci, N. S.; Lutsen, L.; Vanderzande, D.; Osterbacka, R.; Westerling, M.; Juska, G. *Appl. Phys. Lett.* **2005**, *86*, 112104.

(193) Chen, C.; Peng, R.; Wu, H.; Wang, M. *J. Phys. Chem. C* **2009**, *113*, 12608.

(194) Kim, K.; Liu, J.; Namboothiry, M. A. G.; Carroll, D. L. *Appl. Phys. Lett.* **2007**, *90*, 163511.